Resonant Nanostructures for Optical Waveguide Integration and Metasurfaces

Rui Guo

A thesis submitted for the degree of
Doctor of Philosophy of
The Australian National University

May 2017

Declaration

Declaration of Authorship

This thesis is my own original work, if the research is conducted jointly with another person, or group, I will clearly indicate the contribution to the research in the according chapter.

Rui Guo
2/May/2017

Acknowledgments

First of all, I sincerely thank my supervisor panels – Prof. Yuri Kivshar, Prof. Dragomir Neshev, Dr. Manuel Decker and Dr. Isabelle Staude. I highly appreciate Prof. Yuri Kivshar and Prof. Dragomir Neshev offered me this great PhD opportunity. Date back to four years ago, I still clearly remember how happy I was when I received the scholarship of my PhD offer, and I gladly announced this great news in my wedding ceremony to share my excitement to all my friends and family. During my PhD time, Prof. Yuri Kivshar is always supporting me and my projects, from ideas, fabrications, measurements, to visits, international conferences and training schools. I learned a lot from Porf. Yuri Kivshar. He is always positive, optimistic, enthusiastic, and I found great successful people have the same quality, and he is definitely one of them. I am also very lucky that Prof. Dragomir Neshev is one of my supervisors, who can combine different useful resources together for me, which is crucial for all my PhD projects. I thank Dr. Manuel Decker for passing all his nano-fabrication techniques and experiences to me without any reservation. In addition, as a chair supervisor, he taught me how to use simulation software in detail, how to write reports, posters, papers, and even thesis, how to realize experiments from a theoretical idea and so on. He spent a lot of time on me not only for technique problems, but also on encouraging me from a depressed condition. I thank Dr. Isabelle Staude for useful discussions on fabrications, and introducing me a collaboration project.

Secondly, I thank Dr. Frank Setzpfandt, Prof. Duk Yong Choi and Dr. Mingkai Liu. As collaborators, they are definitely the best ones, and I learned a lot from them. Dr. Frank Setzpfandt generously shared his extraordinary opto-mechanical experiences to me in terms of how to build better performance, high efficient optical measurement setup. During his stay in Nonlinear physics center and my visiting in Jena, he gave me the most efficient and applicable help and advice. Prof. Duk Yong Choi kindly provided his best recipes to me in dielectric nano-fabrications, which he had been studying during the past decades. Working with Dr. Mingkai Liu is a fantastic experience. He always finished his job quickly with high quality, and he is always reliable.

Thirdly, I thank my friends in nonlinear physics center, Dr. Wei Liu, Dr. Mingkai Liu, Mr. Allen Wu, Dr. Ali Mirzaei, Dr. Katie Chong, Dr. Guangyao Li, Dr. Ben Hopkins, Mr. James Titchener for sharing great time together. Especially Mr. Allen Wu and Dr. Ali Mirzaei, we exchanged endless ideas on how to make contributions to this world, how to invent useful devices to help people, how to create companies

that can attract excellent people together. We always have unlimited energy in finding the way to realize our dreams and I always believe that we can.

Finally, I thank my family. My wife, daughter and parents. I remember that once I asked my wife, what is your dream? She answered–to realize yours, and she applied this answer to our daily life with no complains. My daughter is always giving me tons of courage and confidence in pursuing my career. My parents are always my solid support both in my life and my career.

Abstract

Integrated nano-optics and nano-photonics have been very hot topics in the last two decades, and they play very important roles in telecommunications, optical interconnectors, integrated sensing devices, just to name a few. Traditionally, integrated photonic crystals, Mach Zehnder waveguides interferometers, ring resonators, gratings are the key elements for integrated photonic circuits, however, they are bulky and there is a room to decrease further the functional areas to make more compact integrated photonic devices. Due to their ability to confine light in sub-wavelength volumes plasmonic nanoparticles and nanoantennas can serve as a fundamental link between electronic and photonic circuits, as they can bridge large size mismatch between the electronic and optical wave function. Thus, plasmonic elements can be utilized to increase the integration density and performance of active and passive photonic devices, as well as to include new functionalities and concepts for photonic chips. Therefore, our goal is to design subwavelength functional areas by utilizing plasmonic meta atoms to manipulate both farfield and localized light and integrate these plasmonic functional areas into dielectric optical waveguides. However, plasmonic materials suffer from their intrinsic absorption. All-dielectric nanoantennas, on the other hand, exhibit high radiation efficiencies, but the lower field confinement and enhancement which also reduce coupling efficiencies.

Therefore, this thesis is mainly focused on exploiting the novel applications in integrated photonic devices based on applying the advantages of plasmonic and dielectric nanoantennas, respectively. The topics include the integration of plasmonic nanoantennas on silicon waveguides, such as the spectral band splitting by using a single Fano nanoantenna, and polarization demultiplexing by utilizing a dragon fly shape nanoantenna. Furthermore, this thesis also contains hybrid and all dielectric metasurfaces in localized light manipulating, biosensing, and opto-mechanics applications.

Publications

0.1 Journal Publications

[1] R. Guo et al. "Bidirectional waveguide coupling with plasmonic Fano nanoantenns." Applied Physics Letters 105.5 053114 (2014) (chapter2)

[2] R. Guo et al. "Plasmonic Fano Nanoantennas for On-Chip Separation of Wavelength-Encoded Optical Signals." Nano Letters 15.5 3324-3328 (2015) (chapter3)

[3] R. Guo et al. "Multipolar coupling in hybrid metal-dielectric metasurfaces." ACS Photonics 3(3) 349-353 (2016) (chapter5)

[4] M. Liu, R. Guo et al. "Polarization-induced chirality in metamaterials via optomechanical interaction" Advanced Optical Materials (2016) (chapter6)

[5] H. Chen, R. Guo et al "Manipulation of photoluminescence of two-dimensional $MoSe_2$ by gold nanoantennas." Scientific Reports 6 22296 (2016)

[6] R. Guo et al. "High bit-rate ultra-compact light routing with mode-selective on-chip nanoantennas." submitted (2017) (chapter4)

[7] C. I. Ozdemir, R. Guo et al. "All dielectric metasurfaces for bio-sensing." in preparation (2017) (chapter6)

0.2 International Conference Papers and Presentations

[1] R. Guo et al. "Polarization Demultiplexing Waveguide Coupler by a Plasmonic Nanoantenna." CLEO: Science and Innovations. Optical Society of America, 2016. (chapter4)

[2] R. Guo et al. "Integrate plasmonic nanoantennas for polarisation sensitive directional waveguide coupling." SPIE: Micro+Nano Materials, Devices, and Applications, 2015. (chapter4)

[3] R. Guo et al. "Plasmonic Fano Nanoantenna for On-chip Wavelength Demultiplexing." CLEO: Science and Innovations. Optical Society of America, 2015. (chapter3)

[4] E. Rusak, R. Guo et al. "Hybrid Metal-Dielectric Nanoantennas for Directional Emission Enhancement." CLEO: QELS Fundamental Science. Optical Society of America, 2015. (chapter5)

[5] R. Guo, et al. "Fano nanoantenna for on-chip separation of wavelength-encoded optical signals." Advanced Electromagnetic Materials in Microwaves and Optics (METAMATERIALS), 2015 9th International Congress on. IEEE, 2015. (chapter3)

[6] R. Guo, et al. "Ultra-Compact On-chip Spectral-Band Demultiplexing with Plasmonic Fano Nanoantennas." European Quantum Electronics Conference. Optical Society of America, 2015. (chapter3)

[7] H. Chen, R. Guo et al. "Tunable photoluminescence of two-dimensional $MoSe_2$ by gold nanoantennas." SPIE: Micro+Nano Materials, Devices, and Applications, 2015.

[8] L. Wang, R. Guo et al. "Multipolar third harmonic generation in magnetic fishnet metamaterials." SPIE: Micro+Nano Materials, Devices, and Applications, 2015.

[9] R. Guo, et al. "Bidirectional wavelength multiplexing with an optical Fano nanoantenna." CLEO: QELS Fundamental Science. Optical Society of America, 2014. (chapter2)

[10] R. Guo, et al. "Directional waveguide coupling with optical fano antennas." Australian Institute of Physics Congress, 2014. (chapter2)

[11] M. Decker, R. Guo et al "Two-color light routing using bi-directional nanoantennas on waveguides." International Conference on Metamaterials, Photonic Crystals and Plasmonics, META, 2014. (chapter2)

[12] M. Decker, R. Guo, et al "Frequency-Selective Bidirectional Fano Antennas." Postdeadline Presentation, Australia and New Zealand Conference on Optics and Photonics (ANZCOP), 2013. (chapter2)

Contents

Chapter 1

Introduction

1.1 Thesis Statement and Motivation

Our data and information hungry world has driven the immense progress in the semiconductor electronics industry and we have witnessed a continuous progress towards smaller, faster and more efficient electronic devices over the last five decades. Device scaling has also brought about countless challenges. Currently, two of the most daunting problems preventing significant increases in processor speed are thermal and RCL delay-time issues associated with electronic transceivers [1]. Optical interconnects, on the other hand, possess an almost unimaginably large data carrying capacity and may offer interesting new solutions for circumventing these problems [2]. Optical alternatives may be particularly attractive for future chips with more distributed architectures in which a multitude of fast electronic computing units need to be connected by high speed links. Therefore, silicon photonics has been considered to be the next generation of data transmitting interface both for on-and off-chip's solutions. People design light source, modulators, detectors, and demultiplexers based on silicon photonics platform. [Fig. 1.1 (a),(b),(c)].

"This future 3D-integated chip consists of several layers connected with each other with very dense and small pitch interlayer vias. The lower layer is a processor itself with many hundreds of individual cores. Memory layer (or layers) are bonded on top to provide fast access to local caches. On top of the stack is the Photonic layer with many thousands of individual optical devices (modulators, detectors, switches) as well as analogue electrical circuits (amplifiers, drivers, latches, etc.). The key role of a photonic layer is not only to provide point-to-point broad bandwidth optical link between different cores and/or the off-chip traffic, but also to route this traffic with an array of nanophotonic switches. Hence it is named Intra-chip optical network (ICON)" , IBM press release.

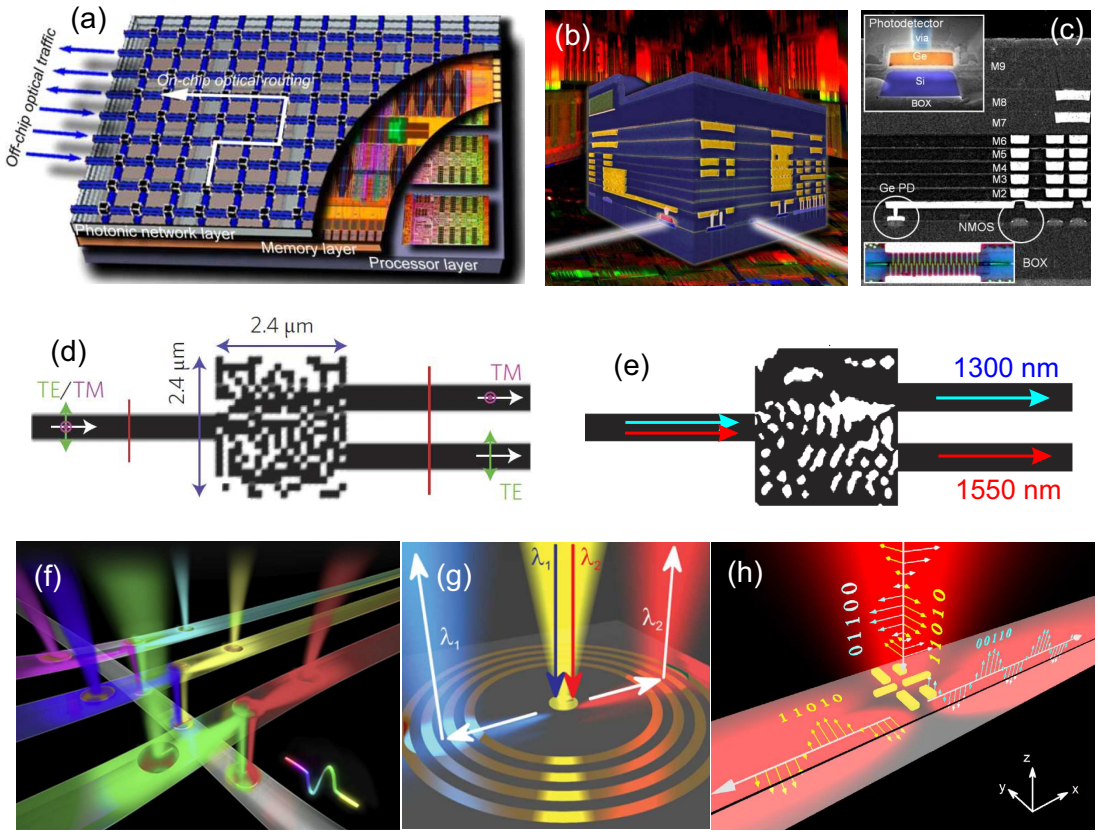

Figure 1.1: (a) IBM's multilayer chip. It uses light instead of electrical signals to transfer information. Thus it allows large volumes of data to be moved fast (25Gbps per channel) between computer chips in servers, large data-centers, and supercomputers via pulses of light. (b) Cross-sectional view of an IBM Silicon Nanophotonics chip combining optical and electrical circuits. (c) Cross-sectional SEM view of a 90nm CINP metal stack with Ge PD embedded into the front-end. Zoomed-in image of a photodetector is shown on top left. Optical microscope top-down image is shown on the low left [3]. (d) Sketch of an integrated nanophotonics polarization beamsplitter [4]. (e) A silicon wavelength demultiplexer that splits 1300 nm and 1550 nm light from an input waveguide into two output waveguides [5]. (f) Utilizing discrete nano-antennas, we can direct different colors or polarizations of light between waveguides, so as to control the complex traffic of optical information. (g) Ultra-compact wavelength demultiplexer waveguide coupler with a single nano-antenna [6]. (h) Scheme of a waveguide-integrated plasmonic nanoantenna for mode-selective polarisation (de-)multiplexing. The device couples light of orthogonal polarisations into different directions and modes of the underlying silicon waveguide.

Unfortunately, their implementation is hampered by the large size mismatch between electronic and dielectric photonic components. Dielectric photonic devices are limited in size by the fundamental laws of diffraction to about half an effective wavelength of light, and tend to be at least one or two orders of magnitude larger than their nanoscale electronic counterparts, even the latest publications of polarization

beam splitter [4] [Fig. 1.1 (d)] and wavelength demultiplexer [5] [Fig. 1.1 (e)] claimed the smallest (micron size). This obvious size mismatch between electronic and photonic components presents a major challenge for interfacing these technologies. It thus appears that further progress will require the development of a radically new solution that can bridge the gap between the world of nanoscale electronics and microscale dielectric photonics. In contrast to conventional large-scale optical dielectric photonics which are difficult to miniaturize, plasmonics nanoantennas [7] provide a superb opportunity that can shrink the functional area into nanometer regime thanks to its light confinement capability. In addition plasmonic nanoantennas provide a promising pathway towards a range of advanced light manipulation functionalities, such as directional scattering, polarization conversion, and fluorescence enhancement. Therefore, in the new generation of data processing and transmitting technology, the role of nanoantennas [Fig. 1.1 (f)] can be a nanometer-size light router. Each nanoantenna can be used as signal splitters that can pass different informations from one waveguide channel into a different layer of orthogonal optical channels for the further data processing, such as nano wavelength demultiplexer (Fig. 1.1 (g), Chapter 2 and 3) and nano polarization demultiplexer (Fig. 1.1 (h), Chapter 4). In this way, the future's processing and transceiver chips can not only remain its compact size with multilayer design but also apply ultra-wide bandwidth and low loss photonics signal channels.

Moreover, plasmonic nanoantennas can also be tailored to provide a link between localized optical near-fields and propagating optical far-fields, allowing for strong enhancement of light-matter interaction processes such as spontaneous emission and quantum light source enhancement. However, they suffer from their intrinsic absorption. All-dielectric nanoantennas, on the other hand, exhibit high radiation efficiencies, but the lower field confinement and enhancement also reduce coupling efficiencies. Hybrid metal-dielectric nanoantennas composed of plasmonic feed elements and dielectric director elements provide a combination of the advantages for both plasmonic and all-dielectric nanoantennas. Hence, they may offer large Purcell enhancements for the localized quantum light source and highly directional radiation patterns while preserving high radiation efficiencies at the same time. This is essentially crucial for manipulating quantum light in nanometer scale for quantum computing and quantum information technology, which has a promising potential to dramatically speed-up in information and data processing rate as comparing to the fastest current electronic computers. Furthermore, this hybrid design may also benefit the bio-sensing and bio-detection field, as the plasmonic feed elements can enhance the marked fluorophores and the dielectric directors can pass photoluminescent information efficiently to the direction of the detectors. We will discuss it in Chapter 5 on the design, fabrication and characterization of hybrid nanoantennas array, or hybrid metasurfaces.

Furthermore, in the current world, a lot of brilliant physics ideas still have huge gaps to the practical applications, and most of them are majorly due to the low efficiency of devices, such as nonlinear optics applications, quantum information technology, negative index metamaterials and so on. Therefore, more and more

researchers are eager to discover high efficient approaches, which can provide bright opportunities to increase devices' performances. Luckily, all dielectric metasurfaces has been reported close to unity efficiency and such metasurfaces are ideal candidates for high quality factors and low damping devices. In chapter 6 we will discuss our all dielectric metasurface solutions for high sensitivity bio-sensing, and low-power drive opto-mechanics applications. Briefly, we designed a dielectric metasurface based on non-parallel coupled electric dipoles made from amorphous silicon material, and this metasurface can provide very narrow resonance linewidth (sub-nanometer scale, we can achieve 5 nm linewidth experimentally due to the fabrication imperfections). Such high Q and high efficiency system can provide high sensitivity and high figure of merit bio-sensors, as well as low power optical dynamic spatial modulation, and dynamic polarization manipulation.

All in all, this thesis includes integrated optical devices for communication, quantum information technology, bio-sensing, opto-mechanics with the most compact and efficient solutions.

1.2 Nanoantennas

1.2.1 A brief history and background (radio wave to optical antennas)

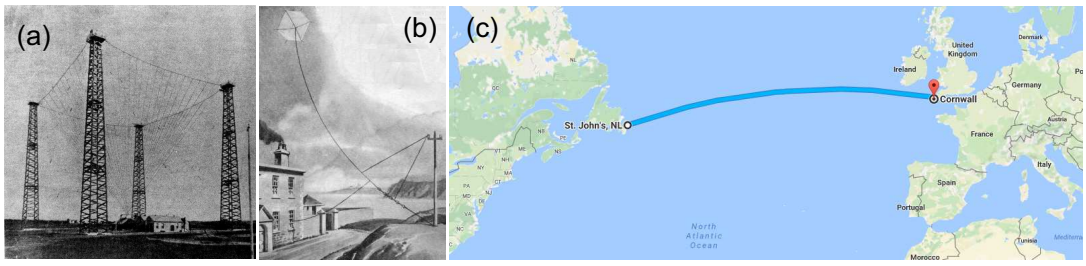

Figure 1.2: (a) Marconi station at Poldhu, Cornwall, England in 1905. The four wooden towers support a network of wires which converge to a point just above the transmitting and receiving buildings between the towers. (b) A scene at St. John's, Newfoundland, showing Senatore Marconi's arrangement for using a kite to support the antenna which he used in his first experiments. (c) Google map showing St. John's and Cornwall.

In 1831, Michael Faraday presented the first experiment on electromagnetic induction by sliding a magnet around the coils (loop antenna) of a wire attached to a galvanometer, and this experiment gave birth to the first antenna which receives the electromagnetic radiation detected by the galvanometer. However, the electromagnetic waves had not been considered at that time until 1865, James Clerk Maxwell brought electricity, magnetism, and light as manifestations of the same phenomenon, which gives the classical theory of electromagnetic radiation [15, 16]. In 1886, Heinrich Rudolph Hertz demonstrated the first wireless electromagnetic communication system. He used a coil-driven spark gap and one-meter wire pair as a radiator.

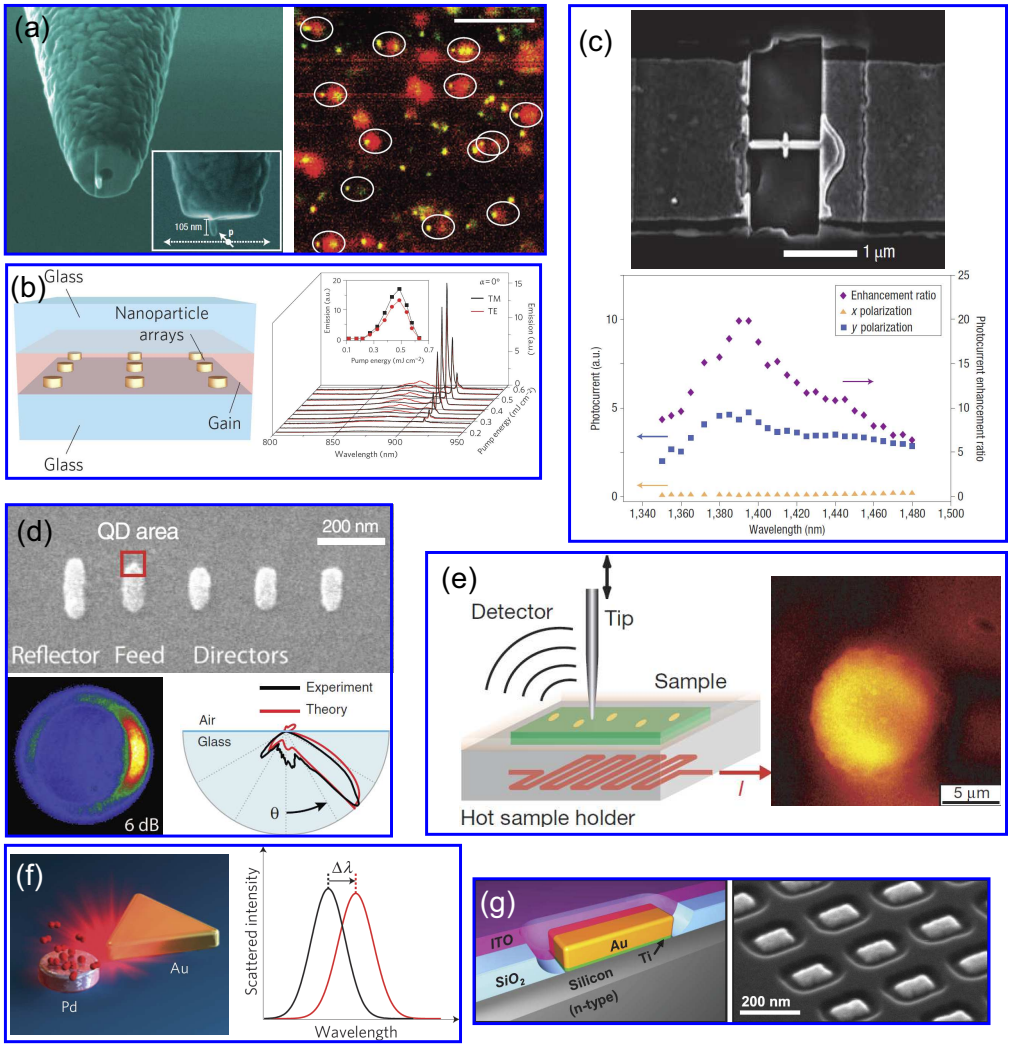

Figure 1.3: (a) An aluminium nano-antenna at the end face of an aperture near-field fibre probe, and a spatial fluorescence map achieved by scanning a with randomly placed isolated single fluorescent molecules [8]. (b) Scheme of the plasmonic nanoparticle array laser and the emission spectra with different pump pulse energies and polarizations [9]. (c) An Scanning electron microscopy (SEM) image of an open-sleeve dipole antenna detector and its measured photocurrent responses with two orthogonal polarizations [10]. (d) An SEM image of five-element Yagi-Uda antenna with quantum dot by the feed element, and its radiation pattern, which shows highly directional scattering of emitted light [11]. (e) The sketch of detection of the thermal radiation scanning tunnelling microscope (TRSTM) signal and TRSTM image recorded simultaneously at 170 ^{o}C, showing the infrared near-field thermal emission scattered by the tip [12]. (f) A palladium and a gold nanoparticles can sense the hydrogen efficiently with the resonance shift of the gold antenna that can be optically detected [13]. (g) Gold resonant antennas on an n-type silicon substrate that can make more compact, wavelength-selected, polarization-specific photodetectors [14].

Capacity spheres were present at the ends for circuit resonance adjustments. The receiver was a simple half-wave dipole antenna. In 1901, Guglielmo Marconi was sending information over large distance from Cornwall, England to St. John's Newfoundland (now part of Canada). He used several vertical wires attached to the ground as a transmitting antenna [Fig. 1.2 (a)]. Across the Atlantic Ocean, the receiving antenna was a 200 meter wire held up by a kite [Fig. 1.2 (b)] [17]. This was the dawn of the antenna and the wireless telecommunication era. From the inception of Marconi's demonstration, antennas and telecommunication continuously flourished. Yagi-Uda antenna was invented in 1926, Horn antenna in 1939, phased array antenna and parabolic reflectors in 1940s, microstrip antennas in 1970s and inverted F-antenna used in the mobile phone market in 1980s.

Nowadays, radiowave or microwave antennas are considered to be an indispensable and mature technology in communication and detection fields. To push antennas theory and its applications into optical frequency regime, more and more people from optics, plasmonics and nano-technology fields are getting involved into this unprecedented new area- *optical antenna*, or *nanoantenna*. The history of optical antenna is accompanied with the near-field optics [18–20], which started with nano-particles, dating back to almost a century ago. However, optical antennas research started to flourish just two decades ago due to the fast development of nano-fabrication technology. As this field has been developing very fast, it diverged into many different sub-fields, such as optical antennas for nano-imaging and spectroscopy [8,21–23][Fig. 1.3 (a)], nano-lasing [9,24][Fig. 1.3 (b)], enhanced light-matter interaction [10,25][Fig. 1.3 (c)], localized light manipulation [11,26,27][Fig. 1.3 (d)], energy harvesting [12,28–30][Fig. 1.3 (e)], sensing [13,31,32][Fig. 1.3 (f)], advanced photovoltaic devices [33], information and detection technology [14,34][Fig. 1.3 (g) and so on.

Moreover, plasmonic nanoparticles and nanoantennas have proven to provide unprecedented opportunities to control and guide light at the nanoscale [35–37]. Due to their unique ability to confine and enhance light to subwavelength volumes, they provide the basis for the development of novel types of solar cells, photo detectors, imaging devices, advanced plasmonic sensors, and nanolasers [36,38]. Plasmonic nanoantennas have also opened up an effective way of manipulating and directing light from localized photon sources and quantum emitters [11,37,39] *via* near-field interactions providing directed emission of light from localized light sources [11,40–45]. Furthermore, plasmonic nanoantennas can provide an efficient way to couple light from free space into plasmonic [27,46,47] or dielectric [48,49] waveguides and *vice versa*. Thus, they can serve as a new type of waveguide coupler for optical chips. Unlike traditional optics, in nano-optics field, the amplitude, phase and polarizations of light can be manipulated within sub-wavelength scale, and nano-antennas are the vital players in this promising field which can tremendously shrink the devices' sizes compared to the traditional ones. Therefore, nano-optics creates a precious opportunity that allows people to understand, master and manipulate the nano-world. This technology can potentially help medicine science, gene engineering, brain study, computer chip, energy storage and so on.

1.2.2 Fundamentals of Nanoantennas

Nanoantennas are antennas for optical wavelength which cover visible to infrared frequency spectrum. Generally, they are used for manipulating light in nanometer scale, such as controlling a localized light source, coupling light into nanometer waveguides and enhancing active materials' photoluminescence. All of these applications are working with nanoantennas' resonances, therefore, the resonance system is fundamentally necessary to be understood in the first place and the very basic model is a general oscillation. This system describes well in important parameters for nanoantennas and nanoparticles, such as resonance characteristics, scattering properties and radiation patterns.

1.2.2.1 General Oscillations – the Lorentz Model

If a simple spring oscillator is undriven and undamped, the forces governing the motion of the mass are only Newton's second law and Hooke's law
Newton's second law: $F = m\ddot{x}$;
Hooke's law: $F = -kx$
where, F is the force, m is the object mass, and k is the hooke's factor. Putting both together, we obtain the equation for the object's displacement with respect to time from the equilibrium position

$$m\ddot{x} = -kx \tag{1.1}$$

The solution to this equation is sinusoidal function with frequency $\omega_0 = \sqrt{\frac{k}{m}}$. This is a natural frequency or fundamental frequency of an undamped spring-like oscillator. To make it more general, a normal oscillation system should include a driving force and a damping force. A typical type of damping is linearly proportional to the velocity of the mass – $F_{damping} = -m\gamma\dot{x}$. Any kind of force can be a driving force. Combining Newton's second law, damping factor, Hooke's law and a driving force, we can have the *Lorentz equation*

$$m\ddot{x} + m\gamma\dot{x} + m\omega_0^2 x = F_{driving} \tag{1.2}$$

We assume that the position and the driving force are time-harmonic varying, and the solution of this equation is

$$x = \frac{F_{driving}/m}{\omega_0^2 - \omega^2 - i\gamma\omega} \tag{1.3}$$

If $\gamma \neq 0$, the proportionality factor between x and $F_{driving}$ is complex, hence, the displacement and driving force are not in phase generally. In order to study phase difference, we write displacement x=A$e^{i\Theta}$($F_{driving}$/m), where the amplitude A and phase Θ are

$$A = \frac{1}{[(\omega_0^2 - \omega^2)^2 + \gamma^2\omega^2]^{1/2}}, \quad (1.4)$$
$$\Theta = tan^{-1}\frac{\gamma\omega}{\omega_0^2 - \omega^2}.$$

If we differentiate the amplitude equation of (1.4), we can achieve the largest amplitude for the *driving frequency* or the *damping frequency* [50]

$$\omega_{DF} = \sqrt{\omega_0^2 - \gamma^2/2} \quad (1.5)$$

red shifted from the natural frequency of the oscillator by an amount determined by the damping γ.

1.2.2.2 Lorentz Model for Nanoantennas

A dipole antenna is the simplest structure of the antenna family. Now, we take a gold nanorod for example. The rod diameter is 40 nm, and the length is 160 nm. A linearly polarized plane wave E_{plane}, whose electric field is along the antenna axis, excites the rod antenna [see Fig. 1.4(a)], and the antenna radiates (scatters) electromagnetic fields. This oscillation system can be described by Eq.(1.2) [50, 51], where the mass m is the effective mass of the conduction electrons in the particle, the displacement x is the plasmon amplitude, and $m\omega_0^2$ corresponds to the electromagnetic restoring force originating from the displacement of the conduction electrons, γ is the damping factor due to electron collisions, and driving force now is from the plane wave. In addition, this system can also be described by a dipole antenna equivalent circuit [Fig. 1.4(b)]. Therefore, we can have the differential equation in terms of circuit current i

$$\frac{d^2i(t)}{dt^2} + \frac{R}{L}\frac{di(t)}{dt} + \frac{1}{LC}i(t) = \frac{\omega}{L}V \quad (1.6)$$

This is also a Lorentz differential equation description of nanoantenna system with a different perspective.

We use CST Microwave Studio to simulate gold rod nanoantennas' characteristics, which is a 3D electromagnetic simulation software utilizing the frequency domain solver. We monitor the local electric field amplitude and phase of the rod antenna by inserting a probe at the center of the nanorod antenna, [see Fig. 1.4(c)]. The results indicates that the electric field of nanorod antenna can be well fitted by the Lorentz model [Eq. 1.4]. The phase analysis is particularly important for directional radiation (scattering) with nanoantenna, and we will discuss it specifically in chapter 2 and chapter 3 in different cases.

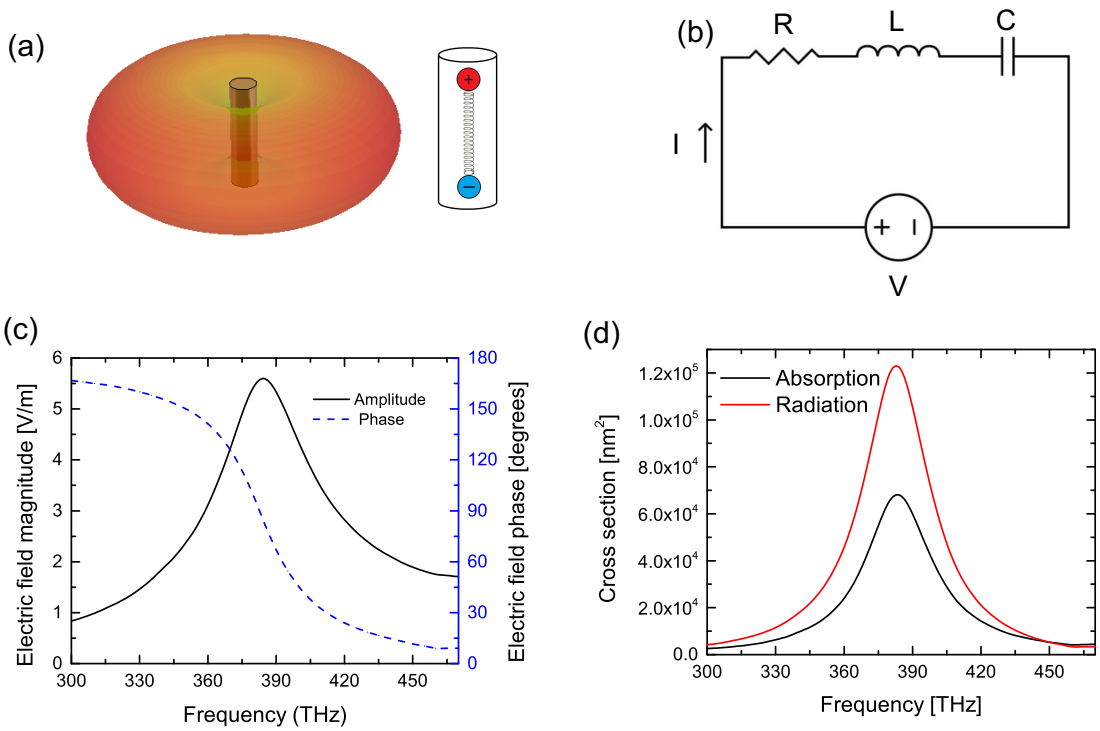

Figure 1.4: (a) A gold rod nanoantenna with its scattered farfield pattern and its collective excitation mode as an electric dipole oscillation. (b) Antenna's equivalent R L C circuit. (c) The electric field amplitude and phase of the nanorod antenna. (d) Radiation cross section and absorption cross section of the nanorod.

1.2.2.3 Cross Sections of Nanoantennas

In order to study nanoantenna's radiation (scattering), absorption abilities, and how nanoantennas react with external electromagnetic fields, here, we introduce the *scattering*, *absorption* and *extinction* cross sections [52]. Extinction is the attenuation of an electromagnetic wave by scattering and absorption as it travels through particles. Therefore,

$$C_{ext} = C_{abs} + C_{sca(rad)}. \tag{1.7}$$

where C_{ext} is the *Extinction Cross Section*, C_{abs} is the *Absorption Cross Section*, and $C_{sca(rad)}$ is the *Scattering Cross Section* (or *Radiation Cross Section*). Fig. 1.4(d) presents the absorption and radiation cross section of the rod antenna, and both of them show the resonance frequency of the antenna, which are simulated by CST Microwave Studio. Because the cross sections are related to power rather than field, cross section's lineshape [Fig. 1.4(d)] is squared by the field lineshape [Fig. 1.4(c)]. *Scattering (Radiation)* of electromagnetic waves is related to the heterogeneity of the system. A gold nano particle in vacuum, for instance, is illuminated by an electromagnetic plane wave, and electric charges in the nanorod is set into oscillation which radiates electromagnetic energy in all directions. Moreover, the excited charges in nanorod may

transfer part of the incident electromagnetic energy into other forms, thermal energy, for example, and this process is *absorption*.

1.2.2.4 Radiation Pattern and Directivity

The radiated power (the square of the magnitude of the electric or magnetic field) in the farfield region is represented as a function of the directional coordinates, named the *Radiation Pattern* [17][see Fig. 1.4(a), a rod antenna with its radiation pattern at resonant frequency].

$$\int_0^{\pi}\int_0^{2\pi} p(\theta,\phi)sin\theta d\phi d\theta = P_{rad.} \tag{1.8}$$

where $p(\theta,\phi)$ is the angular power density. *Directivity* [17] of an antenna defined as the ratio of the radiation intensity in a given direction from the antenna to the radiation intensity averaged over all directions.

$$D(\theta,\phi) = \frac{p(\theta,\phi)}{P_0} = \frac{4\pi p(\theta,\phi)}{P_{rad}} \tag{1.9}$$

where $p(\theta,\phi)$ is radiation intensity (W/unit solid angle), P_0 is radiation intensity of isotropic source (W/unit solid angle), and P_{rad} is total radiated power (W).

1.2.2.5 Babinet's Principle of Complementary Screens

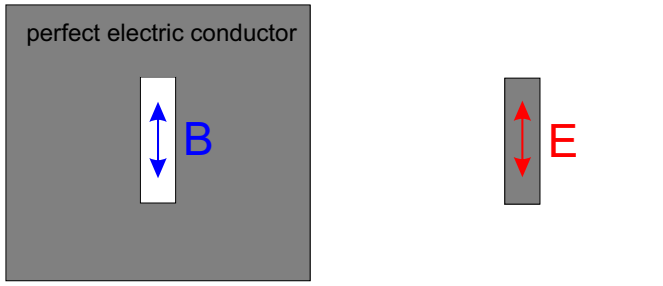

(a) Screen with opening (b) Complementary dipole

Figure 1.5: Equivalent radiators according to Babinet's principle. (a) Opening on a screen and (b) its complementary dipole.

In antenna design's perspective, sometimes, it is very useful and convenient to apply *Babinet's principle*. Babinet's principle [17, 53, 54] claims that when the field behind a screen with an opening is added to the field of a complementary structure, the sum is equal to the field when there is no screen (see Fig 1.5). Suppose a screen and its complement are immersed in a medium with an intrinsic impedance η and have terminal impedances of Z_s and Z_c, respectively, the impedances are related by

$$Z_s Z_c = \frac{\eta^2}{4}. \tag{1.10}$$

The farfields radiated by the opening on the screen ($E_{\theta s}$, $E_{\phi s}$, $H_{\theta s}$, $H_{\phi s}$) are related to the farfields of the complement ($E_{\theta c}$, $E_{\phi c}$, $H_{\theta c}$, $H_{\phi c}$)

$$E_{\theta s} = H_{\theta c}, \quad E_{\phi s} = H_{\phi c}, \quad H_{\theta s} = -\frac{E_{\theta c}}{\eta_0^2}, \quad H_{\phi s} = -\frac{E_{\phi c}}{\eta_0^2} \tag{1.11}$$

where η_0 is the impedance of vacuum. The Babinet principle will help the design of a compact Fano nanoantennas, which we will discuss in more details in chapter 2 and chapter 3.

1.3 Nanoantenna Array – Metasurfaces and Metamaterials

In the previous section (Chapter 1.2), we discussed about nanoantennas, and in this section, we will expand single nanoantenna to infinite two dimensional arrays– Metasurfaces.

1.3.1 Two dimensional expansion of identical nanoantennas

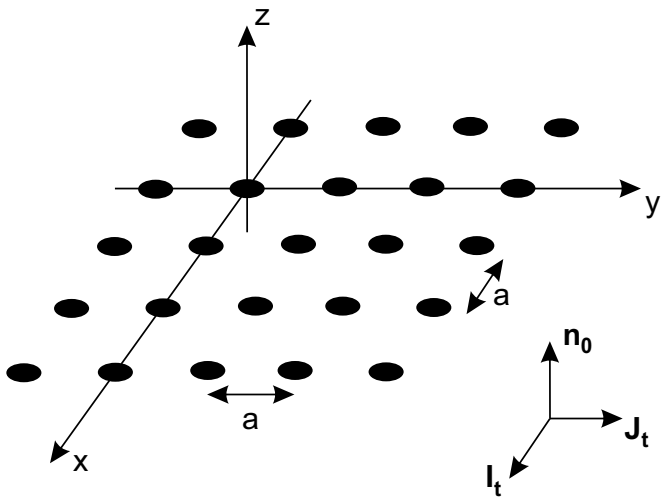

Figure 1.6: Planar regular array of small electrically or magnetically polarizable particles. The array extends to infinity along x and y axes.

Metasurface is generally formed by a two-dimensional periodical subwavelength array of small identical particles (nanoantennas) [55–58] [Fig. 1.6]. Suppose they are electrically polarizable unit cells. Let the grid have square cells of the size a$\times$a and be excited by incident electric field $\mathbf{E}_{inc}$ of plane wave. If we want to know the reflection and transmission coefficients, we have to calculate the dipole moment of the unit cells. The key problem now is the calculation of the field acting on every particle, the *local field*, which is the sum of the incident field $\mathbf{E}_{inc}$ and the field induced by all other neighbor cells $\mathbf{E}_{int}$–*interaction field*. We can calculate the interaction field numerically, summing up the fields of the dipoles in the array. An appropriate limit can be taken

as the grid contains infinitely amount of particles. Here, we introduce a circle of radius R around one of the particles [Fig. 1.7] and calculate

$$\mathbf{E}_{hole} = \Sigma \mathbf{E}_p \tag{1.12}$$

summing up the fields created at the origin by all the dipoles sitting inside the circle

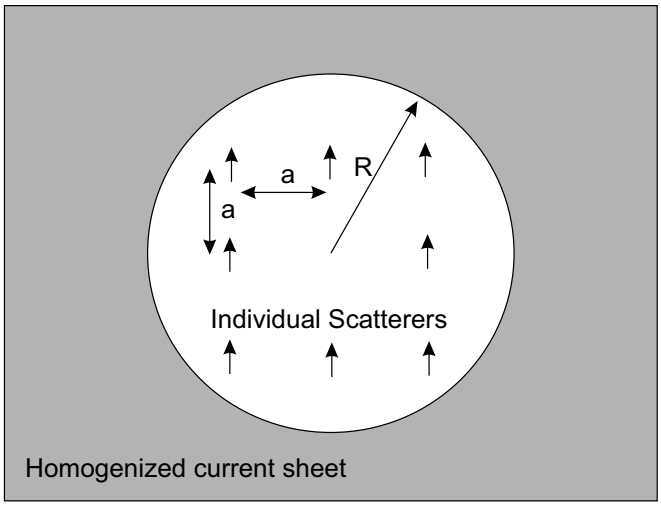

Figure 1.7: Calculation of the local field: individual dipoles near the reference particle and a homogenized current sheet far from the reference particle. Electric dipole moments of small particles are shown by the small arrows. the reference dipole at the center has been removed.

of radius R except the reference dipole located at the origin. In the next step, we increase the radius R until the result converges. Actually, the wave field of dipoles at distance R behaves as 1/R, but the number of dipoles located at distance R increases proportionally to R. Assume small losses in space, and the wave number k has a small negative imaginary part, and split the interaction field into two parts: the field of the dipoles inside the circle of radius R and field of the dipoles located outside this circle. The calculation of the second part can be simplified if we assume that we can replace the discrete set of dipoles by an averaged continuous distribution of polarization, which makes sense for large R. This is because from a large enough distance the reference dipole cannot "see" the individual dipoles but rather feels the field of the averaged polarization. Thus

$$\mathbf{E}_{loc} = \mathbf{E}_{inc} + \mathbf{E}_{sheet} + \mathbf{E}_{hole} \tag{1.13}$$

where $\mathbf{E}_{sheet}$ is the field of a current sheet with a hole of radius R. The sum of the two last parts gives the interaction field

$$\mathbf{E}_{int} = \mathbf{E}_{sheet} + \mathbf{E}_{hole} = \beta \mathbf{p} \tag{1.14}$$

where $\mathbf{p}$ is the dipole moment of one inclusion, β is the array *interaction constant*. In

addition, the book *Ref. [58]* gives a detailed description on the interaction constant and its relation to the hole radius R [Fig. 1.7]. It concludes that the interaction field in infinite arrays is determined by a few nearest inclusions and R=a/1.438.

In general, the electromagnetic properties of a single electrically small scatterer can be modeled with the help of polarizability dyadics [57]

$$\begin{bmatrix} \mathbf{p} \\ \mathbf{m} \end{bmatrix} = \begin{bmatrix} \bar{\bar{\alpha}}_{ee} & \bar{\bar{\alpha}}_{em} \\ \bar{\bar{\alpha}}_{me} & \bar{\bar{\alpha}}_{mm} \end{bmatrix} \cdot \begin{bmatrix} \mathbf{E}_{loc} \\ \mathbf{H}_{loc} \end{bmatrix} \tag{1.15}$$

where $\mathbf{p}$ and $\mathbf{m}$ are the electric and magnetic dipole moments that are induced by the local fields $\mathbf{E}_{loc}$ and $\mathbf{H}_{loc}$ at the location of the small particle. If you think general metasurface, the array period is smaller than the free space wavelength, so that no higher-order propagating waves are created. The effect of the array on the local field [(1.13), (1.14)] can be modelled with the interaction constant [58, 59] β

$$\mathbf{E}_{loc} = \mathbf{E}_{inc} + \bar{\bar{\beta}}_e \cdot \mathbf{p} \tag{1.16}$$

$$\mathbf{H}_{loc} = \mathbf{H}_{inc} + \bar{\bar{\beta}}_m \cdot \mathbf{m} \tag{1.17}$$

where

$$\bar{\bar{\beta}}_e = Re[-j\frac{\omega\eta_0}{4a^2}(1+\frac{1}{jkR})e^{-jkR}]\bar{\bar{I}}_t + j[\frac{\eta_0\epsilon_0\mu_0\omega^3}{6\pi} - \frac{\eta_0\omega}{2a^2}]\bar{\bar{I}}_t \tag{1.18}$$

$$\bar{\bar{\beta}}_m = \frac{\bar{\bar{\beta}}_e}{\eta_0^2} \tag{1.19}$$

where $k = \omega\sqrt{\epsilon_0\mu_0}$ is the free space wave number, $\eta_0 = \sqrt{\mu_0/\epsilon_0}$ is the free space wave impedance, R=a/1.438, $\bar{\bar{I}}_t$ is the tangential unit dyadic, $\mathbf{n}_0$ is the unit vector normal to the array plane [Fig. 1.6], and Re[z] is the real part of z.

In order to study the reflection and transmission from an array, one has to solve the induced dipole moments. This time, we use the effective polarizabilities that relate the induced dipole moments to the incident field

$$\begin{bmatrix} \mathbf{p} \\ \mathbf{m} \end{bmatrix} = \begin{bmatrix} \bar{\bar{\tilde{\alpha}}}_{ee} & \bar{\bar{\tilde{\alpha}}}_{em} \\ \bar{\bar{\tilde{\alpha}}}_{me} & \bar{\bar{\tilde{\alpha}}}_{mm} \end{bmatrix} \cdot \begin{bmatrix} \mathbf{E}_{inc} \\ \mathbf{H}_{inc} \end{bmatrix} \tag{1.20}$$

The effective polarizabilities can be obtained by substituting the local fields in Eq. 1.15 from Eq. 1.16 and Eq. 1.17 and finding the dipole moments as functions of $\mathbf{E}_{inc}$ and $\mathbf{H}_{inc}$. The result for the effective polarizabilities are functions of the polarizabilities

of an individual particle and the interaction constants $\bar{\bar{\beta}}$.

$$\bar{\bar{\alpha}}_{ee} = (\bar{\bar{I}}_t - \bar{\bar{\alpha}}_{ee}\cdot\bar{\bar{\beta}}_e - \bar{\bar{\alpha}}_{em}\cdot\bar{\bar{\beta}}_m\cdot(\bar{\bar{I}}_t - \bar{\bar{\alpha}}_{mm}\cdot\bar{\bar{\beta}}_m)^{-1})\cdot\bar{\bar{\alpha}}_{me}\cdot\bar{\bar{\beta}}_e)^{-1} \cdot(\bar{\bar{\alpha}}_{ee} + \bar{\bar{\alpha}}_{em}\cdot\bar{\bar{\beta}}_m\cdot(\bar{\bar{I}}_t - \bar{\bar{\alpha}}_{mm}\cdot\bar{\bar{\beta}}_m)^{-1}\bar{\bar{\alpha}}_{me}) \tag{1.21}$$

$$\bar{\bar{\alpha}}_{em} = (\bar{\bar{I}}_t - \bar{\bar{\alpha}}_{ee}\cdot\bar{\bar{\beta}}_e - \bar{\bar{\alpha}}_{em}\cdot\bar{\bar{\beta}}_m\cdot(\bar{\bar{I}}_t - \bar{\bar{\alpha}}_{mm}\cdot\bar{\bar{\beta}}_m)^{-1})\cdot\bar{\bar{\alpha}}_{me}\cdot\bar{\bar{\beta}}_e)^{-1} \cdot(\bar{\bar{\alpha}}_{em} + \bar{\bar{\alpha}}_{em}\cdot\bar{\bar{\beta}}_m\cdot(\bar{\bar{I}}_t - \bar{\bar{\alpha}}_{mm}\cdot\bar{\bar{\beta}}_m)^{-1}\bar{\bar{\alpha}}_{mm}) \tag{1.22}$$

$$\bar{\bar{\alpha}}_{me} = (\bar{\bar{I}}_t - \bar{\bar{\alpha}}_{mm}\cdot\bar{\bar{\beta}_m} - \bar{\bar{\alpha}}_{me}\cdot\bar{\bar{\beta}}_e\cdot(\bar{\bar{I}}_t - \bar{\bar{\alpha}}_{ee}\cdot\bar{\bar{\beta}}_e)^{-1})\cdot\bar{\bar{\alpha}}_{em}\cdot\bar{\bar{\beta}}_m)^{-1} \cdot(\bar{\bar{\alpha}}_{me} + \bar{\bar{\alpha}}_{me}\cdot\bar{\bar{\beta}}_e\cdot(\bar{\bar{I}}_t - \bar{\bar{\alpha}}_{ee}\cdot\bar{\bar{\beta}}_e)^{-1}\bar{\bar{\alpha}}_{ee}) \tag{1.23}$$

$$\bar{\bar{\alpha}}_{mm} = (\bar{\bar{I}}_t - \bar{\bar{\alpha}}_{mm}\cdot\bar{\bar{\beta}}_m - \bar{\bar{\alpha}}_{me}\cdot\bar{\bar{\beta}}_e\cdot(\bar{\bar{I}}_t - \bar{\bar{\alpha}}_{ee}\cdot\bar{\bar{\beta}}_e)^{-1})\cdot\bar{\bar{\alpha}}_{em}\cdot\bar{\bar{\beta}}_m)^{-1} \cdot(\bar{\bar{\alpha}}_{mm} + \bar{\bar{\alpha}}_{me}\cdot\bar{\bar{\beta}}_e\cdot(\bar{\bar{I}}_t - \bar{\bar{\alpha}}_{ee}\cdot\bar{\bar{\beta}}_e)^{-1}\bar{\bar{\alpha}}_{em}) \tag{1.24}$$

In the incident plane wave, the electric and magnetic fields are related and the induced dipole moments (1.20) with $\mathbf{H}_{inc} = -\frac{1}{\eta_0}\cdot\bar{\bar{J}}_t\cdot\mathbf{E}_{inc}$ can be written as

$$\mathbf{p} = (\bar{\bar{\alpha}}_{ee} - \frac{1}{\eta_0}\bar{\bar{\alpha}}_{em}\cdot\bar{\bar{J}}_t)\cdot\mathbf{E}_{inc} \tag{1.25}$$

$$\mathbf{m} = (\bar{\bar{\alpha}}_{me} - \frac{1}{\eta_0}\bar{\bar{\alpha}}_{mm}\cdot\bar{\bar{J}}_t)\cdot\mathbf{E}_{inc} \tag{1.26}$$

where $\bar{\bar{J}}_t = \mathbf{n}_0\times\bar{\bar{I}}_t$ is the transverse rotation dyadic.

The above polarizability dyadics are very general case for isotropic media. However, many metasurfaces are based on non-chiral, symmetric inclusions, such as nanodisk structures. In this case, the polarizabilities have no cross terms, and just have its electric and magnetic components. In addition, each meta-cell is one nanoantenna, therefore we model the polarizabilities using the conventional Lorentz dispersion model near the resonance [Eq. 1.3], adequately describes electric and magnetic dipolar response of small inclusions of arbitrary nature

$$\alpha_{ee} = \frac{A_e}{\omega_e^2 - \omega^2 - i\omega\gamma_e} \tag{1.27}$$

$$\alpha_{mm} = \frac{A_m}{\omega_m^2 - \omega^2 - i\omega\gamma_m} \tag{1.28}$$

where γ_e and γ_m are the loss factors of the electric and magnetic modes of the unit cell, respectively. A_e and A_m are the amplitude coefficients.

The induced dipole moments (1.25) and (1.26) correspond to averaged electric and magnetic current sheets with the surface current densities $\mathbf{J}_e = (j\omega\mathbf{p})/a^2$ and $\mathbf{J}_m = (j\omega\mathbf{m})/a^2$ that radiate plane waves into free space. The reflected field is the sum of the fields radiated by these surface currents

$$\mathbf{E}_r = -\frac{j\omega}{2a^2}\cdot[\eta_0\mathbf{p} - \mathbf{n}_0\times\mathbf{m}] \tag{1.29}$$

Similarly, the transmitted field is the sum of the incident field and the fields caused

by the array

$$\mathbf{E}_t = \mathbf{E}_{inc} - \frac{j\omega}{2a^2} \cdot [\eta_0 \mathbf{p} + \mathbf{n}_0 \times \mathbf{m}] \tag{1.30}$$

Combining Equations (1.25), (1.26), (1.29) and (1.30), we can have the *Reflectance* and *Transmittance* expressions:

$$R = (\frac{\mathbf{E}_r}{\mathbf{E}_{inc}})^2 \tag{1.31}$$

$$T = (\frac{\mathbf{E}_t}{\mathbf{E}_{inc}})^2 \tag{1.32}$$

Moreover, the phase control in term of transmission and reflection can also be achieved

$$\Theta_R = tan^{-1}(\frac{\mathbf{E}_r}{\mathbf{E}_{inc}}) \tag{1.33}$$

$$\Theta_T = tan^{-1}(\frac{\mathbf{E}_t}{\mathbf{E}_{inc}}) \tag{1.34}$$

1.3.2 Collective Oscillation System – Electromagnetic Response of Materials and Metamaterials

In the previous section, we showed that arrays of dipoles behave as a two-dimensional *metasurface* with an effective response, such as transmittance and reflectance. Next, we present a simplified effective oscillator response which is useful for describing the effective material parameters for homogeneous materials, including three-dimensional *metamaterials*.

1.3.2.1 Optical Dielectric Response – Lorentz Model

Think about a dielectric medium with an external light excitation. The induced dipole moment $\mathbf{p}$ of an oscillator is ex which produced by one electron displacing from its atom-core of its dielectric material, if n is the number of oscillators per unit volume and e is the electron charge, the polarization $\mathbf{P} = ne\mathbf{x}$. According to Eq.(1.3) with $F_{driving} = e\mathbf{E}$, we have

$$\mathbf{P} = \frac{\omega_p^2}{\omega_0^2 - \omega^2 - i\gamma\omega}\epsilon_0 \mathbf{E} \tag{1.35}$$

where the *plasma frequency* is $\omega_p = \sqrt{\frac{ne^2}{m\epsilon_0}}$. The dielectric function is

$$\epsilon = 1 + \chi = 1 + \frac{\omega_p^2}{\omega_0^2 - \omega^2 - i\gamma\omega} \tag{1.36}$$

with real and imaginary parts

$$\epsilon' = 1 + \chi' = 1 + \frac{\omega_p^2(\omega_0^2 - \omega^2)}{(\omega_0^2 - \omega^2)^2 + \gamma^2\omega^2} \tag{1.37}$$

$$\epsilon'' = \chi'' = \frac{\omega_p^2\gamma\omega}{(\omega_0^2 - \omega^2)^2 + \gamma^2\omega^2} \tag{1.38}$$

where χ is the electric susceptibility. The above dielectric functions are well described for light-matter interactions, which is based on each individual dipole moment $\mathbf{p}$ or polarizability. Suppose we have three dimensional nanoantennas array, which lattice constant is much smaller than the wavelength. This three-dimensional nanoantenna arrays can mimic the collective polarizability as a whole, as such, we can engineer materials dielectric function, in terms of its permittivity and permeability. This is the concept of *Metamaterials*. Generally, metamaterials are formed by either dielectric or metal unit-cells depending on different functionalities. The Lorentz model describes well the dielectric material, while the Drude model is suitable for metals.

1.3.2.2 Optical Metal Response – Drude Model

The optical properties of metals can be explained by a *plasma model* [60] – a collective motion of the free electron gas against a fixed background of positive ion cores. The electrons oscillate in response to the applied electromagnetic field, and their motion is damped via collisions occurring with a characteristic collision frequency $\gamma = 1/\tau$. τ is the relaxation time of the free electron gas. The optical response of a collection of free electrons can be achieved from the Lorentz oscillator model [Eq. (1.2)] without Hooke's springs ($F = kx$). Therefore, we can have *Drude Model*

$$m\ddot{\mathbf{x}} + m\gamma\dot{\mathbf{x}} = -e\mathbf{E} \tag{1.39}$$

in this case, the macroscopic polarization is given by

$$\mathbf{P} = -ne\mathbf{x} = -\frac{\omega_p^2}{\omega^2 + i\gamma\omega}\epsilon_0\mathbf{E} \tag{1.40}$$

therefore, we can have the dispersion of dielectric function for metal

$$\epsilon = 1 - \frac{\omega_p^2}{\omega^2 + i\gamma\omega} \tag{1.41}$$

with real and imaginary parts

$$\epsilon' = 1 - \frac{\omega_p^2}{\omega^2 + \gamma^2} \tag{1.42}$$

$$\epsilon'' = \frac{\omega_p^2\gamma}{\omega(\omega^2 + \gamma^2)} \tag{1.43}$$

1.3.3 Introduction and Background of Metasurfaces and Metamaterials

1.3.3.1 Metamaterials

Metamaterials [61] are artificially designed with meta-atoms or meta-molecules that are much smaller than the wavelength being considered for manipulating electromagnetic waves in different ways. As a material, the electromagnetic response is determined by the permittivity ε and permeability μ [62]. These two parameters describe the electromagnetic wave and matter interaction, with two important values-refractive index $n = \sqrt{\mu\varepsilon}$, and impedance $Z = \sqrt{\mu/\varepsilon}$, which are the macroscopic parameters. Fig. 1.8 (c) presents the relation between different types of materials and its permittivity and permeability with their real parts. Conventional transparent materials are in the first quadrant, which has both positive values of ε and μ, such as air, water, crystals and semiconductors. A negative value of $\varepsilon(\mu)$ means that the vector of the induced electric(magnetic) field inside the material points at the opposite direction to the incident field. Noble metals are good examples representing the materials in the second quadrant with positive μ but negative ε. A very rare example of negative μ was discovered in ferromagnetic medium near a resonance [63]. All in all, metamaterial research is to innovate and explore the electromagnetic parameter space [Fig. 1.8 (c)]. In other words, people in this field create artificial materials which do not violate the Maxwell's equation but expand region of the parameter space which the conventional media cannot reach.

The earliest metamaterials to our knowledge would be the Lycurgus Cup [Fig. 1.8 (a)], the Roman glass challis dating back to 4th century AD. The glass with metallic nano particles [Fig. 1.8 (b)] embedded [65], appears green when viewed in reflected light but red with light transmitted through the glass [64, 71]. At that time, people applied metamaterials in art pieces, but didn't fully understand the physics behind this phenomenon. The research on metamaterials started to be blossomed since 1990s, when J. B. Pendry et al proposed the periodic thin wires can work as a low frequency plasma with a negative value of effective permittivity [72], and periodic double split ring resonators can provide strong magnetic resonances which cause a negative value of effective permeability [Fig.1.8(e)] [67]. Following Pendry's prediction, in 2000, D. R. Smith et al experimentally demonstrated a composite medium exhibits a frequency region in the microwave regime with simultaneously negative values of effective permeability and permittivity [Fig.1.8(f)] [68]. Right after the successful experimental work, at the same year, Pendry's theoretical work on perfect lens [Fig.1.8(g)] [69] represented the very first try to fill the gap of a novel concept of metamatrials and its exciting applications. Five years later, the first experiment paper on the "perfect lens" was published [Fig.1.8(h)] [70]. Conspicuously, the field of metamaterials originated from the negative refraction medium, which was theoretically predicted by Veselago dating back in 1968. Veselago's proposal [66] has several interesting phenomena, such as reversed Doppler effect, reversed Cerenkov radiation, reversed Goos-Hänchen shift, and left-handed lens[Fig. 1.8 (d)]. In order to reach the negative refraction in optical frequency, a bunch of approaches have been introduced, such as coupled cut-wires [73], fishnet structure [74–77], and coax-

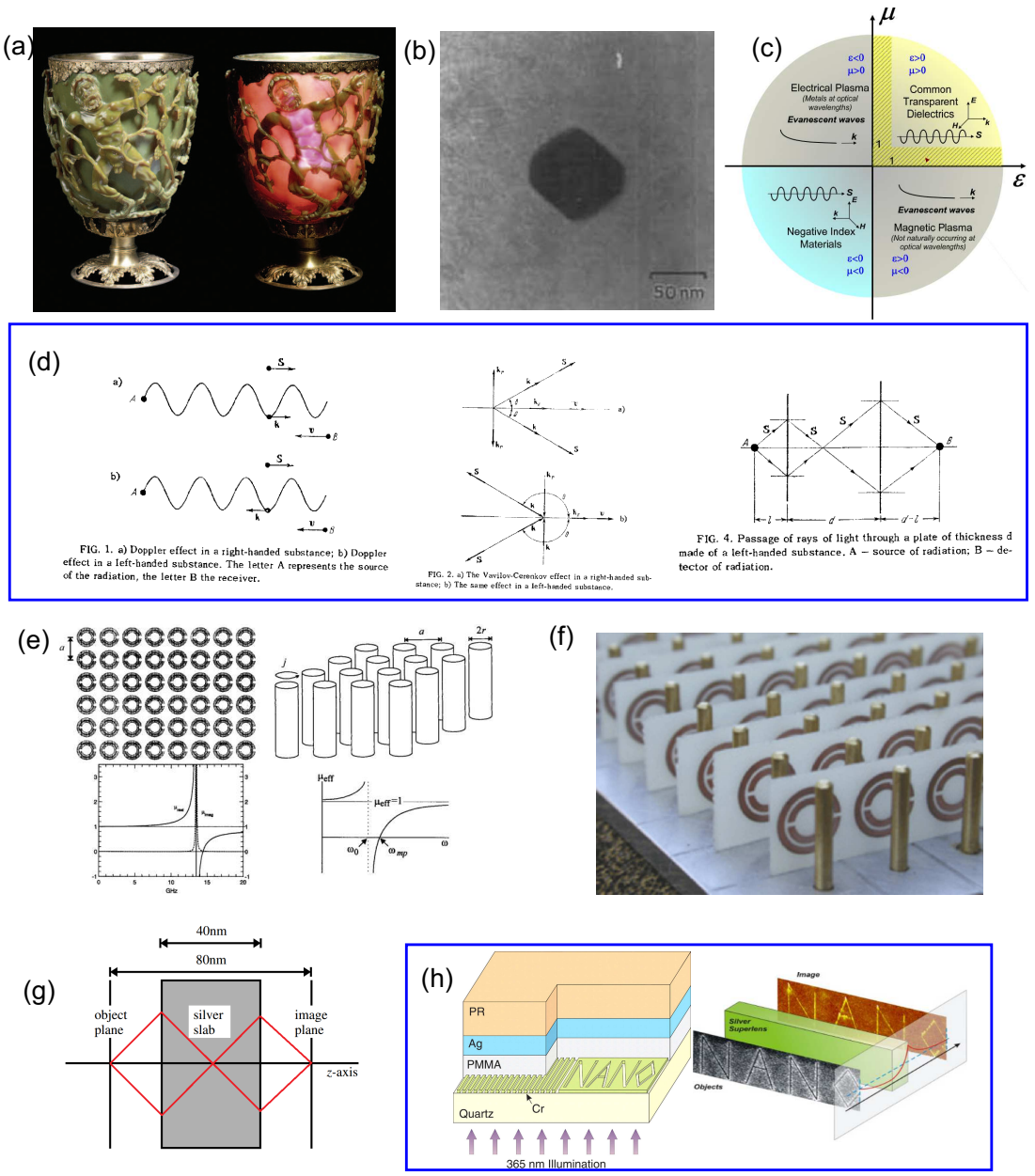

Figure 1.8: (a) Lycurgus Cup viewed with reflected light (left), and with transmitted light (right) (British Museum; AD fourth century) [64]. (b) A TEM image of a metallic particle in the glass of the Lycurgus cup [65]. (c) The coordinate system for permittivity and permeability [61]. (d) Veselago's prediction in reversed Doppler effect, reversed Cerenkov radiation, and left-handed lens [66]. (e) Pendry's work on negative effective permeability [67] (f) The first demonstration of a negative index metamaterial by D. R. Smith et al [68]. (g) The perfect lens proposed by J. B. Pendry, that made of negative materials [69]. (h) The first experimental demonstration of superlens with a thin slab of silver [70].

ial waveguide arrays [78,79]. Nowadays, metamaterials study has been expended far beyond negative refraction, and it has emerged into other research directions, such as optical magnetism [73, 80–82], artificial chirality [83–87], nonlinear optical metamaterials [88–91], super resolution imaging with metamaterials [70, 92–98], and electromagnetic cloaks of invisibility [99–103], and so on. Moreover, modern research on metamaterials is continuously making revolutions in different fields, including optical sensing, quantum photonics, miniature phase array antenna, novel waveguides, nano-scale photolithography and photonic circuits.

1.3.3.2 Metasurfaces

Those demanding practical applications require solid design and fabrication support to make them meaningful. Although nano fabrication technology has been developed fast during last two decades, there are still a lot of limitations for real three dimensional metamaterials [111]. Hence, currently, more and more works are focused on thin layer *metasurfaces* [112,113], which are generally formed by a two-dimensional periodical subwavelength arrays of small particles. Such metasurfaces can provide a variety of unprecedented advancement compared to the traditional optical devices, such as lenses, waveplates and holograms. The conventional optical components root on gradually phase change accumulated during light propagating in the bulk medium to shape light beams. In contrast to this, metasurfaces can provide abrupt amplitude, phase and polarization change within the scale of a wavelength. In 2011, N. Yu et al experimentally demonstrated light phase shifted when passing through a 50 nm thin metasurface. By changing the angle of each v-shape meta-atoms, the light phase can be changed accordingly and locally, therefore it paves an innovative way to manipulate the beam shape and wave front. [Fig. 1.9 (a)] [104]. Applying the similar design, in 2012, N. Yu et al experimentally presented a high efficient quarter-wave plate which can cover a broadband wavelength range by a thin layer of metasurface [Fig. 1.9 (b)] [105]. In the same year, S. Sun et al designed a microwave metasurface that can couple free space electromagnetic waves into propagating waves and surface waves on metasurface [Fig. 1.9 (c)] [106]. In general, a thin layer metasurface spans a lot of practical and applicable fields such as functional hologram generation [Fig. 1.9 (d)] [107]; vortex beam generation and beam control [Fig. 1.9 (e)] [108] which is very useful in optical communications, LADAR (laser detection and ranging) system, optical tweezers, optical trapping and laser beam shaping; ultra-compact metalens [Fig. 1.9 (f)] [98]; Polarisation splitter based on metasurface spin Hall effect [Fig. 1.9 (g)] [109]. Above metasurfaces' functionalities are extremely attractive to currently innovative technology applications, especially those related to integrated optics and photonics that can dramatically shrink the size of the device and make the products look smarter and more portable, such as compact optics in virtual reality (VR), augmented reality (AR) and mixed reality (MR) devices [Fig. 1.9 (h) [114]].

Furthermore, metasurfaces provide prospective solutions to current cutting edge technology research areas, such as quantum dot light enhancement and manipulation [39,115] [Fig. 1.10 (a)], two-dimensional materials photoluminescence enhance-

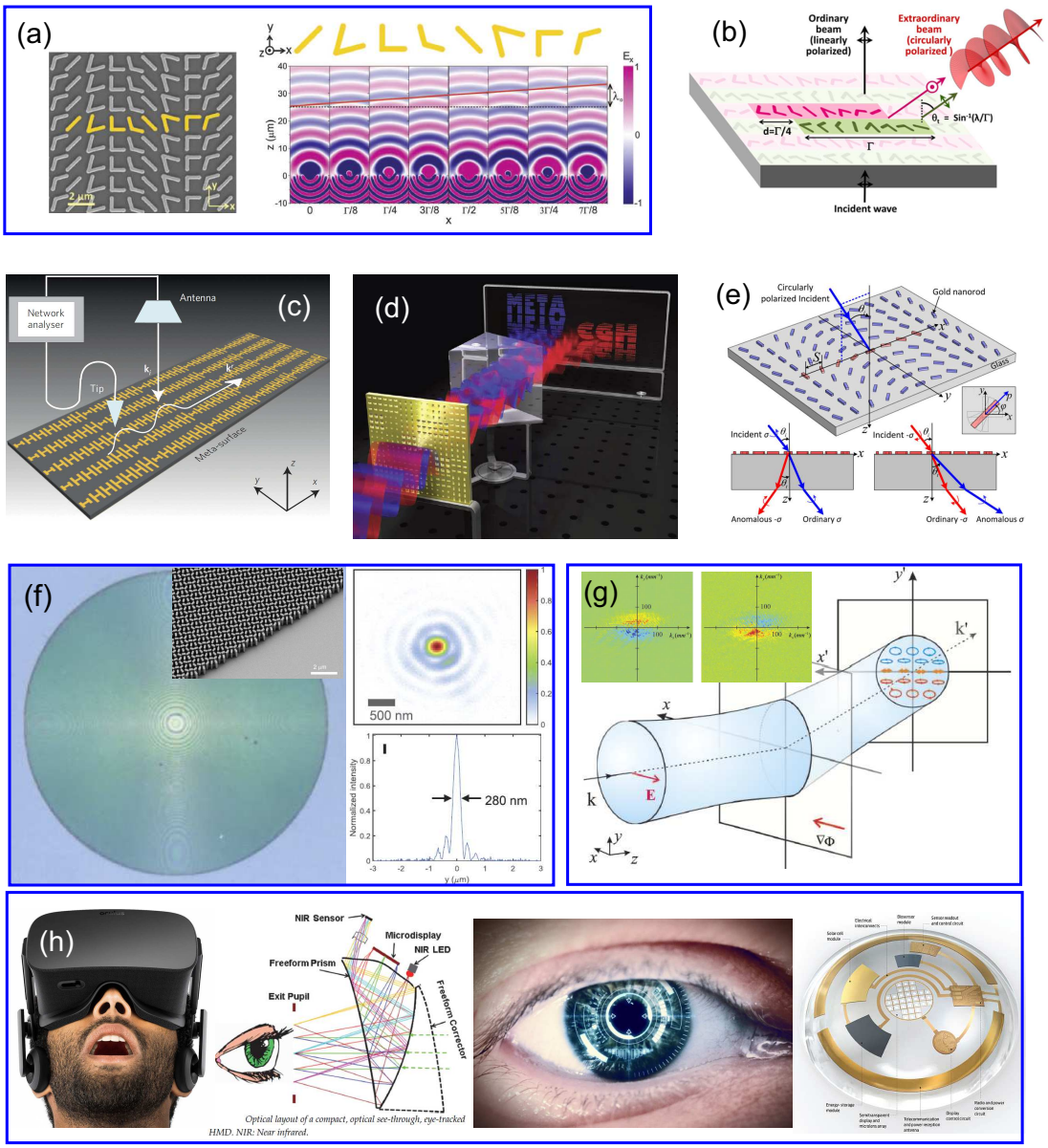

Figure 1.9: (a) Abrupt light phase shifts in the optical path with 50 nm thick metasurface [104]. (b) Metasurface quarter-wave plates can generate high quality circularly polarized light over a broad wavelength range [105]. (c) Metasurface can couple free space planewave to surface wave [106]. (d) Spatially and spectrally shape light fields, and simultaneously contol the amplitude and phase of the transmitted fields by metasurface and this technique can be applied to the holographic imaging [107]. (e) Metasurface composed of dipolar antenna array that can generate an optical vortex beam [108]. (f) Visible-range metalenses with high efficiency and high resolution [98]. (g) A strong photonic spin Hall effect with large splitting of polarized light at metasurface [109]. (h) Virtual reality headset and smart contact lenses [110].

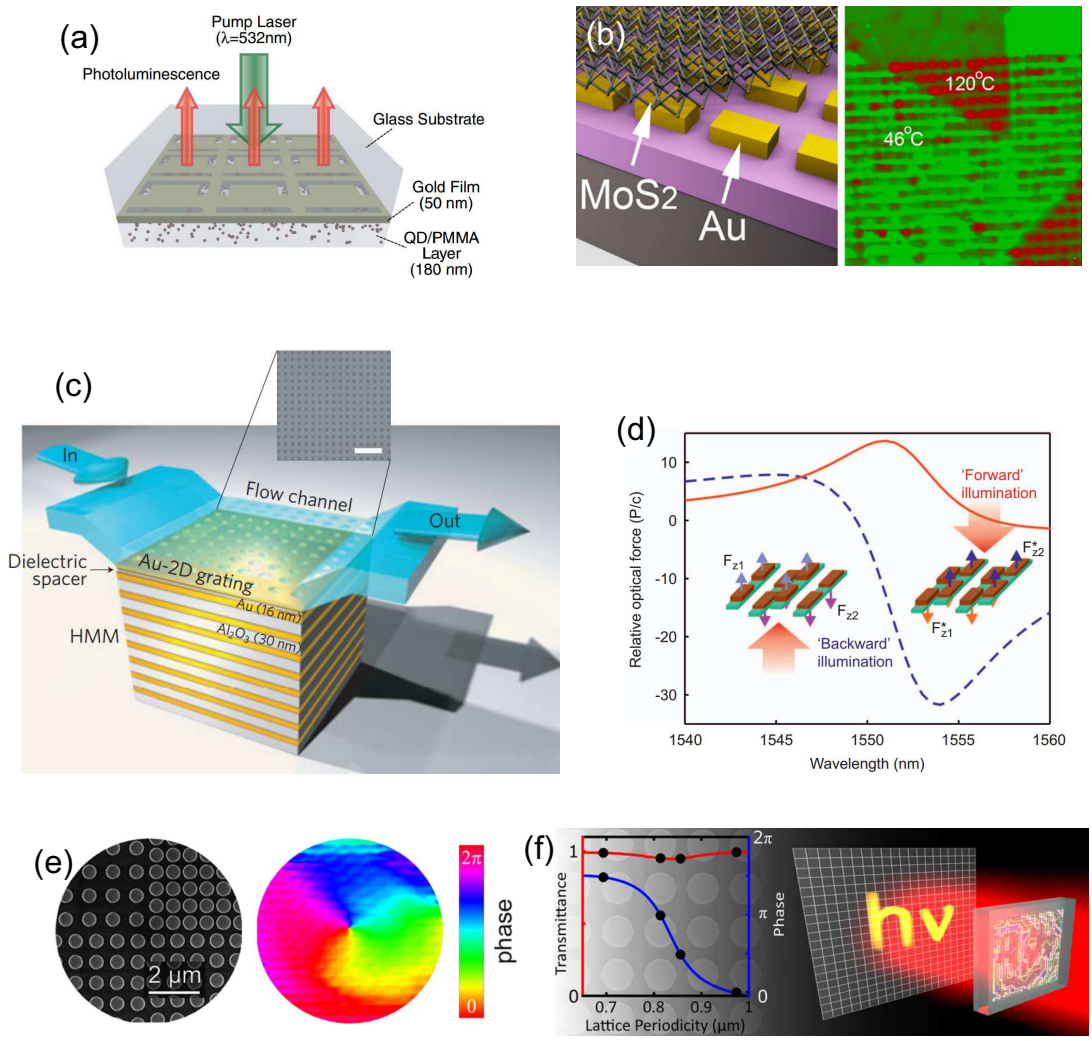

Figure 1.10: (a) Hybridyzing semiconductor quantum dots with plasmonic metamaterials leads to a multifold intensity increase and narrowing of their photoluminescence spectrum [115].(b) Plasmonic metasurfaces give a significant enhancement (65%) of the photoluminescence intensity, clear evidence that the optical properties of the MoS_2 monolayer are strongly influenced by the nanoantenna surface plasmons, which also rise the local temperature [116]. (c) Hyperbolic metamaterials as an optical sensor which offers significant opportunities in the field of medical research and clinical diagnostics, particularly for the detection of small numbers of molecules in highly diluted solutions [117]. (d) Dielectric photonic metamaterial presented a giant nonlinear optical response driven by resonant optomechanical forces [118]. (e) Silicon metasurface at telecommunication wavelengths that can control the wavefront of optical beams with near-unity transmittance efficiency and close to 0-2π phase coverage [119]. (f) High efficiency polarization-insensitive holographic Huygens' metasurface based on dielectric resonant meta-atoms capable of complex wavefront control at telecommunication wavelengths [120].

ment and temperature control [116] [Fig. 1.10 (b)], and high sensitivity bio-sensors that can assist medical research and clinical diagnostics [117] [Fig. 1.10 (c)]. Those metasurfaces are majorly made from noble metals for localized field enhancement and the hyperbolic metamaterials mechanisms. However, for traditional optics, such as lenses and waveplates, it is better to have low loss media with high transparency for the phase and polarization control. In addition, opto-mechanical force systems normally need high quality factor and low energy dissipation as well. Therefore, all dielectric metasurfaces are getting more and more popular in recent years. Such platform can support a giant nonlinear optical response driven by resonant opto-mechanical forces [118] [Fig. 1.10 (d)], near-unity transmission efficiency wavefront control with 0-2π phase coverage [119][Fig. 1.10 (e)], and highly efficient holographic metasurfaces [120][Fig. 1.10 (f)].

1.4 Thesis Outline

Chapter 2 gives an introduction on the directional scattering with Lorentz resonance dipole's phase analysis. In addition, we explain how Fano resonance helps bi-directional scattering which can route light in opposite directions for two different operation wavelengths. We utilize a Fano resonance to tailor the radiation phases of a gold nanodisk and a nanoslit that is inscribed into the nanodisk to realize bidirectional scattering. At last, we show the simulation results that this Fano nanoantenna operates as a bidirectional waveguide coupler at telecommunication wavelengths and, thus, is suitable for integrated wavelength-selective light demultiplexing.

Chapter 3 will continue the previous chapter to present the experimental realization of an ultra-compact plasmonic spectral-band demultiplexer integrated onto an silicon waveguide that couples two wavelength-encoded optical signals in the O and the C band in opposite directions. In addition a ring grating was used for mapping the nanoantenna's directivities at 1550 nm and 1310 nm wavelength, respectively.

In chapter 4 we introduce and investigate directional, polarization-, and mode-selective onchip nanoantennas merged with a silicon rib waveguide. We demonstrate that these nanoantennas can separate polarization-encoded optical signals by coupling different polarizations of light vertically to different waveguide modes propagating into opposite directions. As the central result of this work, we then show the suitability of this concept for the control of optical signals modulated at a frequency of 10 GHz without measurable signal degradation. Our results demonstrate that waveguide-integrated nanoantennas have the potential to be used as ultra-compact polarization- and mode-demultiplexing on-chip devices in high-bit-rate telecommunication applications.

In chapter 5, we study functional hybrid nanoantenna array consisting of metal-dielectric nanoantennas that direct light from an incident plane wave or from localized light sources into a preferential direction. The directionality is obtained by carefully balancing the multipolar contributions to the scattering response from the

constituents of the nanoantenna array. The hybrid nanoantennas are composed of a plasmonic gold nanorod acting as a feed element and a silicon nanodisk acting as a director element. In order to experimentally realize this design, we have developed a two-step electron-beam lithography process in combination with a precision alignment step. The optical response of the fabricated sample is measured and reveals distinct signatures of coupling between the plasmonic and the dielectric nanoantenna elements that ultimately leads to unidirectional radiation of light.

In Chapter 6, we introduce all dielectric metasurfaces that in opto-mechanics and bio-sensing applications.

For opto-mechanics, we investigate a metamaterial where the structural symmetry can be broken by optical forces, giving strong modulation of electromagnetic properties. Since symmetry sets fundamental bounds on the optical response, breaking it controls the metamaterial properties over the entire resonant frequency band. This can be achieved by a polarized pump beam, exerting scattering forces which are not constrained by structural symmetry. We illustrate this concept by introducing a planar metasurface composed of zig-zag chains of dipole meta-atoms, and find that a highly asymmetric force exists for appropriate incident polarization. The effect is employed to transform a planar achiral metasurface into a stereoscopic chiral structure. Importantly, the handedness of the induced chirality can be actively switched to opposite by changing incident polarization. The proposed concept can be employed to achieve dynamic spatial control of metamaterials at infrared and optical frequencies.

For bio-sensing metasurfaces, we demonstrated the results from the real-time microfluidic bioassay measurements. We performed a protein/antibody binding experiment using protein A/G and antibody IgG on functionalized sensor chips. We investigated different amounts of IgG and were able to detect concentrations down to 5 ng/mL, which is competitive with current biosensor designs based on plasmonic nanoholes and even surface plasmon resonance (SPR). In addition, the high light transmission and sharp resonances (5 nm linewidth) of the metasurface make measurements in our setup straightforward and lead to high signal-to-noise ratios.

Chapter 2

Directional scattering and Fano resonances

In this chapter we will introduce the concept of the uni-directional scattering by dipoles interference model. In addition, we will discuss how Fano resonance makes bidirectional scattering. Combining these analysis, we designed a compact single-element Fano nanoantenna that allows for directional coupling of light in opposite directions of a high-index dielectric waveguide for two different operation wavelengths. We utilize a Fano resonance to tailor the radiation phases of a gold nanodisk and a nanoslit that is inscribed into the nanodisk to realize bidirectional scattering. We show that this Fano nanoantenna operates as a bidirectional waveguide coupler at telecommunication wavelengths and, thus, is ideally suitable for integrated wavelength-selective light demultiplexing.

2.1 Introduction

2.1.1 Nanoantennas and light manipulation

Directional farfield scattering by plasmonic nanoantennas is achieved by detuning the resonance wavelengths of two or more antenna elements and, thereby, adjusting their relative phase differences in the radiation fields. This results in constructive interference of radiation in one direction and destructive interference in the other direction. Since the sign of the relative phase difference between the antenna elements usually does not change with the wavelength of the incident light, most of the plasmonic nanoantennas investigated to date are designed for directional scattering of the incident light at one operation wavelength and into one direction only [11, 27, 46–49, 121–124]. However, in order to increase optical data-communication speed and bandwidth it is essential to provide nanoantennas with multi-frequency operation [125] that allow to increase information density by parallel encoding of information at different operation wavelengths (multiplexing). In such a scheme wavelength-selective bidirectional nanoantenna-waveguide coupling to separate information encoded in the wavelength is an essential device for on-chip light demultiplexing. To realize bidirectional nanoantennas, however, a strong relative phase

difference with opposite signs has to be realized.

2.1.2 Fano resonance and bidirectional light scatting

One promising way of achieving this goal is the use of Fano resonances [126, 127] where the constructive and destructive inference of two resonances with very different radiation characteristics provide positive and negative relative radiation phases in a given wavelength range.

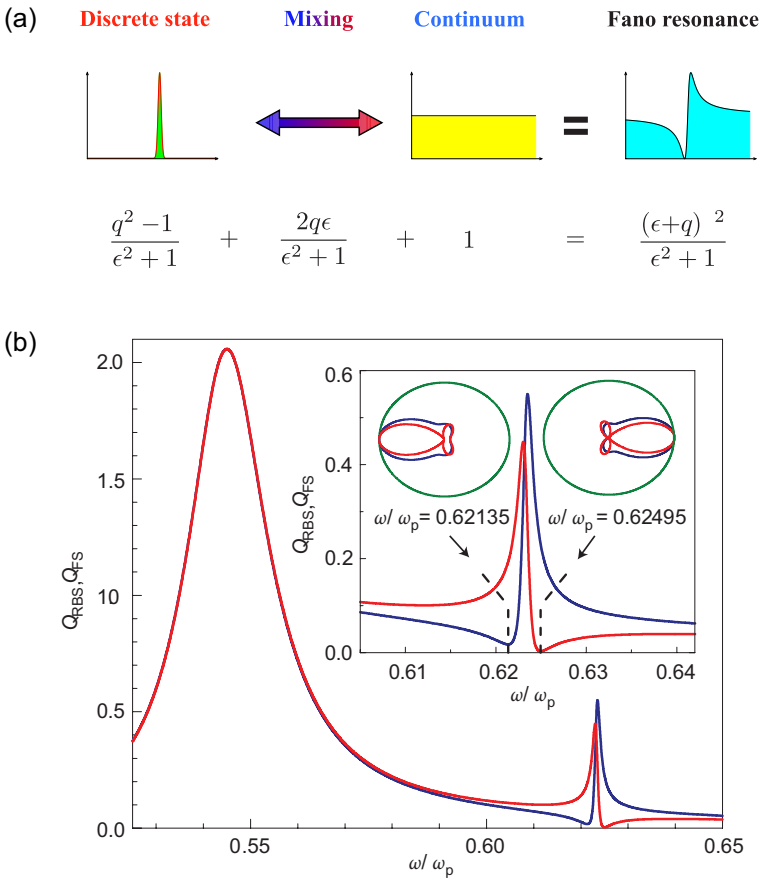

Figure 2.1: (a) Adapted from [127]. Illustration of the Fano formula as a superposition of the Lorentzian line shape of the discrete level with a flat continuous background. (b) Adapted from [126]. Mie scattering against a solid metallic sphere. Radar back scattering (RBS; red) and forward scattering (FS; blue) cross-sections versus normalized frequency ω/ω_p.

Fano resonance is caused by the interference of a discrete autoionized state with a continuum gives rise to characteristically asymmetric peaks in excitation spectra [128]. The Fano resonance lineshape of a scattering cross section can be defined [127]

$$\sigma = \frac{(\epsilon+q)^2}{\epsilon^2+1} \tag{2.1}$$

where ϵ is a reduced energy q is the asymmetry parameter as a ratio of the transition probabilities to the mixed state and to the continuum (Fig. 2.1(a)). This asymmetric resonance can provide bidirectional scattering according to the analytical simulations (Fig. 2.1(b)). Fano resonances in plasmonic nanostructures have already been found to support bidirectional radiation of light from localized quantum emitters [40,42,43], however, studies of bidirectional scattering for farfield excitation are, so far, limited to the directional excitation of surface-plasmon polaritons [27, 46, 47] or the use of the interband transitions of bi-metallic dimers [129] which are all connected with large losses [27, 46, 129] or are not scalable with regard to their operation frequency [129]. Furthermore, a bidirectional nanoantenna design providing the functionality of a bidirectional waveguide coupler for wavelength demultiplexing has not been presented to date.

2.2 Results and discussion

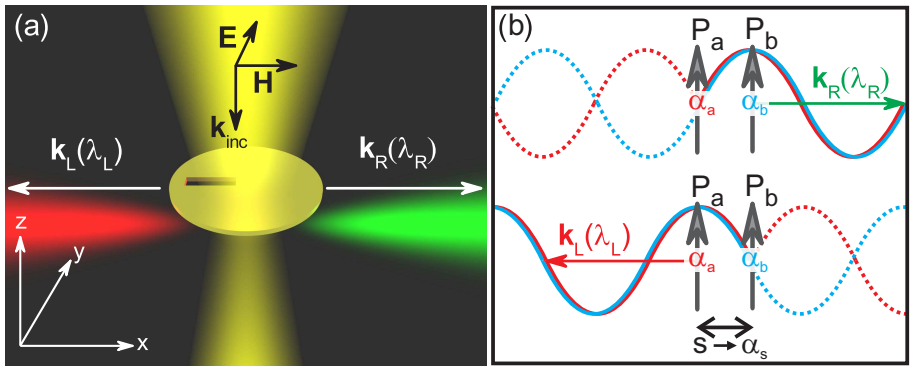

Figure 2.2: (a) Artist view of the bidirectional Fano nanoantenna. The incident broadband light (depicted in yellow) is scattered in opposite directions ($\mathbf{k}_L(\lambda_L)$, $\mathbf{k}_R(\lambda_R)$) for different wavelengths (λ_L red and λ_R green). (b) Dipole scheme showing the interference conditions for bidirectional scattering with $\mathbf{k}_L(\lambda_L)$ and $\mathbf{k}_R(\lambda_R)$.

Here, we present a compact single-particle Fano nanoantenna that shows the capability of simultaneously directing light of two different wavelengths in opposite directions for broadband farfield excitation in free space [see Fig. 2.2(a)]. We demonstrate that this Fano antenna can be integrated onto a high-index dielectric waveguide and can be utilized as a bidirectional waveguide coupler for wavelength demultiplexing. In order to achieve bidirectionality, we effectively merge a rod-shaped aperture antenna and a circular patch antenna into one compact subwavelength nanoparticle. We utilize the interference of the radiation from those two elements that can be regarded as two electric dipoles with very different resonance widths in order to achieve wavelength-selective bidirectional scattering [Fig. 2.2(b)]. The first electric-dipole resonance with a broad linewidth is obtained from a gold nanodisk with a diameter of $d = 400\,\mathrm{nm}$ and a thickness of $h = 30\,\mathrm{nm}$. To realize the second electric-dipole resonance with approximately the same resonance frequency but a narrow

linewidth (as required for the formation of a Fano resonance) we inscribe a 15-nm-wide and 120-nm-long nanoslit in x direction [see Fig. 2.3(a)] and displace it by $s = 100\,\text{nm}$ from the center of the gold nanodisk. To intuitively understand how the Fano-antenna characteristics shown in Fig. 2.3(a) give rise to bidirectional scattering for different operation wavelengths, we describe the two elements of the Fano antenna (the nanodisk and the nanoslit) as two electric dipoles (P_a and P_b) oriented in y direction, one positioned at the nanodisk center and the other at the center of the nanoslit [see inset Fig. 2.3(a)]. The radiation characteristics are then governed by the response of the two (ideal) dipole sources with equal amplitudes $P_a = e^{i\alpha_a}$ and $P_b = e^{i\alpha_b}$, where α_a and α_b represent the phases of the respective dipole radiation [see Fig. 2.2(b)]. Furthermore, the relative displacement $s = 100\,\text{nm}$ of the two dipoles with respect to each other introduces a retardation phase factor α_s. In order to achieve scattering to the left ($-x$ direction), the conditions $\alpha_L = (\alpha_a - \alpha_b) + \alpha_s = 0^o$ (constructive interference to the left) and $\alpha_R = -(\alpha_a - \alpha_b) + \alpha_s = 180^o$ (destructive interference to the right) have to be fulfilled. Likewise, for scattering to the right ($+x$ direction), $\alpha_L = (\alpha_a - \alpha_b) + \alpha_s = 180^o$ (destructive interference to the left) and $\alpha_R = -(\alpha_a - \alpha_b) + \alpha_s = 0^o$ (constructive interference to the right) have to be valid. While one of these two conditions, corresponding to unidirectional scattering only, can be met quite easily, fulfilling both conditions at the same time is impossible for the ideal case of bidirectional scattering with infinite front-to-back ratio (zero back scattering) since this implies that $\Delta\alpha = \alpha_a - \alpha_b = \pm 90^o$ and $\alpha_s = 90^o$ have to be fulfilled simultaneously. However, if one allows non-zero backscattering ($|\Delta\alpha| = \alpha_s$), bidirectional scattering with a maximized front-to-back ratio can be achieved.

In order to investigate the radiation properties of the actual Fano antenna shown in Fig. 2.3(a), we perform numerical calculations using finite-integral frequency-domain simulations (CST Microwave Studio). First we excite the Fano antenna that is suspended in air with a linearly-polarized plane wave incident from the top and calculate the normalized scattering cross section. Figure 2.3(a) shows that the scattering cross section is characterized by a broad resonance with a pronounced maximum at 1100 nm wavelength and a resonance minimum at 800 nm wavelength. To identify the origin of the Fano resonance in our nanoantenna design, we analyze the constituent elements of the antenna, namely the gold nanodisk and the nanoslit, separately. For a single gold nanodisk [Fig. 2.3(b)] with a diameter of $d = 400\,\text{nm}$ and a thickness of $h = 30\,\text{nm}$ we find a broad resonance with a pronounced peak at about 1070 nm wavelength in the scattering cross section [solid line in Fig. 2.3(b)]. This peak can clearly be identified as the main resonance found for the Fano antenna shown in Fig. 2.3(a). To evaluate the phase of the scattered field, we position an electric-field probe in the nearfield of the nanodisk and extract the phase delay. Notably, the large resonance width of the nanodisk is connected with a weak phase dispersion.

Inspired by Babinet's principle [Chapter 1.2.2.5] [17], we investigate the scattering properties of the complementary structure – a single gold nanorod with the same dimensions [Fig. 2.3(c)], in order to analyze the optical response of the nanoslit. According to Babinet's principle, the radiation pattern of the nanoslit is identical in shape to that of a nanorod except that electric and magnetic fields are inter-

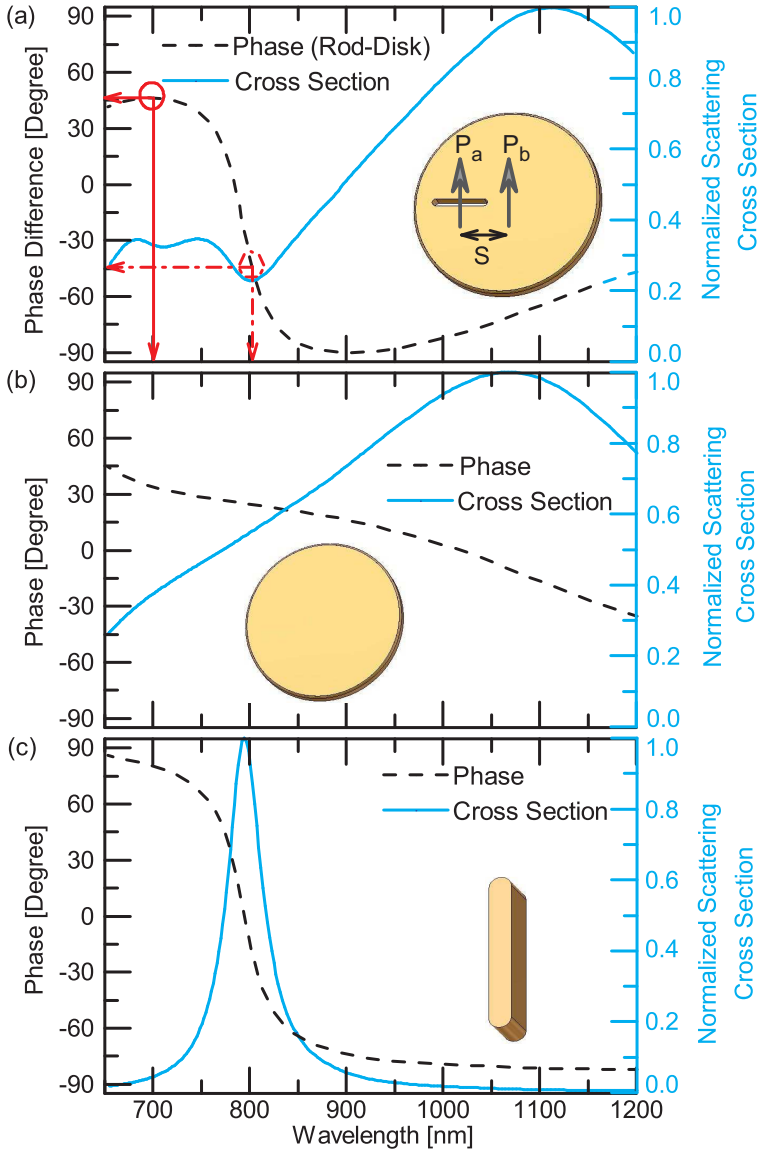

Figure 2.3: (a) Normalized scattering cross section (blue curve) and the phase difference between the single nanorod and the nanodisk (black dashed curve). The inset shows the Fano antenna design. The two arrows indicate the dipoles P_a and P_b representing the nanoslit and the nanodisk, respectively. At 702 nm (phase difference of $+47$ degrees) and at 808 nm (phase difference of -45 degrees) bidirectional scattering occurs. (b) Normalized scattering cross section (blue curve) and phase spectrum (black dashed curve) of a single gold nanodisk with a diameter 400 nm and a thickness 30 nm. (c) Normalized scattering cross section (blue curve) and phase spectrum (black dashed curve) of a gold nanorod with a length of 120 nm, a width of 15 nm and 30 nm thickness.

changed [17, 130]. In order to describe the response of the nanoslit that is excited by an incident electric field perpendicular to the slit by its complementary structure,

a nanorod, the orientation of the nanorod has to be parallel to the polarization of the incident light. Thus, we calculate the response of a gold nanorod with the same dimensions as the nanoslit in the final nanoantenna design but with perpendicular orientation [see Fig. 2.3(c)]. Notably, since Babinet's principle is not exact for (lossy) optical metals, the nanoslit resonance is slightly blueshifted and spectrally broadened as compared to the nanorod resonance, however, these small deviations do only marginally affect the results obtained from the dipole model. We find that the nanorod shows a resonance (scattering peak) at 800 nm wavelength that can be linked to the resonance of the nanoslit. Furthermore, the nanorod resonance is relatively narrowband in comparison to the resonance of the nanodisk. This is connected with a strong phase dispersion in the scattered field at 800 nm wavelength. The interference of the radiation of the nanodisk and the nanoslit in the final nanoantenna design ultimately leads to a Fano resonance in the scattering cross section at 800 nm wavelength as can be seen in Fig. 2.3(a). Furthermore, the Fano resonance results in a relative phase difference $\Delta\alpha$ of the scattered field of the nanodisk and the complementary nanoslit that is positive for wavelengths smaller than approximately 790 nm and negative for wavelengths above this value [dashed line in Fig. 2.3(a)]. Specifically, we obtain $\Delta\alpha = \alpha_a - \alpha_b = -45^o$ at 808 nm wavelength and $\Delta\alpha = \alpha_a - \alpha_b = +47^o$ at 702 nm wavelength for our actual Fano antenna design. Because of the fixed displacement of the two dipoles $s = 100$ nm at 808 nm wavelength, the retardation phase is fixed to $\alpha_s \approx 45^o$. As a result, we expect our Fano antenna to support scattering to the right at 702 nm wavelength and to the left at 808 nm wavelength for excitation with a y polarized wave propagating in $-z$ direction [Fig. 2.2(a)].

To verify the bidirectional scattering of our Fano antenna we now calculate the radar cross sections RCS_R in $+x$ direction and RCS_L in $-x$ direction and plot the corresponding (black and red) curves in Fig. 2.4(a). Clearly at 702 nm wavelength, the right scattering cross section (RCS_R) is maximized while the left scattering (RCS_L) is minimal and *vice versa* at 808 nm wavelength. Furthermore, the side scattering ratios $SSR_R = RCS_R/RCS_L$ and $SSR_L = RCS_L/RCS_R$ as depicted in Fig. 2.4(b) exceed 17 for both scattering directions. The calculated directivity of the Fano antenna in $+x$ (at 702 nm) and $-x$ (at 808 nm) direction is 2.4 and 2.8, respectively.

In the next step, we integrate the bidirectional Fano antenna onto a chalcogenide-glass waveguide to couple light with different wavelengths into opposite waveguide directions. We excite the antenna that is immersed in a droplet of index-matching liquid with the y-polarized mode of a tapered optical fibre (core diameter of 1 μm) from the top [see Fig. 2.5(a,b)]. The waveguide width is 600 nm, height is 580 nm, and the refractive index of the chalcogenide glass is 2.65. The refractive index of the glass substrate, the index-matching liquid, and the glass fibre is 1.45. To quantify the amount of light coupled into the waveguide in $+x$ and $-x$ direction we monitor the energy flow at the faces at each end of the waveguide. We then calculate the direction-dependent coupling efficiencies, *i.e.*, the power flow through each of the faces normalized to the incident power flow from the fibre port. In doing so we obtain the spectrally-resolved coupling efficiencies η_L and η_R for the left and the right wavguide face [Fig. 2.5(c)]. For the Fano antenna integrated onto a chalcogenide

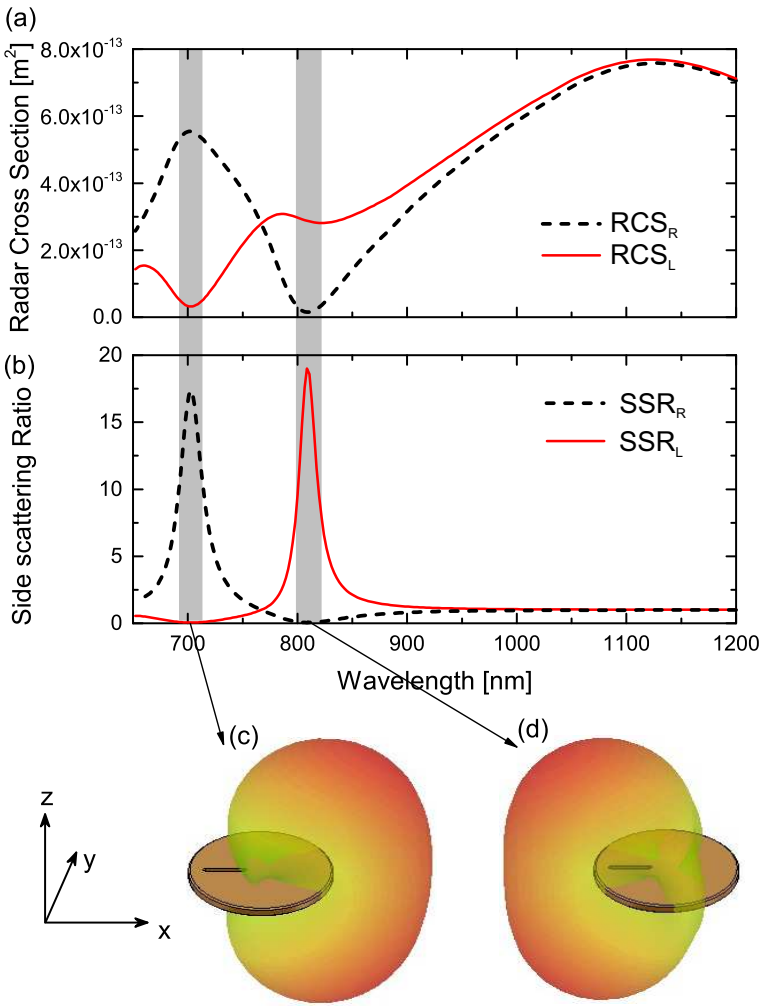

Figure 2.4: (a) Radar cross section RCS_R for scattering to the right ($+x$ direction) and RCS_L for scattering to the left ($-x$ direction). (b) Side scattering ratios $SSR_R = RCS_R/RCS_L$ (black dashed curve) and $SSR_L = RCS_L/RCS_R$ (red solid curve). Radiation pattern at (c) 702 nm and (d) 808 nm wavelength.

waveguide, we obtain maximum coupling efficiencies of $\approx 5\%$ for each direction. This is quite impressive considering the subwavelength scale of both the nanoantennas and the waveguide.

Figure 2.5(d) finally shows the fidelity of the directional coupling, *i.e.*, the ratios of the power coupled to the opposite waveguide directions for each wavelength. In our calculations we obtain a maximum fidelity of 11 for coupling to the right direction at 1250 nm wavelength and a fidelity of 6.2 at 1610 nm for coupling to the left direction. At a wavelength of around 1530 nm and 1380 nm we get a comparable fidelity of about 3.3 for both directions. For these two cases we additionally plotted the y component of the electric field in a cutting plane through the center of the waveguide. Figure 2.5(e) and (f) visualize the bidirectional coupling that is realized

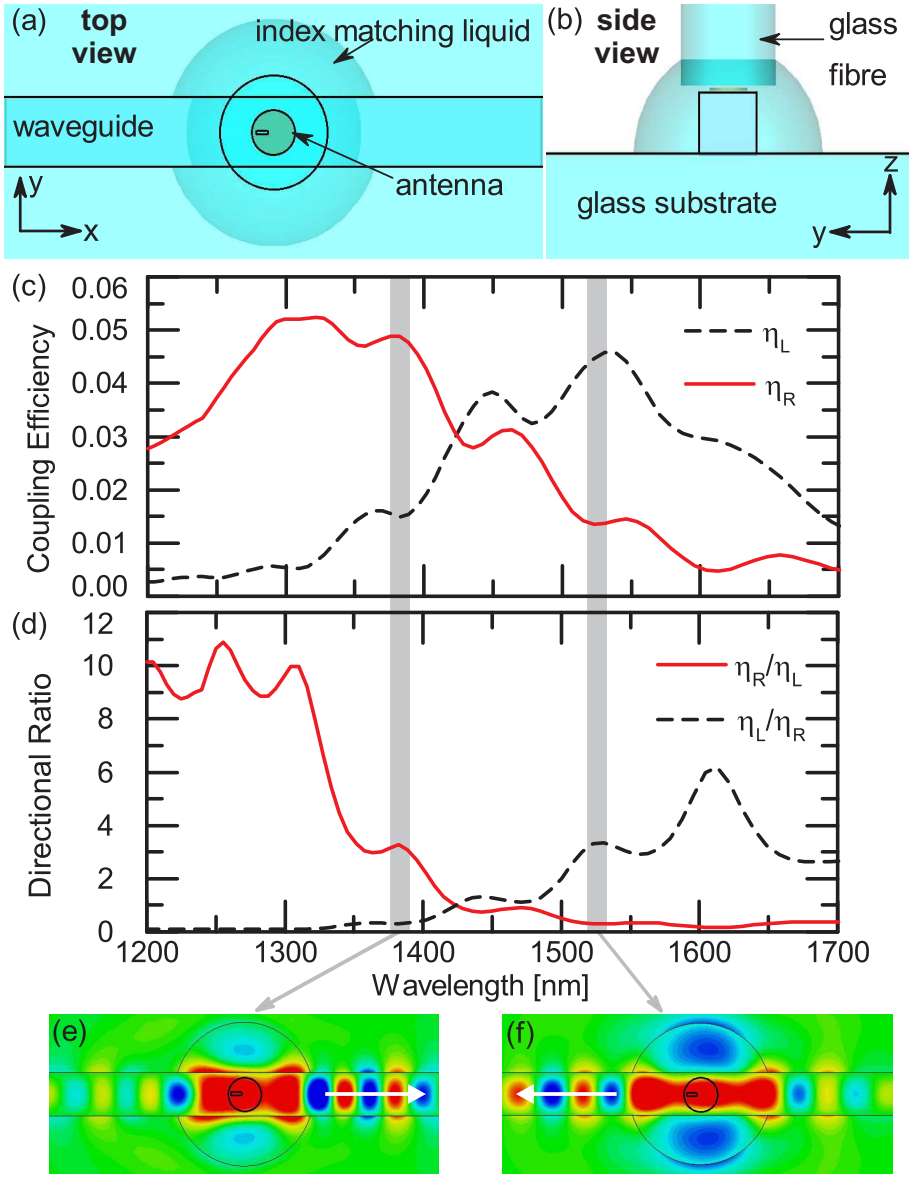

Figure 2.5: (a) Top view and (b) side view of the Fano nanoantenna on a chalcogenide-glass waveguide. The antenna is excited by a glass fibre from the top. (c) Coupling efficiencies in $+x$ direction (η_R, red solid curve) and in $-x$ direction (η_L, black dashed curve) of the waveguide. (d) The directional ratio η_R/η_L (red solid curve) and η_L/η_R (black dashed curve) defines the fidelity of the directional coupling. (e,f) Top-view color plots of the y component of the electric field in a cutting plane through the center of the waveguide.

at around 1380 nm and 1530 nm wavelength showing clearly that, for the two selected wavelengths, the waveguide mode is launched mostly in one direction.

Phase matching is crucial to couple light efficiently from free space into the

waveguide as guided modes. There are two important factors to achieve an efficient coupling. Firstly, we should calculate the effective wavelength of the guided mode, and use the effective wavelength to calculate the phase matching condition. Secondly, we need to calculate the nanoantennas' resonances and phases in the according effective medium rather than in the air.

2.3 Summary

In summary, we have introduced a single-element nanoantenna consisting of a gold nanodisk and a Babinet-inverted nanorod (nanoslit). We have shown that this nanoantenna exhibits a pronounced Fano response that can be exploited to generate bidirectional radiation patterns for different wavelengths of light with a maximum side-scattering ratio of approximately 17 for opposite directions. We also demonstrate that this bidirectional Fano antenna can be integrated onto dielectric waveguides and can provide an on-chip solution for two-colour routing that may lead to compact devices for wavelength-selective waveguide demultiplexing. Finally, due to the Fano resonance, the antenna properties are inherently sensitive to changes in the dielectric environment which makes this Fano antenna a promising candidate for integrated sensing applications.

Chapter 3

On-chip wavelength demultiplexing nanoantenna

In the previous chapter, we discussed about the Fano resonances which can make bidirectional scattering of light, and this phenomenon can be applied to nano wavelength demultiplexing by a single plasmonic nanoantenna for the compact integrated telecommunication applications. Therefore, in this chapter, we will discuss further about experimental realization of an ultracompact plasmonic spectral-band demultiplexer for telecommunication wavelengths integrated onto an optical waveguide that couples two wavelength-encoded optical signals in the O and the C band in opposite directions of a silicon waveguide. In this way, we demonstrate a plasmonic key element for on-chip optical data processing that can also be used as a functional link between on- and off-chip optical signals.

3.1 Introduction

Due to their ability to confine light to subwavelength volumes [35] plasmonic nanoparticles and nanoantennas provide a fundamental link between electronic and photonic circuits as they can bridge the large size mismatch between the electronic and photonic wave functions [131, 132]. As a result, plasmonic elements can be utilised to increase the integration density and performance of active and passive photonic devices. In this context, many ultrafast and compact devices with designed functionalities have been suggested, including plasmonic photo detectors [14, 133–136], modulators [137, 138], plasmonic waveguides [131, 139], and plasmonic waveguide couplers [27, 46, 47, 140, 141]. Furthermore first experimental demonstrations of directional waveguide coupling have been achieved very recently [142–145]. However, an ultra-compact plasmonic realisation of an optical demultiplexer that is suitable for on-chip signal processing is still missing. Here we suggest the concept of hybrid plasmonic-dielectric devices and realise an ultra-compact plasmonic spectral-band demultiplexer for telecommunication wavelengths integrated onto an optical waveguide. In contrast to conventional large-scale optical wavelength demultiplexers based on prisms, gratings, Mach-Zehnder interferometers, or spectral filtering that are difficult to miniaturise, we develop and realise a submicron-sized two-directional

nanoantenna that additionally provides an interconnect between free-space and on-chip photonic circuitry. Key to the device functionality is to realise an antenna with the capability of simultaneously directing light of two different wavelengths in opposite directions. Since most of the conventional nanoantennas only provide unidirectional scattering characteristics [36, 121, 123–125], these designs are not suitable for multiplexing applications. Our design utilises the concept of Fano resonances [40,43,124,126,146] in plasmonic nanostructures for tailoring the nanoantenna scattering properties in order to separate two wavelength-encoded optical signals. In this way, we demonstrate a plasmonic key element for on-chip optical data processing that can also be used as a functional link between on- and off-chip optical signals.

Unidirectional scattering or emission of radiation in commonly used nanoantenna designs like Yagi-Uda antennas [36], for example, is typically achieved by detuning the resonance wavelengths of two or more antenna elements. In this way the relative phase differences in the radiation fields of the individual antenna elements are adjusted to realise constructive interference in one direction and destructive interference in the other direction. However, in order to be able to spatially separate optical signals encoded at different operation wavelengths one requires a nanoantenna that operates at (at least) two different wavelengths and supports unidirectional scattering in different directions at each operation wavelength. A solution to enable such multi-wavelength functionality is the use of Fano resonances [126] which are known to provide an alternative way of designing farfield radiation patterns [124, 146] and emission patterns of localised light sources [40, 42, 43]. However, the concept of Fano resonances has never been applied in order to design multi-directional scattering in plasmonic nanoantennas, the fundamental prerequisite for being able to divide wavelength-encoded optical signals.

3.2 Results and discussion

We will use the design ideas of the previous chapter, and applied it to the experimental realization. With the same design as chapter 2, we effectively merge a rod-shaped aperture antenna (nanoslit) and a circular patch antenna (nanodisk) into one compact subwavelength nanoparticle. These two elements combine a broad nanodisk resonance with a comparably narrow resonance from the nanoslit that are strongly coupled to each other via the electric currents within the single particle. As a result, they give rise to a Fano resonance in the scattering spectrum which, in turn, enables directional scattering of light with different wavelengths in different directions. This Fano nanoantenna, which is designed for operation at the O- and the C-band in the near-infrared, is then processed on top of a silicon-slab waveguide on a silicon-on insulator (SOI) wafer that is used to guide the scattered light from the antenna. Our directional nanoantenna then couples incident light of different wavelengths into different propagation directions in the slab-waveguide [see Fig. 3.1(a),(b)] and, hence, can be used to spatially separate optical signals. A scanning electron microscopy image of a typical Fano nanoantenna is depicted in Fig. 3.1(c)). Furthermore, in order to

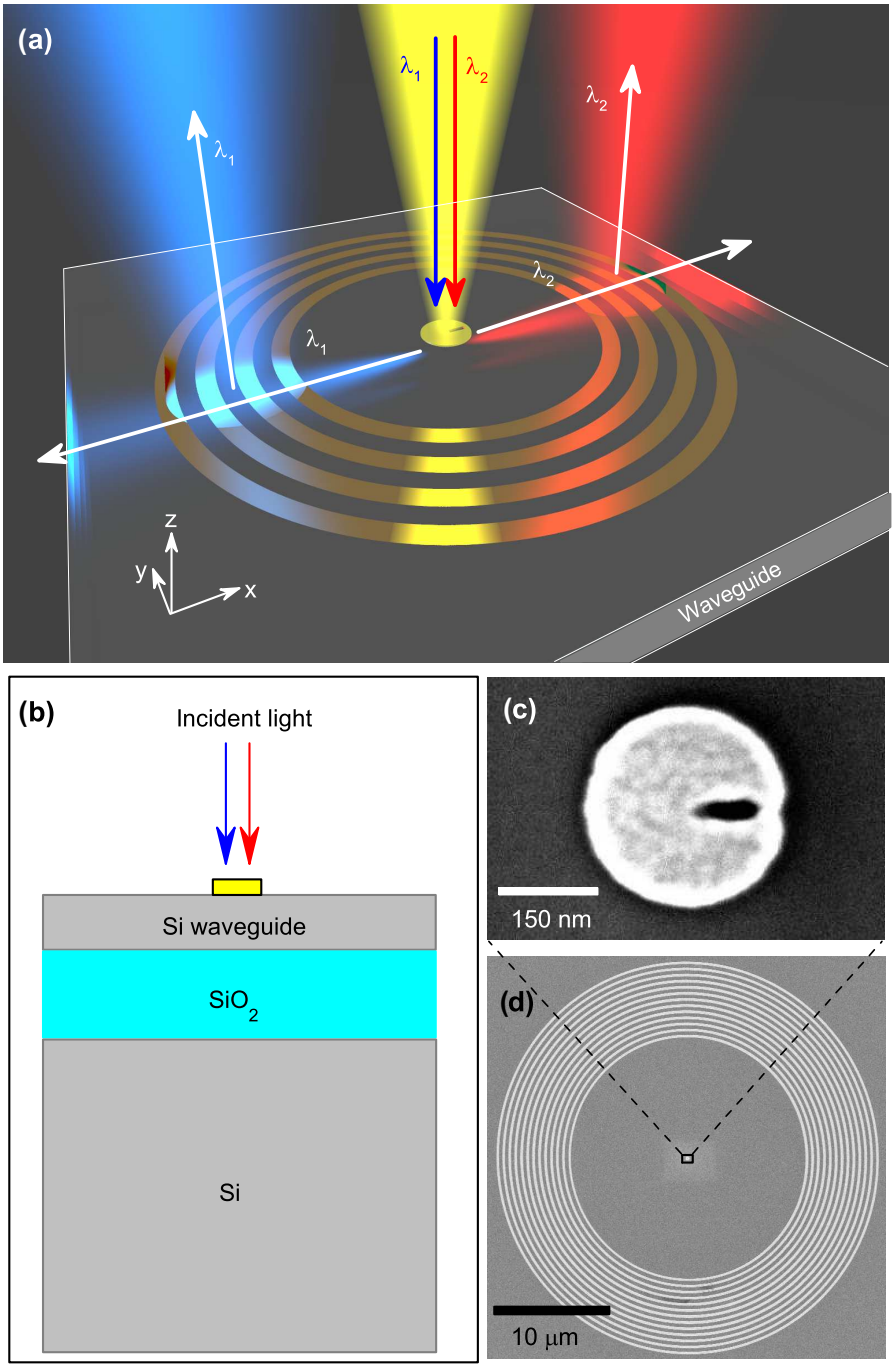

Figure 3.1: (a) Schematics of the wavelength-demultiplexing nanoantenna on a slab waveguide with a circular ring-grating for detection. (b) Experimental configuration of the nanoantenna on a silicon-on-insulator wafer. (c),(d) Scanning-electron-microscope image of the fabricated nanoantenna (c) and circular grating (d) on top of the silicon-slab waveguide. The radius of the inner ring of the grating is 10 μm and the size of the incident laser beam is 2 μm (FWHM).

detect the radiation that is coupled into different directions of the silicon waveguide by the nanoantenna, we process an additional gold ring-grating coupler centred on the nanoantenna [see Fig. 3.1(a),(d)]. This allows us to measure the angle-resolved directivity pattern within the silicon waveguide and, most importantly, to separately detect the different wavelength-encoded optical signals at two opposite outputs. According to the previous chapter, the rod-shaped aperture antenna (nanoslit) and the circular patch antenna (nanodisk) combine a broad nanodisk resonance with a comparably narrow resonance from the nanoslit that are strongly coupled to each other via the electric currents within the single particle. As a result, they give rise to a Fano resonance in the scattering spectrum which, in turn, enables directional scattering of light with different wavelengths in different directions.

In a first step, we numerically tailor the scattering properties of our bi-directional plasmonic Fano nanoantenna and identify the nanoantenna parameters for operation at the two telecommunication bands at $\lambda_1 = 1310\,\text{nm}$ (O-band) and $\lambda_2 = 1550\,\text{nm}$ (C-band). This results in a circular gold nanodisk with a diameter of $d = 300\,\text{nm}$ and a gold thickness of $h = 30\,\text{nm}$ and a 18-nm-wide and 100-nm-long nanoslit which is displaced by 60 nm from the center of the disk in $+x$-direction. For the numerical calculations we use the finite-element frequency-domain solver of the software package CST Microwave Studio. In order to calculate the scattering properties of the nanodisk/nanoslit antenna, we first embed the nanoantenna in an effective medium with a refractive index of $n = 2.1$ that emulates the influence of the SOI wafer in experiment. We then excite the nanoantenna with a y-polarised plane wave incident from the top and calculate the normalised scattering cross section. Fig. 3.2(a) shows that the scattering cross section (black solid line) of the nanoantenna which is characterised by a broad resonance with a pronounced maximum at $\lambda \approx 1900\,\text{nm}$ wavelength and a resonance minimum at $\lambda \approx 1300\,\text{nm}$ wavelength. To identify the origin of the resonance in our nanoantenna design, we separately analyse the constituent elements of the nanoantenna, namely the gold nanodisk and the nanoslit. For the single gold nanodisk, i.e. without nanoslit, we find a broad resonance with a pronounced peak at approximately 1800 nm wavelength in the scattering cross section that matches the main peak in the scattering cross section of the final nanoantenna design (red dashed line). In order to investigate the resonance properties of the nanoslit we calculate, inspired by Babinet's principle, the scattering properties of its complementary structure – a single gold nanorod identical in dimensions to the nanoslit (blue dashed line). The gold nano-rod shows a pronounced and spectrally narrow resonance peak at approximately 1300 nm wavelength where the resonance dip for the final nanoantenna design is observed. This behaviour is indeed evidence for the presence of a Fano resonance in the optical response of the nanodisk/nanoslit antenna since at this spectral position the narrow resonance of the nanoslit destructively interferes with the broad resonance of the nanodisk. In a second step, we numerically calculate the angle-resolved coupling directivity of the nanoantenna on top of a 220-nm-thin silicon slab waveguide, i.e. the intensity of light coupled in one waveguide direction normalised to the total intensity coupled into the waveguide, for the two operation wavelengths λ_1 (O-band) and λ_2 (C-band) of the antenna.

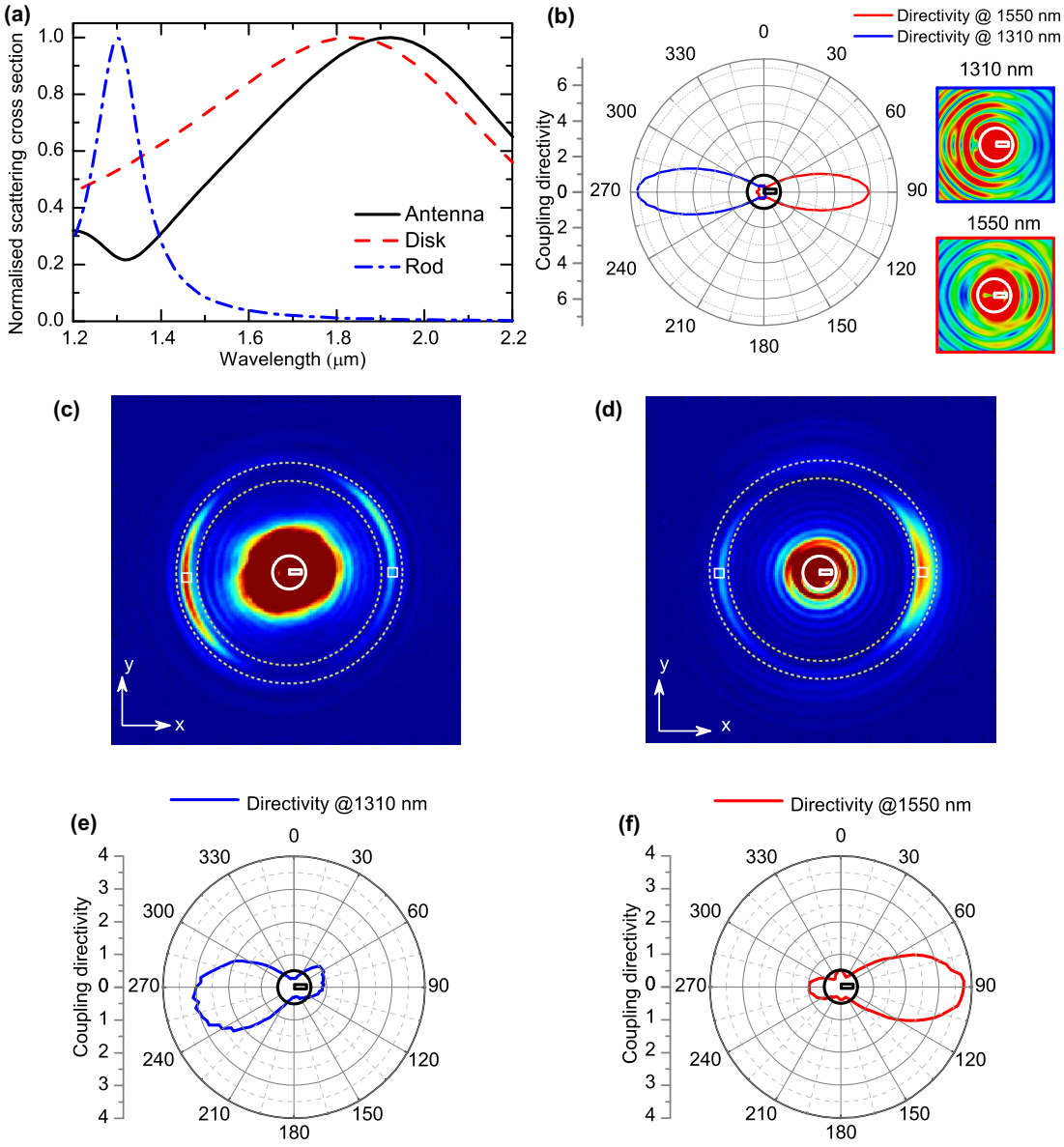

Figure 3.2: (a) Calculated scattering cross section of the nanoantenna embedded in a medium with $n = 2.1$ and its constituent elements, a gold nanodisk and a nanorod. (b) Calculated directivity of light coupling into the waveguide for the two operation wavelengths. (c),(d) Experimental CCD image (raw data) for y-polarised illumination of the antenna at a wavelength of (c) $\lambda_1 = 1310\,\text{nm}$ and (d) $\lambda_2 = 1550\,\text{nm}$. The antenna (not to scale) is indicated as white outline. (e),(f) Directivity extracted from (c),(d) by evaluation of the outcoupled power from the ring grating [white-dashed lines in (c),(d)].

These results are shown in Fig. 3.2(b) and show that at $\lambda_1 \approx 1310\,\text{nm}$ wavelength the nanoantenna shows highly directional waveguide coupling with a maximum coupling directivity of around 7 to the left ($-x$-direction) of the waveguide while

at $\lambda_2 \approx 1550\,\text{nm}$ wavelength the light is coupled to the right with a directivity of around 6. Hence, our nanoantenna supports two-directional waveguide coupling when integrated onto a silicon waveguide. Although the antennas are designed for plane wave incidence, we focus the incident laser beam on the antenna to increase the energy density and therefore the absolute detection intensity.

Next, we fabricate the nanoantenna on a silicon-on insulator wafer [see Fig. 3.1(b)]. To detect the radiation that is coupled into different directions of the silicon waveguide by the nanoantenna we image the light coupled out by the circular grating onto an InGaAs CCD camera [Fig. 3.2(c),(d)]. In this way, we can spatially separate and analyse the two wavelength-encoded optical signals. Furthermore, the circular ring grating allows us to directly extract the angle-resolved directional coupling pattern into the silicon waveguide for the two operation wavelengths λ_1 and λ_2. The measured patterns are shown in Fig. 3.2(e),(f) and confirm directional waveguide coupling of the incident light to the left and right with a maximum coupling directivity of approximately 3 and 4, respectively. In order to estimate the coupling efficiencies of light into the waveguide at the two operation wavelengths, we calculate the ratio of the power collected from the left/right half of the ring grating divided by the power of the incident light and obtain coupling efficiencies of 3.3% for $\lambda_1 = 1310\,\text{nm}$ wavelength and 5.8% for $\lambda_2 = 1550\,\text{nm}$ wavelength, respectively. These waveguide-coupling efficiencies assume a grating outcoupling efficiency of about 25% for $\lambda_1 = 1310\,\text{nm}$, and 30% for $\lambda_2 = 1550\,\text{nm}$ gained from numerical simulations.

In the previous paragraphs, we discussed the nanoantenna couples light into the slab waveguide and we can observe the coupling directivity from the nanoantenna by a ring grating. Furthermore, we can do an inverse experiment that confirm if this phenomenon can be done inversely. This time, we excite left and right side of the ring grating and study how nanoantenna reacts with it. We firstly applied 1550 nm laser to excite right side of the ring grating [Fig. 3.3(b)] comparing to excite left side of the ring grating [Fig. 3.3(c)] with the same laser power. Apparently, we can see the nanoantenna decouples light from right waveguide mode excitation is much stronger than the left waveguide mode excitation. We did the same experiment with 1310 nm laser, and we observe the opposite results according to [Fig. 3.3(d), (e)].

Finally, we demonstrate on-chip spectral band separation with the use of our Fano nanoantenna on the silicon waveguide. We modulate the light of the two laser sources at two different modulation frequencies ($f_1 = f_{\lambda 1} = 1.48\,\text{Hz}$, $f_2 = f_{\lambda 2} = 1.78\,\text{Hz}$) utilizing a two-frequency chopper and combine the two signals into a single beam with a beam splitter. We then focus the combined laser beam onto the sample [see Fig. 3.4(a)]. The two wavelength-encoded signals are then directionally coupled into the waveguide by the nanoantenna. After propagating to the left/right, the light is outcoupled by the circular grating on the left/right. We then monitor the time-dependent total intensity $I_{tot} = I_{\lambda 1} + I_{\lambda 2}$ at the each of the two opposite output ports by evaluation of the CCD camera images at the positions shown in Fig. 3.2(c). The measured signal at the output port on the left and on the right is plotted in Fig. 3.4(b) in blue and red, respectively, depicting the time-traces of a typ-

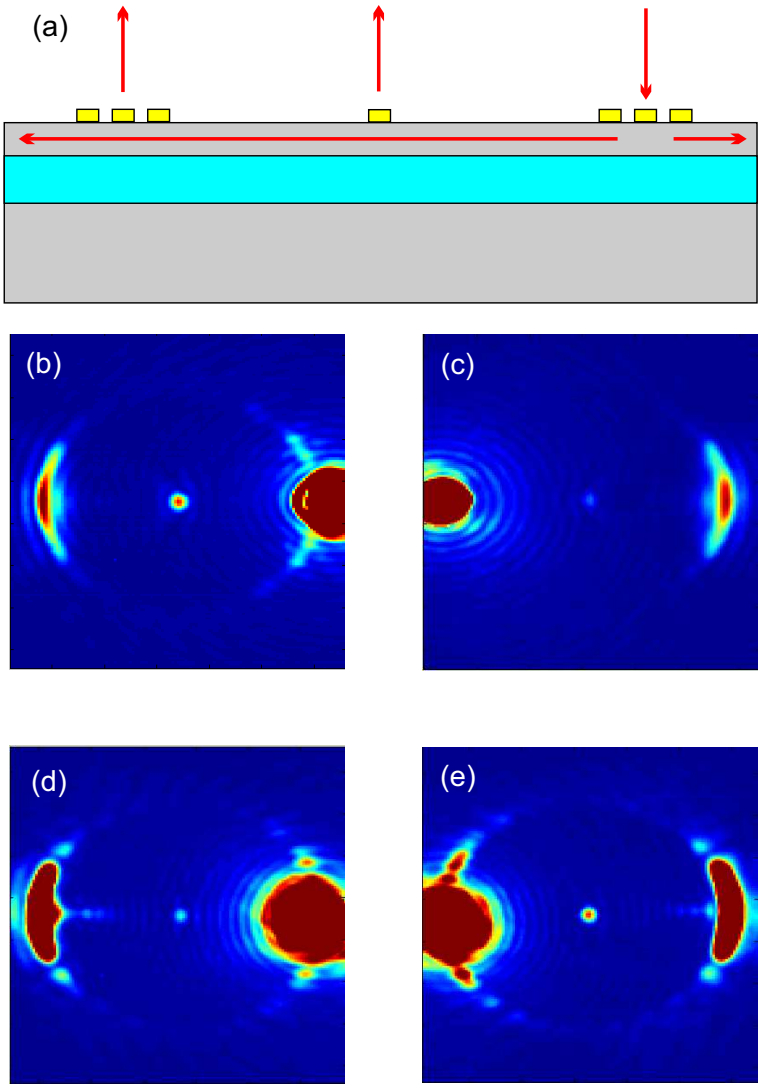

Figure 3.3: (a) Schematics of the experiment. Laser light excites one side of the ring grating, which couples light into the waveguide, and the waveguide light is decoupled by an antenna and the other side of the ring grating. A 1550 nm laser coupled into the waveguide from the right (b) side of the grating and the left (c) side of the grating. A 1310 nm laser coupled into the waveguide from the right (d) side of the grating and the left (e) side of the grating.

ical signal recorded at the respective ports in a time intervall of five seconds. For each port on the waveguide the corresponding wavelength-encoded signals with the two frequencies $f_1 = 1.48\,\mathrm{Hz}$ and $f_2 = 1.78\,\mathrm{Hz}$ are nicely separated and recovered. In order to clearly identify the frequency-components that are measured, we perform a Fourier analysis of a 2.5 minutes-long timetrace at each output port. From the frequency analysis shown in Fig. 3.4(c) we can identify two frequency peaks, one main peak at each port, at the two modulation frequencies of the combined in-

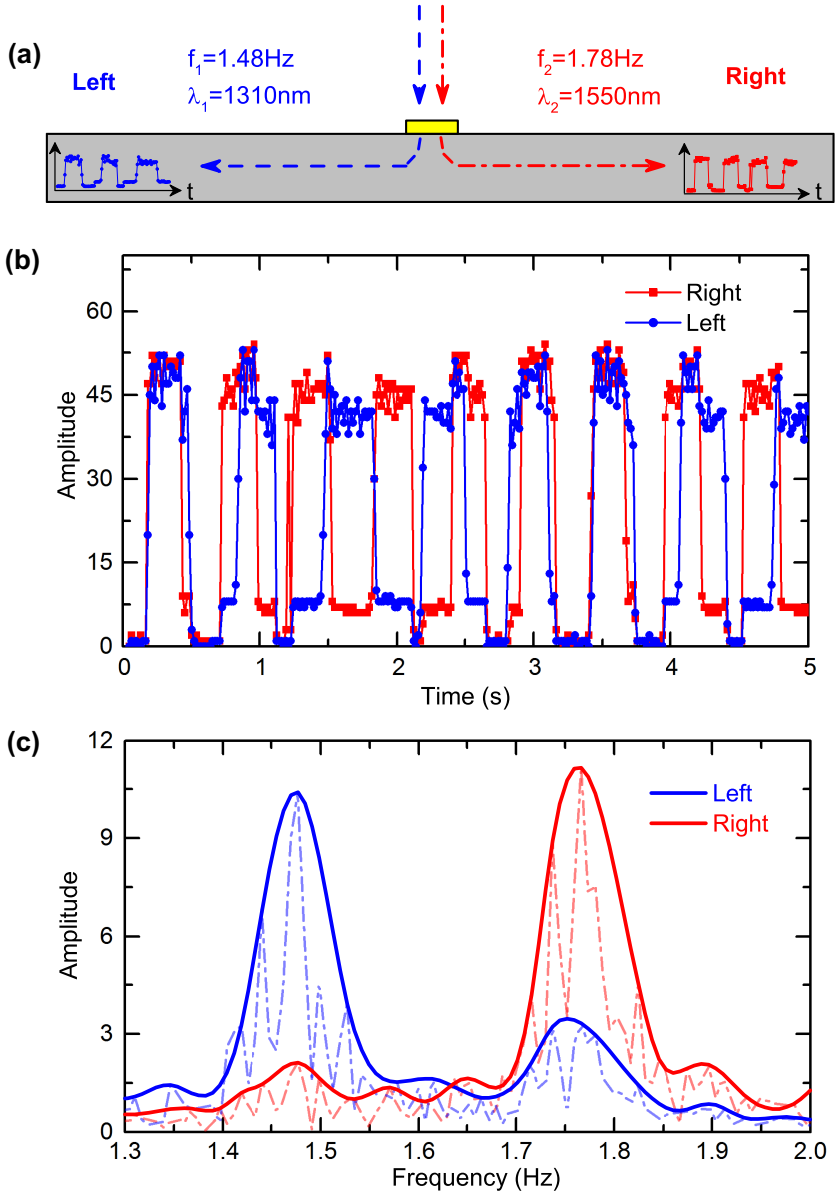

Figure 3.4: (a) Schematics of the experiment. Two optical signals with $f_1 = 1.48\,\mathrm{Hz}$, $f_2 = 1.78\,\mathrm{Hz}$ are encoded at $\lambda_1 = 1310\,\mathrm{nm}$, $\lambda_2 = 1550\,\mathrm{nm}$ wavelength and coupled to the left, right by the nanoantenna. The corresponding signals are outcoupled by the grating and detected by a CCD camera. (b) Detected time signal at the left and the right output port and (c) Fourier analysis of the detected intensity at the two outputs confirming that the two original signals have been well separated by the nanoantenna. The raw data are plotted as dash-dotted lines with the corresponding envelopes (solid lines).

put beam confirming that the two modulated signals are very well separated by this wavelength-demultiplexing nanoantenna. The width of each resonance and, hence,

the frequency spread of the two signals is mainly determined by the frequency variation of the input signal due to the chopper used in the experiment. Notably, the operation frequency of our wavelength demultiplexing integrated nanoantenna is only limited by the technical limitations of the camera used in the experiment which is fixed to a sampling rate of 59 frames per seconds. There is no fundamental limit for operation at THz frequencies.

3.3 Sample fabrication

To fabricate nanoantenna-grating samples, we performed three-step electron-beam lithography (EBL) on silicon on insulator (SOI) wafer (220 nm top silicon thickness, 2 μm buried oxide thickness). In the first step, we fabricated a single Au Fano antenna. Firstly, we spin coated PMMA495A2 resist with 1000 rpm for 1.5 min, before 3 min and 180 C hotplate post baking. Then we performed EBL. After electron-beam exposure (with 30 kv voltage, 7.5 μm aperture, 600 μC/sqcm dose), development was performed using cold 1:3 MIBK to IPA with a development time of 35 s, followed by a rinse in isopropanol for 30 seconds. After the first lithography, we applied E-Beam evaporator deposition process for 30 nm Au film. After deposition, we immersed sample into hot acetone for lifting-off the gold film. In the second step, we fabricated alignment markers around each of the nanoantennas. Firstly, we spin coated PMMA950A4 resist with 4000 rpm for 1.5 min, before 3 min 180 C hotplate post baking. Then we performed EBL for markers. After electron-beam exposure (with 30 kv voltage 7.5 μm aperture, 600 μC/sqcm dose), development was performed using cold 1:3 MIBK to IPA with a development time of 35 s, followed by a rinse in isopropanol for 30 seconds. After the second lithography, we deposited 30 nm Au film by using E-Beam evaporator. After deposition, we immersed sample into hot acetone for lifting-off the gold film. In the third step, we performed the same procedures as the second one for gold ring gratings positioning.

Our Fano nanoantenna fabrication is very challenging as the 20 nm enclosed slit for lifting-off is critical. The slit is a very tiny area for the photoresist standing, therefore, the resist should be not only thin enough for standing alone within tiny area after development, but also should be thick enough for the 30 nm gold film lifting-off. Hence, we use PMMA 495A2 as a 100 nm thin photoresist for our Fano nanoantenna fabrication. However, 100 nm thin photoresist is difficult for lifting-off a 30 nm thick, 200-300 nm wide Au grating. Especially for the wide structure, it is better to use thicker resist as lift-off mask, therefore, we applied a layer of 200 nm PMMA 950A4 as grating lift-off mask. This is why we use three-step lithography rather than one step.

3.4 Grating design

The ring grating in this system is crucial as it reflects the antenna's coupling directivity, coupling efficiency, and modulation contrast at both 1550 nm and 1310 nm

wavelengths. Therefore, the design of the grating should be very careful.

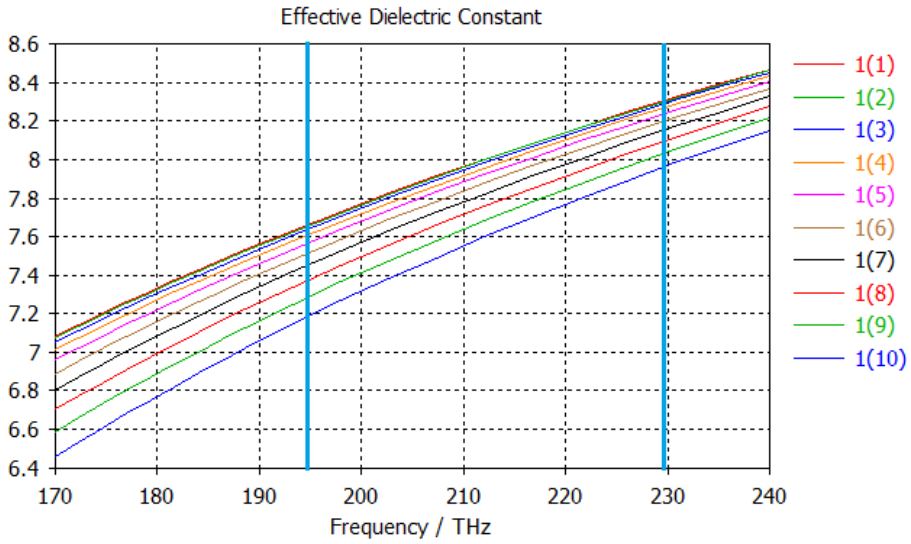

Figure 3.5: The effective dielectric constants dispersion curves simulated based on a 220 nm thick slab silicon waveguide for the first 10 different modes.

The interested wavelengths for our experiment are 1550 nm and 1310 nm, which corresponds to 194 THz and 229 THz. Fig. 3.5 indicates the effective dielectric constant of the slab waveguide of SOI based on CST Microwave studio simulation results. We are interested in the first 3 modes in this waveguide, and the average dielectric constant of those two wavelengths is about 8 for the first three modes, which is also the 1430 nm wavelength's dielectric constant. 1430 nm is the average wavelength of 1550 nm and 1310 nm. Therefore, the effective wavelength of 1430nm of slab waveguide is about 500nm, which is the grating period length. The next step is to decide the grating's width and thickness. The thickness normally we use for fabrication lift-off is 30 nm, and it is easier to keep this height. Therefore, the grating element width is the next number that we should find for both 1550 nm and 1310 nm light. We fabricated 6 different ring gratings with different widths (72nm, 136nm, 182nm, 237nm, 317nm, 375nm). With fixed laser power for both 1550 nm and 1310 nm, we excite those samples at one end of the grating and observe the intensity at the other end [Fig. 3.6 (a), (b)]. The results [Fig. 3.6 (c)] shows that the narrow grating unit, 1550 nm light [blue curve] coupling efficiency is considerably low compared to 1310 nm light [red curve] and the coupling efficiencies are similar for both 1550 nm and 1310 nm light with 220 nm width of each grating unit. We want to make the out coupling intensity comparable, because our modulation experiment requires two wavelengths light working at the same time. Finally, we decided use the 220 nm width grating [Fig. 3.6 (d)].

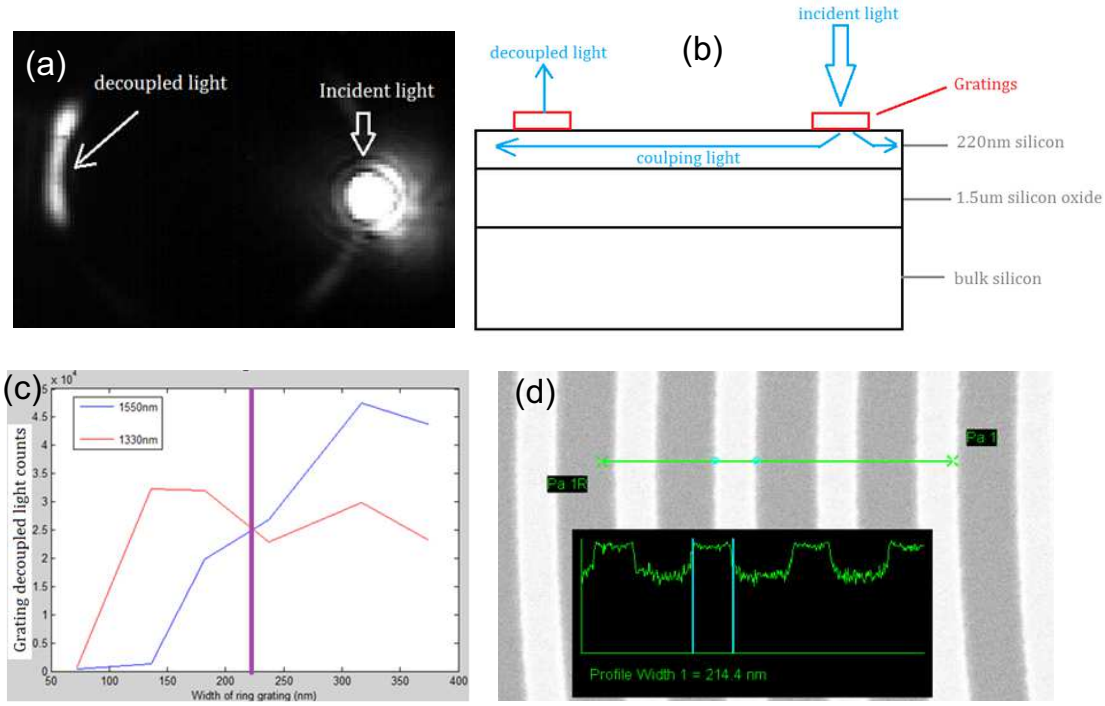

Figure 3.6: (a) The image captured by InGaAs camera the grating is illuminated by incident light and decoupled by the grating at the other end. (b) the schematic of slab waveguide grating coupling system. (c) gratings decoupled light counts with different grating widths and incident wavelengths (1550 nm and 1310 nm). (d) SEM image of the optimized grating for both 1550 nm and 1310 nm light

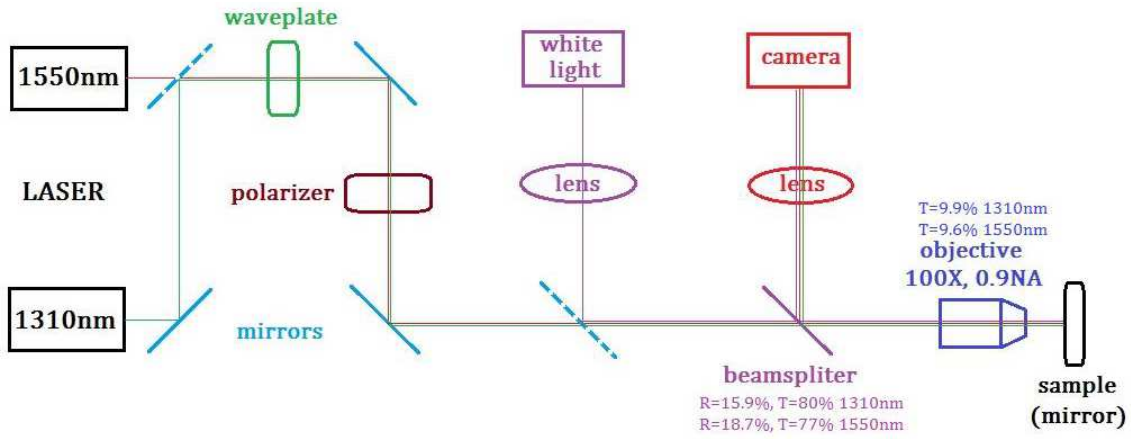

Figure 3.7: Optical measurement setup

3.5 Optical setup

Figure 3.7 is the optical measurement setup. The chopper is just in front of the lasers (1550 nm and 1310 nm). The two Pelico beam splitters are in front of 1550 nm laser and at the left side of the objective. A half waveplate is used for polarization controlling with a polarizer. The white light can illuminate large area of the sample to find our grating-antenna area easily. The objective can transmit 9.9 % of 1310nm light and 9.6 % of 1550nm light. The pelico beamsplitter can transmit 80% and reflect 15.9% of 1310 nm light, and transmit 77% and reflect 18.7% of 1550 nm light.

3.6 Summary

In conclusion, we have demonstrated an ultra-compact plasmonic spectral-band demultiplexer for telecommunication wavelengths integrated onto an optical waveguide that couples two wavelength-encoded optical signals in the O- and the C-band in opposite directions of a silicon waveguide. We make use of the concept of Fano resonances in order to realize a single-particle plasmonic nanoantenna that supports bi-directional scattering and can, therefore, be used as the funtional element for spectral-band demultiplexing. Furthermore, this nanoantenna can be deployed as either a functional element connecting two optical waveguides or as a functional link between off-chip signals and on-chip optical circuitry. For both cases the device functionality is achieved without the need of a functional electronic circuit where an optical signal has to be converted into an electrical system and back again. Hence, this spectral-band-division plasmonic nanoantenna provides an ultra-compact functional element for on-chip optical circuitry.

Chapter 4

Ultra-compact mode-selective light routing with on-chip nanoantennas

Optical nanoantennas provide a promising pathway towards a range of advanced light manipulation functionalities, such as directional scattering, polarization conversion, and fluorescence enhancement. While these functionalities of nanoantennas were so far mainly studied in free space or on homogeneous substrates, the integration of nanoantennas with optical waveguides offers important additional opportunities. Taking advantage of their versatility and unrivaled compactness, nanoantennas imprinted onto optical waveguides as functional elements may enable a dramatic enhancement of the design freedom and of the integration density for optical on-chip devices. Several examples of this concept have been demonstrated recently. However, the important question whether nanoantennas can fulfill complex functionalities for high-bit-rate transmission signal without degradation, which is the core purpose of many integrated optical applications, was not yet investigated.

In this chapter, we will introduce and investigate directional, polarization-, and mode-selective on-chip nanoantennas merged with a silicon rib waveguide. We demonstrate that these nanoantennas can separate optical signals with different polarizations of light vertically to different waveguide modes propagating into opposite directions. As the central result of this work, we then show the suitability of this concept for the control of optical signals with amplitude-shift keying (ASK) and non-return to zero (NRZ) 10 Gb/s modulation without significant BER impairments. Our results demonstrate that the waveguide-integrated nanoantennas have the potential to be used as ultra-compact polarization-demultiplexing on-chip devices for high-bit-rate telecommunication applications.

4.1 Introduction

Many of the intriguing opportunities offered by plasmonic nanoantennas severely suffer from the presence of intrinsic losses caused by metals at optical frequencies which ultimately stand in the way of bringing plasmonic nanoantennas from the concept stage to practical devices. Although, very recently, low-loss all-dielectric nanoantennas [147, 148] have been introduced to address this issue and highly effi-

cient nanoscale devices have been realized [119,120,149,150], there are many aspects where plasmonic nanoantennas still are superior to dielectric nanoantennas.

As a result, it is crucial to identify and explore the key areas where plasmonic nanoantennas can bring large benefits due to their unique functionalities and, in this way, to identify the niches where plasmonic nanoantennas can find their way to practical applications. One promising avenue to achieve this goal envisions plasmonic devices as functional elements on optical chips providing a fundamentally new link between electronic and photonic circuits [131, 132] like in plasmonic photodetectors [14,133–136] or modulators [137,138] and plasmonic amplifiers [151], for example. However, these works do not take advantage of the ample possibilities offered by nanostructured plasmonic particles, particularly nanoantennas, in terms of their designed functionalities, flexibility, and compactness which can add a whole new dimension to the functionalities of plasmonic on-chip devices. Using the additional design freedom may allow, for example, to realize ultra-compact functional interconnects which ultimately will increase the integration density and performance of photonic devices on optical chips. First attempts to use plasmonic nanoparticles as directional waveguide couplers have been explored only recently [6,48,142–144,146].

The crucial question for on-chip nanoantenna devices, however, is to what extend more complex functionalities of plasmonic nanoantennas can be realized on optical chips and if they are suitable for high-frequency signal processing.

To address these fundamental questions, we integrate hybrid plasmonic nanoantennas on dielectric waveguides and investigate their coupling properties at telecommunication wavelengths numerically and experimentally. Specifically, we aim to develop a basic set of on-chip nanoantenna geometries that allow us to selectively couple light of different polarizations into specific waveguide modes and, in addition to that, to control in which direction the incident radiation is coupled into the waveguide. We, then, develop a polarization- and mode-(de)multiplexing nanoantenna that can increase the channel capacity for integrated optical communication applications by combining two individual mode-selective directional nanoantennas in one antenna design. Our mode- or polarization demultiplexing nanoantenna can simultaneously couple light into different modes and direct the light coupled to each mode in opposite directions on a 400x400nm footprint (see Fig. 4.1). In this way, we realize a highly compact integrated device for polarization- and mode (de)multiplexing in contrast to conventional large-scale designs that are difficult to miniaturize and often rely on free space propagation.

Finally, in order to demonstrate the compatibility of our design for high-frequency applications, we perform high-frequency measurements with 10 GHz signal modulation in order to characterize the performance of the plasmonic device in terms of a key performance indicator in telecommunication applications – the bit-error rate. Our results show that designed plasmonic nanoantennas can indeed preserve their functionalities when transferred onto a dielectric waveguide platform and that they are very well suitable for high-frequency modulation on-chip signal processing at telecommunication wavelengths. This makes them a plasmonic key element for on-chip optical data processing that can also be used as a functional link between on-

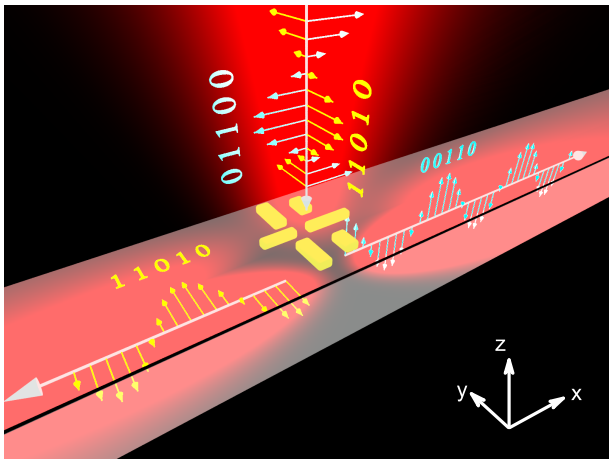

Figure 4.1: Scheme of a waveguide-integrated plasmonic nanoantenna for mode-selective polarization (de-)multiplexing. The device couples light of orthogonal polarizations into different directions and modes of the underlying silicon waveguide.

and off-chip optical signals.

4.2 Results and discussion

In a first step, we numerically design one polarization sensitive gold nanoantenna that is able to couple horizontally (x-) polarized incident light from free-space to the TM mode of an underlying silicon waveguide (Fig.4.2(a)) and a second one that couples vertically (y-) polarized incident light to the TE mode (Fig. 4.2(b)). In addition to this, the two antenna designs should support uni-directional waveguide coupling to selectively guide the light into a specific direction. The TM-antenna shown in Fig. 4.2(a) consists of two horizontally-aligned (along the x-axes) gold nanorods of different lengths ($l_{TM1} = 190nm$ and $l_{TM2} = 140nm$, $w_{TM} = 40nm$, $h_{TM} = 40nm$) that are displaced by a center-to-center distance of 195 nm with respect to each other in x-direction. Due the orientation of the two elements, the TM-antenna can only be excited by horizontally polarized light. Importantly, the radiation of both elements is only coupled to the TM mode of the waveguide (The mode selectivity value is 292 for TM antenna, which can be defined by the ratio of light coupled to the TM mode divided by the light coupled to the TE mode). Due to the different lengths of the two elements and their displacement the radiation coupled into the waveguide is constructively interfered on the right-hand side (+x-direction) and destructively interfered on the left-hand side (-x-direction) of the nanoantenna. Therefore, the TM antenna enables uni-directional waveguide coupling of horizontally polarized incident light to the right-hand side and into the TM mode of the waveguide. Following the same reasoning, the TE antenna (Fig. 4.2(b)) enables uni-directional waveguide coupling of vertically polarized incident light to the left-hand side and into the TE mode of the waveguide. In contrast to the TM antenna, however, the TE antenna

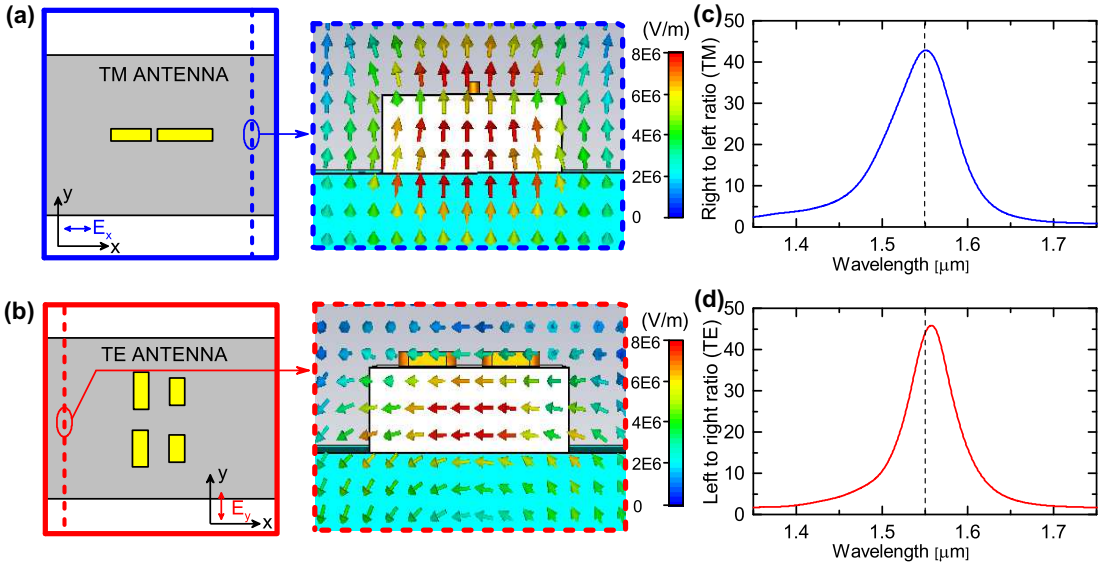

Figure 4.2: (a) Numerical design of the nanoantenna coupling x-polarized light into the TM mode of the waveguide to the right (TM-antenna). The electric-field distribution (color-coded arrows) in a cutting plane on the right-hand side of the nanoantenna (blue-dashed line) shows that the light is propagation in the TM-mode. (b) The corresponding design of the TE-antenna coupling light to the left-hand side into the TE mode. (c) and (d) shows the spectrally-resolved ratio of the light intensity coupled to the right (right-to-left ratio) by the TM-antenna and to the left (left-to-right ratio) by the TE-antenna, respectively.

is composed of two vertically aligned (y-direction) nanorods ($l_{TE1} = 180nm$ and $l_{TE2} = 144nm$, $w_{TE} = 60nm$, $h_{TE} = 40nm$) with that are displaced by a center-to-center distance of 130 nm with respect to each other in x-direction. The center-to-center distance between two pairs of the TE antenna is 260 nm. We use two pairs here for doubling the intensity of the coupled TE light, as the TE antenna couples less light than the TM one. The mode selectivity value for TE antenna is 53. The calculated ratio of light coupled to the right-hand side (right-to-left coupling ratio RL) and to the left-hand side (left-to-right coupling ratio LR) of the waveguide for both antennas is around 45.

Having established these basic nanoantenna elements that allows for mode-selective and directional waveguide coupling, we now use this toolbox to design an integrated plasmonic nanoantenna device that allows for on-chip polarization-(de)multiplexing. In order to achieve a clear separation of the polarization-encoded optical signals we take the above mentioned TM- and TE-antennas which support directional waveguide coupling in opposite waveguide directions and combine them in one nanoantenna design as shown in Fig. 4.3(a). The combined nanoantenna, then, couples horizontal polarization (linear-x polarization) to the right-hand side into the TM mode and vertically-polarized light (linear-y polarization) to the left-hand side into the TE mode (Fig. 4.3(b)) of the waveguide with a RL approx 20 and LR approx 55 at 1550

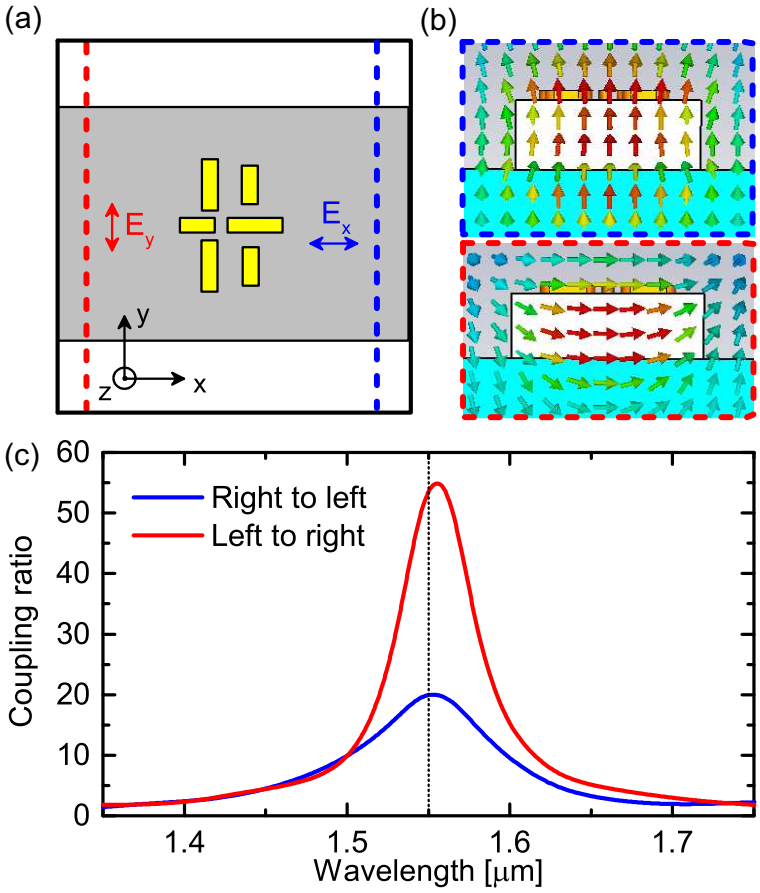

Figure 4.3: (a) Design of the combined TE-TM-nanoantenna coupling x-polarized light to the right (blue-dashed line) into the TM-mode and y-polarized light to the left (red-dashed line) into the TE mode of the waveguide. The corresponding electric-field plots are shown in (b). (c) Right-to-left (Left-to-right) ratio for coupling x-(y-)polarized incident light with a maximum at around 1550 nm wavelength.

nm wavelength (Fig. 4.3(c)), respectively. For all calculations the silicon waveguide has a height of 220 nm and a width of 600nm. The whole system is embedded in an effective medium with a refractive index of n=1.46.

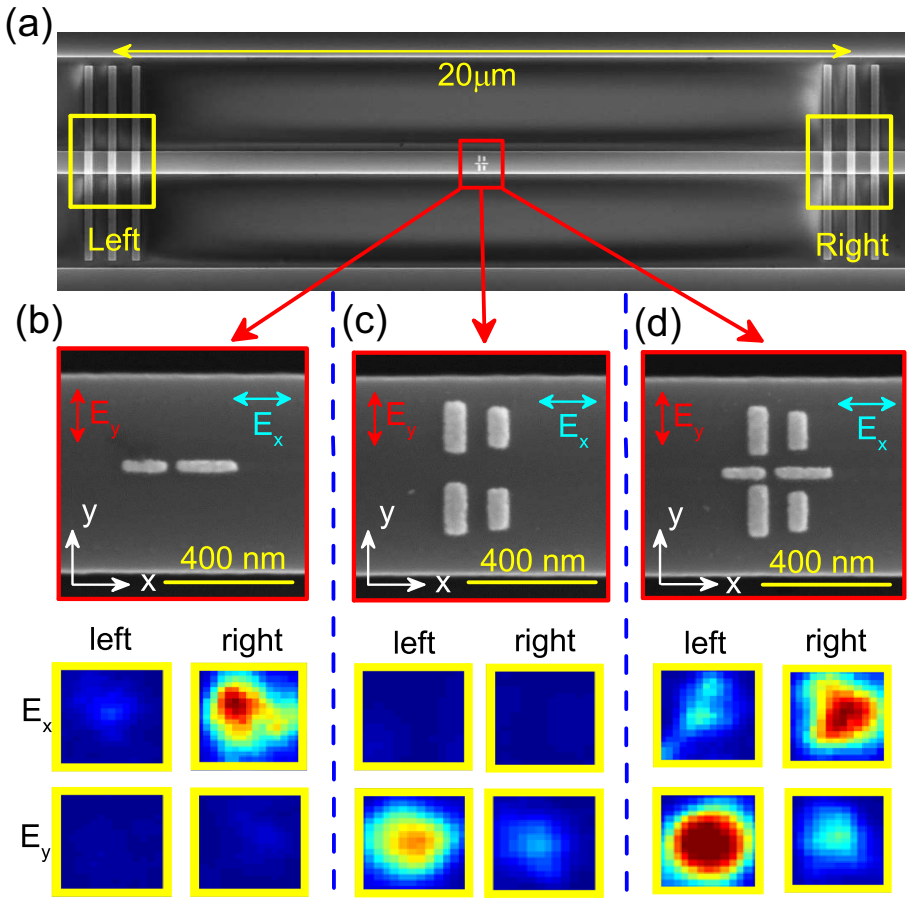

Figure 4.4: (a) Scanning-electron-microscope (SEM) images of a sample for measuring the coupling ratios of the three nanoantennas shown in (b) (TM-antenna), (c) (TE-antenna), and (d) (TE-TM-antenna). The nanoantennas are placed in the center (red square) between two gold gratings that are used as output ports (yellow squares) to detect the radiation coupled to the right-hand side and to the left-hand side of the waveguide. (b)-(d) show the SEM images (top row) of the fabricated antennas and the intensity plots at the left and right output ports detected on a CCD camera for x-polarization (second row) and y-polarization of the incident light of 1550 nm wavelength.

We note that in addition to the polarization-demultiplexing functionality of the combined nanoantenna for free-space excitation, this design can also be used as a waveguide-to-waveguide interconnect [146]. In this case, the device acts as a (TE-TM) mode-(de)multiplexer, i.e., separating information encoded in different waveguides modes. Hence, our nanoantenna can serve both as an ultra-compact bridge between free-space and on-chip photonic circuitry and as an integrated waveguide intercon-

nect. In the next step, we fabricate all three nanoantennas on a silicon waveguide and investigate their directional coupling properties. In order to demonstrate the corresponding functionalities of the three integrated nanoantennas we will, in the following, provide evidence for the key elements of our devices – the directional waveguide coupling, the polarization-dependent selective mode coupling, and the compatibility with high-frequency modulation. To do this, we fabricate two nominally identical sample batches for these experiments. In a first measurement, we detect the radiation that is coupled into the respective waveguide directions for the two orthogonal linear polarizations of the incident light. For this purpose small gold gratings are processed onto the waveguide in a distance of approximately 10 μm to the left and to the right of the nanoantennas (see Fig. 4.4(a)). By imaging the light that is coupled out by the gratings onto an InGaAs CCD camera we can measure the directional coupling ratio of the three antennas depending on the polarization of the incident light (see Fig. 4.4(b)-(d)). Our measurements shown in Fig. 4.4(b)((c)) confirm that the TM- (TE-) antenna couples horizontally- (vertically-) polarized light to the right- (left-) hand side of the waveguide for horizontal (vertical) polarization of the incident light with maximum RL- (LR-) ratio of 4.0 (3.7). Figure 4.4(d) shows the results for the combined nanoantenna and experimentally confirms the polarization-demultiplexing functionality of the combined, i.e., it shows that for horizontal polarization the incident light is coupled to the right and for vertical polarization the incident light is coupled to the left. The measured RL-ratio for horizontal polarization and LR-ratio for vertical polarization is around 3.3 and 3.7, respectively. When we combine TE and TM antennas as a whole, the influence of two types of antennas is trivial, and it does not affect much for the functionality of the system. In other words, when combining the antennas, the functionality is maintained and the interactions are small due to the polarization selectivity of the antennas.

In the second experiment, we provide evidence for the mode-selective coupling properties of the integrated nanoantennas. To this end, we use the second set of nominally identical samples but without a grating on top of the waveguide. We image the waveguide facet on either side of the cleaved sample onto a CCD camera and use a polarizing beam splitter to discriminate between the TE and the TM mode of the waveguide. We, then, detect the emerging light intensity in both waveguide modes depending on the polarization of light incident on the nanoantenna in the middle of the waveguide. These results are shown in Fig. 4.5 For the TM- (TE-) antenna we detect the signal on the right (left) waveguide facet while for the combined antenna we measure on both sides. Or results in Fig. 4.5(a) ((b)) show that for the TE- (TM-) antenna, indeed, vertical (horizontal) polarization is coupled to the TE- (TM-) mode of the waveguide. The corresponding measurements for the TE- and the TM-antenna have been done at the waveguide end where the maximum output intensity is expected due to the directionality of the nanoantennas that is at the left and the right waveguide facet, respectively. For the combined nanoantenna, we measured the polarization-dependent light intensity for both modes and both directions. These results are plotted in Fig. 4.5(c) and Fig. 4.5(d) and clearly show that vertical polarization of light is coupled to the left into the TE-mode and horizontal polarization is

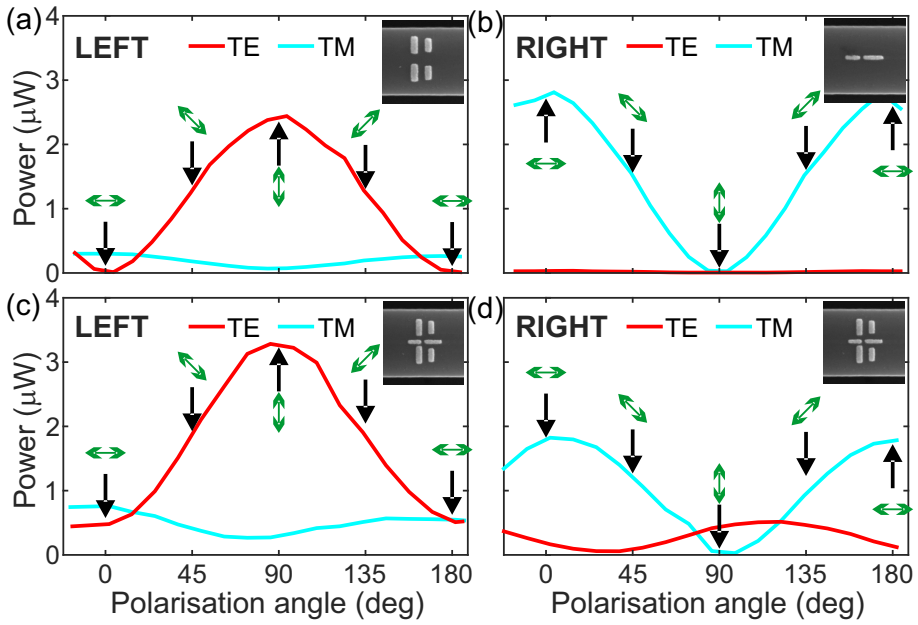

Figure 4.5: (a) Detected light intensity at the left end of the (cleaved) waveguide with the TE-antenna in the center for different polarization angles of the incident light (also indicated as green arrows for the main polarization directions). The light intensity in the TE-mode and the TM-mode of the waveguide is separated by a polarizing beam splitter in the detection part of the setup and plotted in red and blue, respectively. For vertical polarization at 90 degrees (corresponding to y-polarization) the intensity in the TE-mode is at its maximum. (b) Detected light intensity at the right end of the (cleaved) waveguide with the TM-antenna on top. Here we find an intensity maximum for horizontal polarization (0/180 degrees, x-polarization) in the TM-mode. (c) and (d) show the corresponding plots measured at both the left (c) and the right (d) waveguide end for the combined TE-TM-antenna confirming the coupling of y-polarized (x-polarized) light to TE-mode (TM-mode) on the left (right).

coupled to the right into the TM-mode, respectively.

Having demonstrated the mode-selective directional waveguide coupling and the polarization (de)multiplexing capabilities of our waveguide-integrated nanoantenna in experiment, we finally investigate the suitability of our integrated plasmonic system for high-frequency modulation as it is required for telecommunication applications. Although, in principle, the fundamental limit for the maximum modulation frequency is only limit by the plasmon decay time, which is on the order of tens of fs (corresponding to THz modulation frequencies), we want to explore the performance of our devices in terms of signal quality at 10GHz modulation frequency. The most important characteristic of a digital transmission link with this regard is the bit-error-rate (BER) of the system, i.e., the probability of the incorrect bit identification by a decision circuit. Usually BER of 10^{-12} to 10^{-15} are achieved for telecommunication links after forward-error correction [152]. For this purpose, we exemplarily couple a 10GHz-modulated signal to the TM-antenna, which exhibits the best polarization

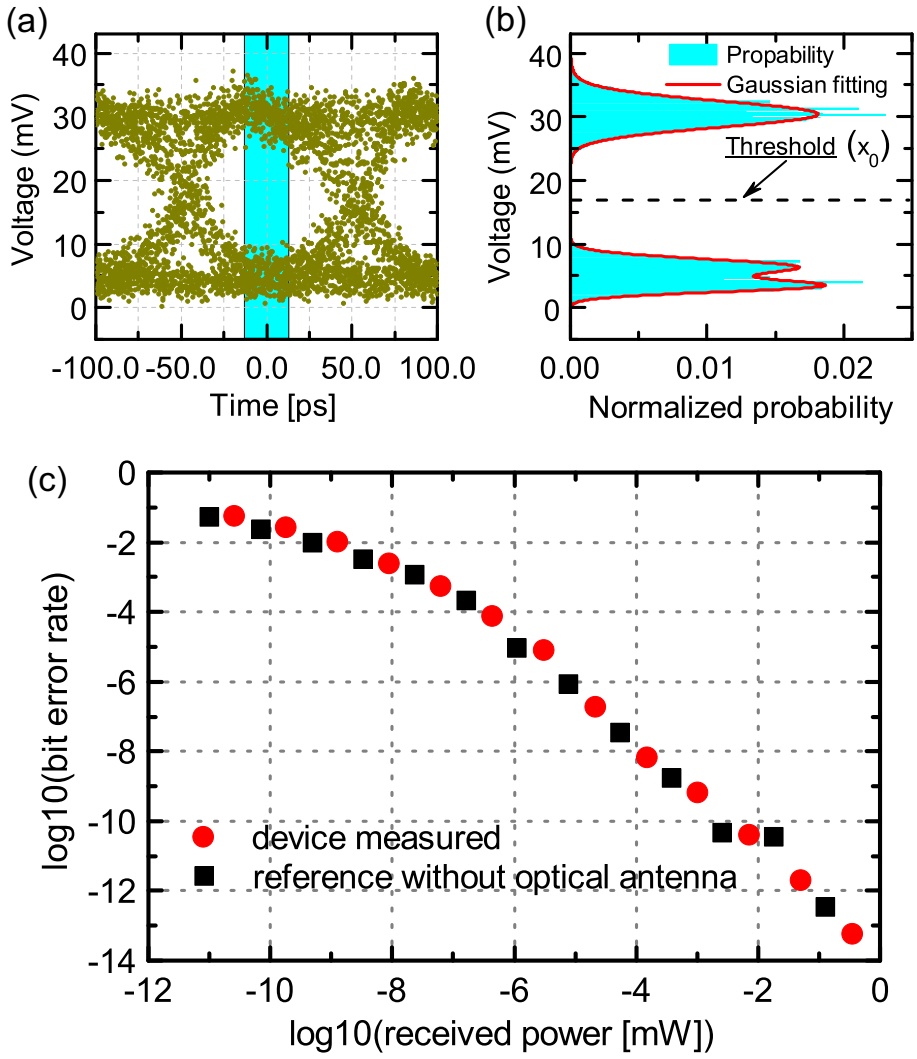

Figure 4.6: (a) Measured eye diagram for the TM-antenna at 10 GHz modulation frequency. The blue-shaded area is used for the statistical evaluation of the signal and the calculation of the bit-error-rate. (b) Probability density function for the detection of a logical one and zero and the Gaussian fitting used to determine the decision threshold x_0. (c) Calculated bit error rate of the sample with nanoantenna (red dots) and without antenna (black squares) for a series of received powers at the detector. Since the two data series lay on top of each other, the measured bit error rate is limited by the measurement setup and not the antenna. Hence the bit error rate of the antenna is below 10^{-13}.

selectivity, and analyze the signal emerging from the waveguide. We then measure the characteristic eye-diagram of the on-chip device (see Fig. 4.6(a)) and extract the probability density function for logical ones and zeros (Fig. 4.6(b)). Evaluation of the latter finally gives us the decision threshold x_0 and the BER of the system under the current conditions [153]. In order to estimate the influence of the measurement setup

on our results, we compare the BER of the measurement setup with sample and without the sample for a series of power values received at the detector. These results are plotted in Fig. 4.6(c). From these results we can see that, on the one hand, we achieve a minimum BER of almost 10^{-13} for a received power of approximately 1mW but, on the other hand, we also observe that the BER of the system with nanoantenna closely follows the reference BER values of the measurement setup alone. Consequently, the measured BER of 10^{-13} is an upper limit due to our setup and the actual BER of the plasmonic device is far lower. Nevertheless, our measurements clearly show that our device is very well competitive with current telecommunication links in terms of signal quality.

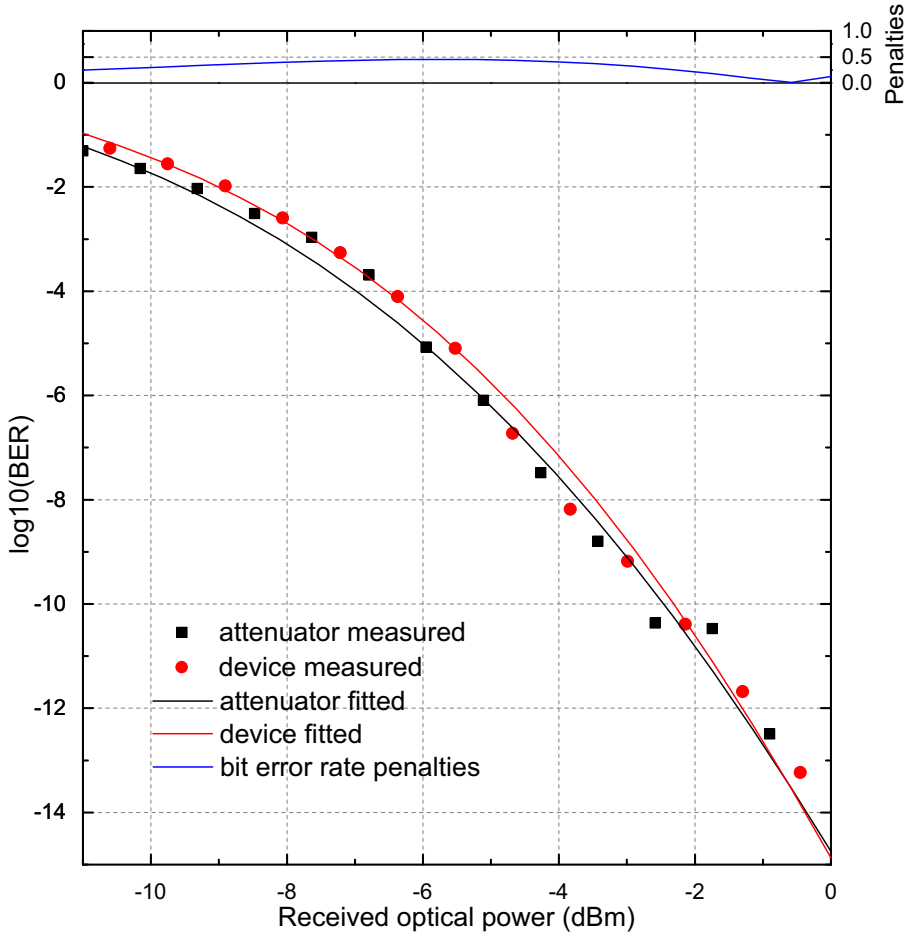

Figure 4.7: Red and black curves are the fittings from bit error rates of our device and optical attenuator (according to Fig. 4.6(c)). The blue curve is the bit error rate penalties.

4.3 Bit error rate data processing

The bit error rate (BER) is evaluated from eye diagrams, captured by a sampling oscilloscope. The device acquires a considerable amount of waveforms and uses them to calculate a histogram of a signal voltage. This histogram represents the statistics of data hits in the specified window, anchored to the center of the eye (see Fig. 4.6(a)). For the sufficiently large number of hits in the histogram window (100000 hits), the normalized histogram approximates the probability distribution function (PDF) of the received electrical signal – logic ones and zeros.

Eye diagrams are captured by the HP83480 sampling oscilloscope (digital communications analyzer). The device acquires considerable amount of waveforms and uses the waveforms to calculate a vertical histogram. This histogram represents the statistics of data hits in the specified histogram window (see Fig. 4.6(a)). If the total amount of data points is large enough (in our case it was typically about 50000 hits in the histogram window), then the normalized histogram represents the PDF of the transmitted signal, which allows us to estimate the BER value.

The histogram collected by the device must be normalized before one can extract any statistics from it. If the histogram is represented as N(x), where N is the number of hits in small interval Δx and x is the instantaneous voltage, then the normalized histogram n(x) is found as:

$$n(x) = \frac{N(x)}{\Delta x \sum N(x)} \tag{4.1}$$

This results in a unit area under the histogram given by $\Delta x \sum N(x) = 1$ formula. After the histogram is normalised we can find an average value $\langle x \rangle$ of the voltage, which is used as a preliminary decision threshold $\tilde{x}_0$

$$\tilde{x}_0 = \Delta x \sum x \cdot n(x) \tag{4.2}$$

We split the histogram into upper $n_{\uparrow}(x)$ and lower $n_{\downarrow}(x)$ parts using the $\tilde{x}_0$ value. It is very important to note, that this approach is valid only for the equiprobable signal. In case when the probabilities of logical ones and zeros are not equal, more complicated method should be used, e. g. fitting of whole histogram with a sum of two Gaussians and search for a local minimum between peaks.

The PDFs of one and zero in our system are close to Gaussian, but under certain conditions a pair of close peaks is observed in each semi-histogram.Therefore, we perform fitting of the semi-histogram with a sum of two Gaussians.

The selection of an appropriate starting estimate is crucial for the good fitting. For this reason we specify fitting functions $f_{\uparrow}(x)$ and $f_{\downarrow}(x)$ based on the statistics extracted from semi-histograms. The fitting function for logical one is:

$$f_{\uparrow}(x) = \frac{1}{\sigma_{\uparrow}\sqrt{2\pi}}(exp[-\frac{(x-\mu_{\uparrow}+\sigma_{\uparrow})^2}{\sigma_{\uparrow}^2}] + exp[-\frac{(x-\mu_{\uparrow}-\sigma_{\uparrow})^2}{\sigma_{\uparrow}^2}]) \tag{4.3}$$

where $\mu_{\uparrow}$ is the mean value and $\sigma_{\uparrow}$ is the data variance of the upper semi-histogram, which is supposed to be close to the normal distribution function.

$$\mu_{\uparrow} = \Delta x \sum x \cdot n_{\uparrow}(x) \tag{4.4}$$

$$\sigma_{\uparrow} = \sqrt{\frac{\sum n_{\uparrow}(x) \cdot (x-\mu_{\uparrow})^2}{\sum n_{\uparrow}(x)}} \tag{4.5}$$

We can also derive $f_{\downarrow}(x)$ function. The fitting functions $f_{\uparrow}(x)$ and $f_{\downarrow}(x)$ intersect with each other at the decision threshold value x_0. Hence, x_0 can be found according to the equation:

$$f_{\uparrow}(x_0) - f_{\downarrow}(x_0) = 0. \tag{4.6}$$

BER value is defined by a numerical integration of the overlapped regions according to the formula:

$$BER = \int_{-\infty}^{x_0} f_{\uparrow}(x)dx + \int_{x_0}^{\infty} f_{\downarrow}(x)dx. \tag{4.7}$$

4.4 Bit error rate penalties

Bit error rate penalty is the value that indicates the deviation of the BER of the device from the optical attenuator. The smaller the bit error rate penalty is, the better performance of the device.

To extract the BER penalties, we should obtain the BER both for the device under test (DUT) and the optical attenuator (VOA) with different values of received optical power [see Fig. 4.7]. Q-factor of the signal is retrieved from BER, according to the Ref. 153,154, which is the inverse function of BER.

$$BER = f(Q) = \frac{e^{-(Q^2/2)}}{\sqrt{2\pi}Q}. \tag{4.8}$$

We can fit the Q-factor function according to equation 4.9

$$Q_{fit}(x) = \frac{c_1 x}{\sqrt{c_2 x^n + c_3} + c_4}, n = 2. \tag{4.9}$$

After fitting the BER(Q_{fit}) both for the device under test and the optical attenuator, we can derive the BER penalties which is defined:

$$PEN = |logBER(Q_{fit}^{DUT}) - logBER(Q_{fit}^{VOA})|. \tag{4.10}$$

4.5 Numerical Calculations:

For the numerical calculations we use the finite element frequency domain solver of the software package CST Microwave Studio. We firstly calculate and optimize the properties of a single-mode waveguide made from silicon, resulting in a waveguide width of 600 nm and 220 nm of height. The refractive index of silicon is assumed to be 3.5 at 1550 nm wavelength. The waveguide is placed on a glass substrate with a refractive index of 1.45 and embedded in a PMMA cladding layer with a refractive index of 1.46. This configuration then results in an effective index for the TE and the TM mode of 2.98 and 1.99, respectively. In the second step, we use two orthogonal linear polarizations of light to excite the antennas, which are placed on top of the silicon waveguides, and optimize the nanoantennas dimensions in order to achieve optimum directional coupling ratios, modes selectivity values, and coupling efficiencies, respectively. Finally, we design the gold gratings that enable the detection of the coupled light for the front-to-back ratio and the directional coupling measurements. For this purpose, we use the averaged effective wavelength at 1550 nm of the TE and the TM mode as the grating period which is about 650 nm. The width of each stripe is 200 nm, and the thickness is 40 nm.

4.6 Sample fabrication:

To fabricate nanoantenna-waveguide samples, we performed three-step electron-beam lithography (EBL) on silicon on insulator (SOI) wafer (220 nm top silicon thickness, 2 μm buried oxide thickness). In the first step, we fabricated single mode silicon waveguides. Firstly, we spin coated ZEP520A resist with 6000 rpm for 2 min, before 3 min and 180 C hotplate post baking. Then we performed fixed beam moving stage (FBMS) mode with EBL . After electron-beam exposure (with 30 kV voltage, 20 μm aperture, 120 μC/sqcm dose), development was performed using cold ZEP developer with a development time of 80 s, followed by a rinse in isopropanol for 30 seconds. After the first lithography, we applied inductively coupled plasma (ICP) etching process (15 W RF Power, 400 W ICP power, 15 mTorr chamber pressure) using 50 sccm of CHF_3 and 1.8 sccm of SF_6 as etching gases. Remaining resist was removed by using oxygen plasma. In the second step, we fabricated alignment markers around

each of the waveguides. In a first step, we spin coated PMMA950 resist with 4000 rpm for 1.5 min, before 3 min 180 C hotplate post baking. Then we performed EBL for markers. After electron-beam exposure (with 30 kv voltage 7.5 μm aperture, 600 μC/sqcm dose), development was performed using cold 1:3 MIBK to IPA with a development time of 35 s, followed by a rinse in isopropanol for 30 seconds. After the second lithography, we deposited 30 nm Au film by using E-Beam evaporator. After deposition, we immersed sample into hot acetone for lifting-off the gold film. In the third step, we performed the same procedures as the second one for gold nanoantenna positioning. Lastly, we spin coated a layer of PMMA 950A as a cladding layer for the antenna-waveguide system.

4.6.1 Cold development:

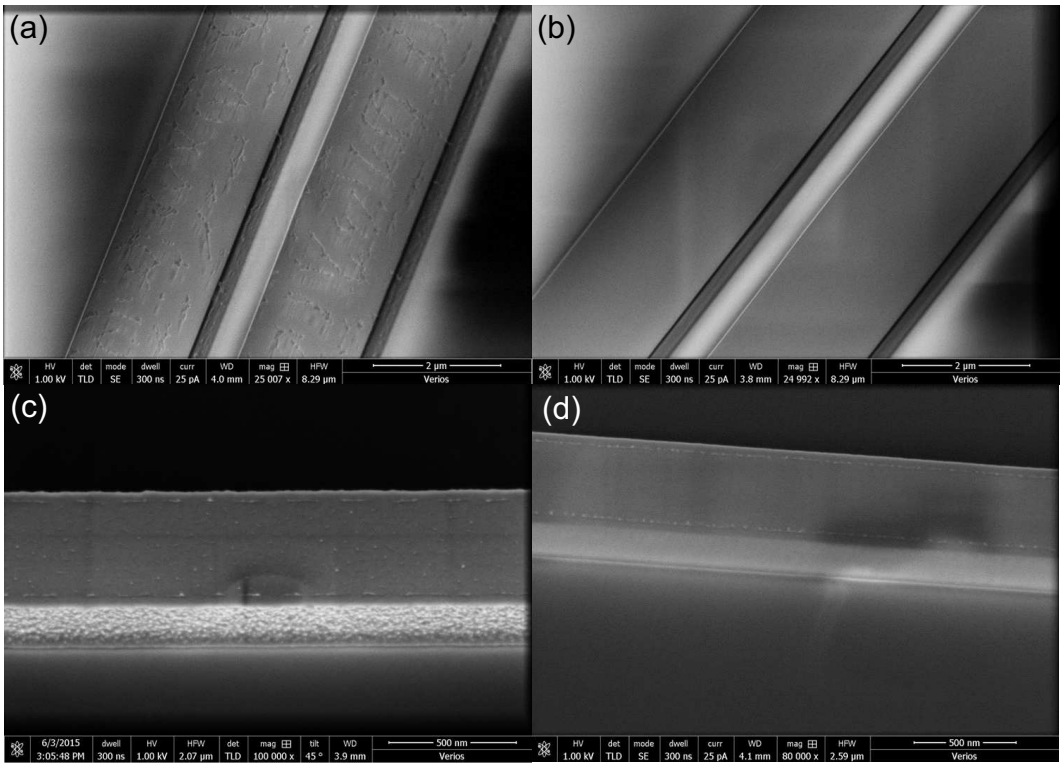

Figure 4.8: SEM images of ZEP520A photoresist mask on top of SOI substrate (a) without cold development and (b) with cold development; SEM images after ICP etching (c) without cold development and (d) with cold development.

To fabricate a low loss waveguide is very crucial to this project as loss gives rise to noise for the device. Typically, after the lithography step, the development of the photoresist is performed at room temperature (roughly 21 degree Celsius), and this is good enough in most cases. However, if people demand high resolution nanostructures, the lithography and development processes could be improved, and the cold development can be applied to the process. Figure 4.8 indicates the significant

improvement of the waveguide sidewall roughness due to the cold development process. Figure 4.8(a) is room temperature developed ZEP520A photoresist mask on SOI wafer compared with (b) low temperature development photoresist mask, and (c) and (d) after ICP etching, respectively. It is quite obvious to notice the phenomenal improvement quality of the mask after low temperature development. In this case, we developed our electron-beam exposed sample with approximately zero degree Celsius temperature ZEP developer.

4.7 High-frequency measurement setup:

In the optical modulation tests, a typical prototype of a fibre optics telecommunication line as described in Ref 153 is used [Fig. 4.9 and Fig. 4.10]. The optical signal is generated from the transmitter part, and the signal is guided by an optical setup to the sample. Finally, the output signal from the sample is collected and analysed in the receiver part. In transmitter part, we use an Anritsu MP1701A pulse pattern generator to generate pseudorandom bit sequence (PRBS) electrical signal which drives a JDS Uniphase Mach-Zehnder modulator to get an optical PRBS. The resulting modulated optical signals are amplified by a MANLIGHT EDFA to a power of 100 mW. Before exciting the plasmonic nanoantennas on waveguides, we introduce a linear polarizer and a half-wave plate to adjust the polarization state of light. In the receiver part, we use a lensed fiber to collect light emerging at the end of the silicon waveguide. The laser light from the lensed fibre passes another EDFA to amplify the optical signal from the device output. To control the received power, the amplified signal is then again attenuated by a variable optical attenuator. The optical signals are converted into electronic signals with an HP 11982A Lightwave converter. Finally, the electronic signal is detected and analyzed by an HP 83480A digital communications analyzer.

4.8 Summary

In conclusion, we have designed and characterized plasmonic nanoantennas integrated on silicon waveguides that allow for polarization-dependent, mode-selective, and directional waveguide coupling at 1550 nm wavelength. We experimentally confirm these properties and, furthermore, demonstrate via analyzing an optical signal with 10 GHz modulation frequency that the waveguide-integrated nanoantennas are very well suitable for on-chip telecommunication applications due to their low bit-error-rate penalty Using these ultra-compact hybridized antennas, we finally realize an on-chip polarization-(de)multiplexing device that can be deployed as either a functional link between free-space signals and on-chip optical circuitry or as a functional element connecting two optical waveguides. In the latter case the integrated nanoantenna can serve as a mode-(de)multiplexer. Hence, our polarization- and mode-(de)multiplexing plasmonic nanoantennas provide a set of ultra-compact integrated functional elements for on-chip optical circuitry. Such a device could e.g.

be used for future applications in integrated quantum optics, where polarization is an important degree of freedom used to create entanglement [155].

∗We used the telecommunication measurement setup in Applied Physics Institute, Jena with Dr. Frank Setzpfandt. Fabrication of the silicon waveguide was partially collaborated with Dr. Xin Gai and Prof. Duk-Yong Choi from Laser Physics Center, ANU.

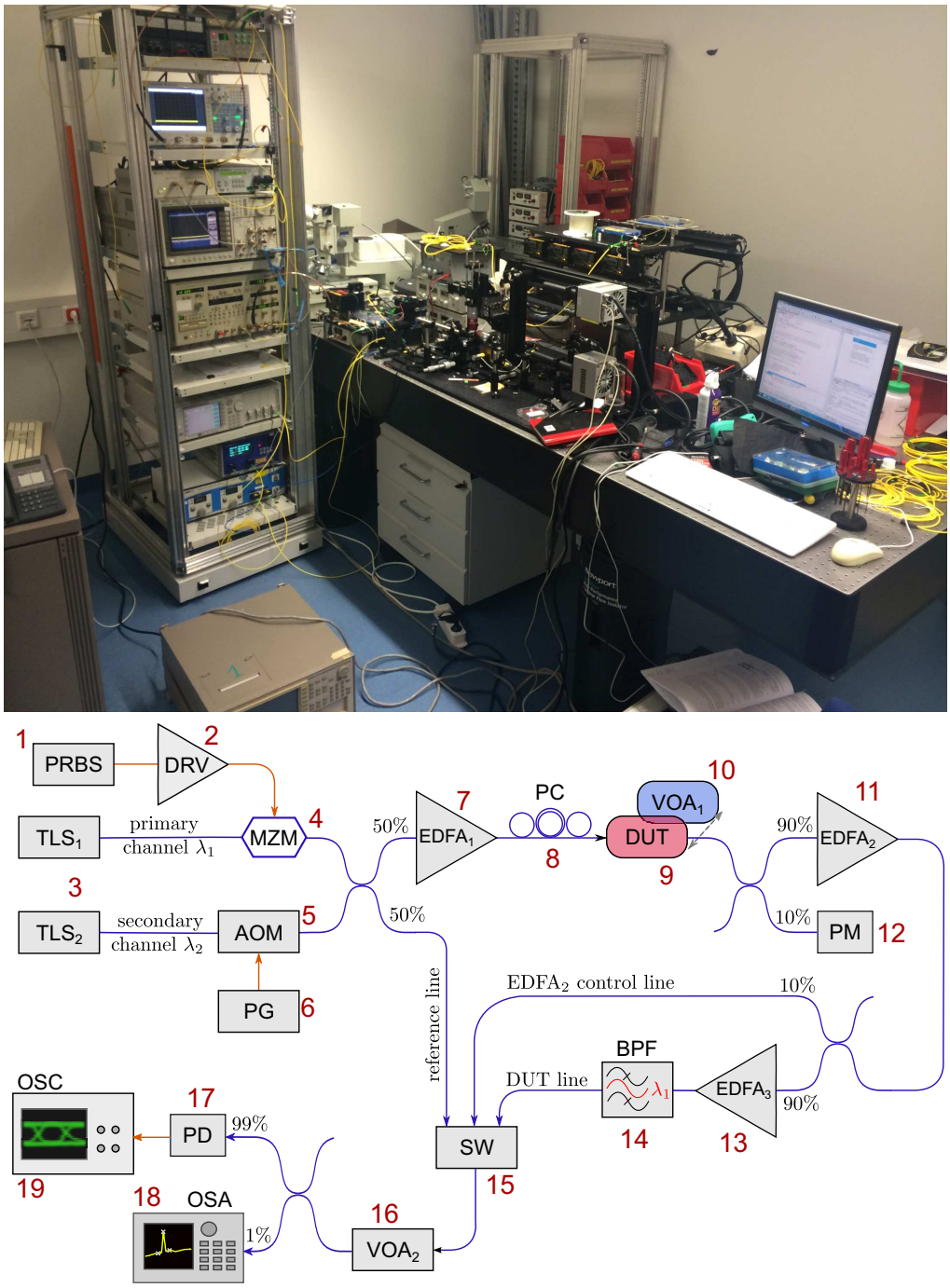

Figure 4.9: top: an image of 10GHz experiment set-up; bottom: (adapted from Ref. 153) Scheme of the experimental setup for the BER measurements: 1 - pseudorandom bit sequence generator (PRBS); 2 - electrical driver (DRV); 3 - tunable laser source ($TLS_{1;2}$); 4 - Mach-Zehnder modulator (MZM); 5 - Acousto-optical modulator (AOM); 6 - pattern generator (PG); 7, 11, 13 - erbium-doped fiber amplifiers ($EDFA_{1;2;3}$); 8 - polarization controller (PC); 9 - device under test (DUT); 10, 16 - motorized variable optical attenuators (VOA); 12-power meter (VOA); 14-tunable band-pass filter (BPF); 15 — fiber optic switch (SW); 17 - fast photodetector (PD); 18 - optical spectrum analyzer (OSA); 19 - sampling oscilloscope (OSC).

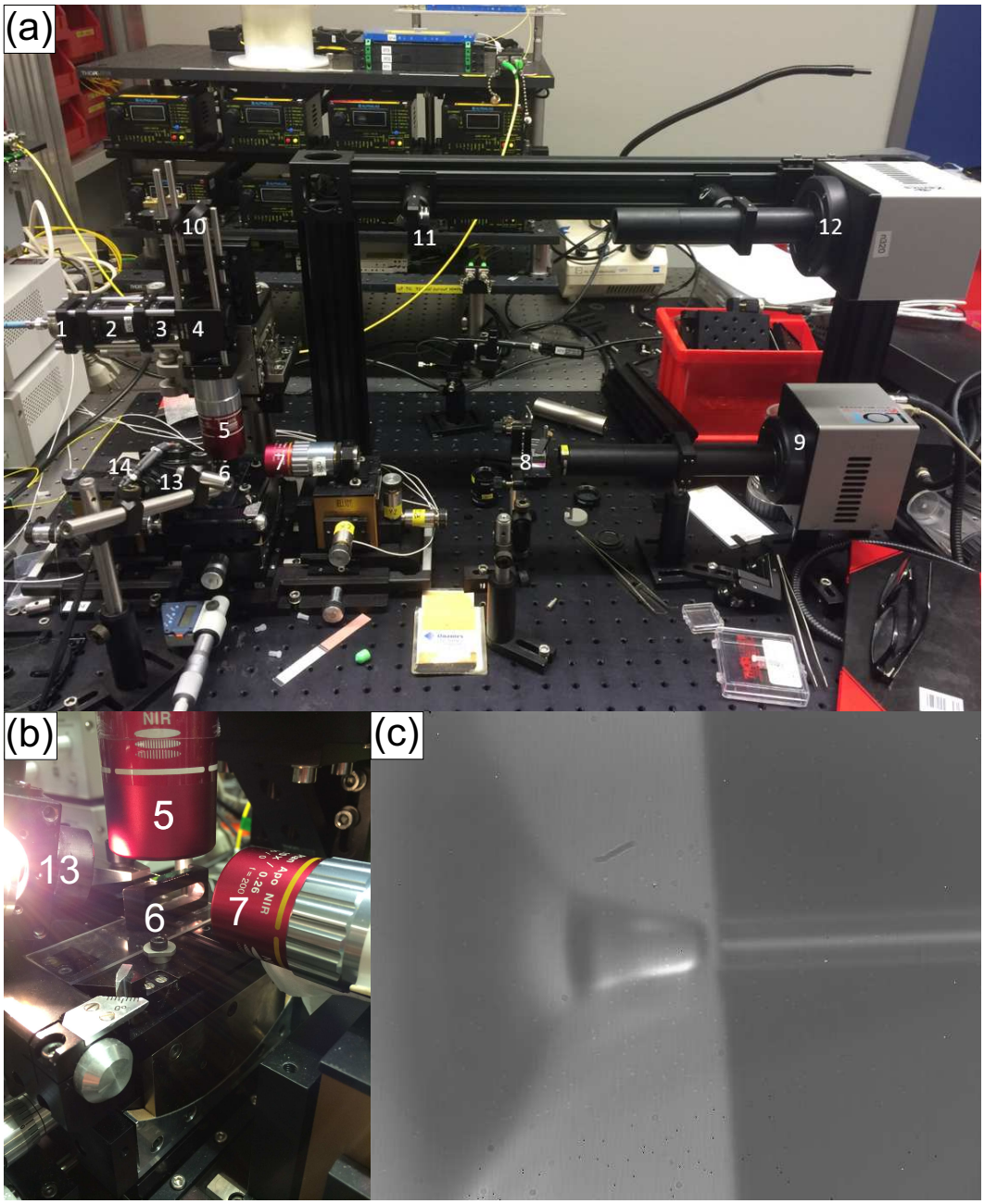

Figure 4.10: (a) 1-polarization maintaining fiber and collimator, 2-polarizer, 3-1550 nm zero order half wave plate, 4-beam splitter, 5-100X objective, 6-antenna-waveguide device, 7-10X objective, 8-polarization beam splitter, 9, 12- infra-red camera, 10-mirror, 11-30cm convex lens, 13-Tungsten light, 14-lensed fiber; (b) Zoomed in image of sample area; (c) image of lensed fiber and silicon waveguide coupling.

Chapter 5

Multipolar coupling in hybrid metal-dielectric nanoantenna arrays

All-dielectric and plasmonic nanostructures have complementary advantages regarding their capabilities for controlling light fields at the nanoscale. While all-dielectric nanostructures can provide near-unity efficiency, plasmonic nanostructures are more compact and offer strong near-field enhancement. Combination of photonic nanostructures of both types offers a promising route towards compact optical elements that unify low absorption losses with small footprints. In this chapter, we will discuss functional hybrid nanoantenna arrays consisting of metal-dielectric nanoantennas that direct light from an incident plane wave or from localized light sources into a preferential direction. The directionality is obtained by carefully balancing the multipolar contributions to the scattering response from the constituents of the nanoantenna array. The hybrid nanoantennas are composed of a plasmonic gold nanorod acting as a feed element and a silicon nanodisk acting as a director element. In order to experimentally realize this design, we have developed a two-step electron-beam lithography process in combination with a precision alignment step. The optical response of the fabricated sample is measured and reveals distinct signatures of coupling between the plasmonic and the dielectric nanoantenna elements that ultimately leads to unidirectional radiation of light.

5.1 Introduction

Nanoantennas can provide an efficient link between localized optical near-fields and propagating optical far-fields, allowing for strong enhancement of light-matter interaction processes such as spontaneous emission enhancement, nonlinear optical processes, or perfect absorption in a small, defined volume. To this end, the nanoantenna array can harness the abilities of nanoparticles to concentrate light into small volumes and to establish highly directional scattering patterns, thereby emitting or receiving light into or from a narrow solid angle efficiently. As such, the meta-atoms borrow their functionalities from optical nanoantennas including plasmonic and dielectric antennas. While plasmonic nanoantennas [11,38,45,156] have proven to provide good directionality and excellent coupling properties due to the strong field

enhancement, they suffer from their intrinsic absorption [157]. All-dielectric nanoantennas [148,149,158–160], on the other hand, exhibit high radiation efficiencies but the lower field confinement also reduces coupling efficiencies. Hybrid metal-dielectric nanoantennas composed of plasmonic feed elements and dielectric director elements allow for combining the advantages of both plasmonic and all-dielectric nanoantennas. Hence, they may offer large Purcell enhancements and highly directional radiation patterns while preserving high radiation efficiencies at the same time. Various recent theoretical and numerical studies have analyzed hybrid nanoantenna architectures, mainly in the context of emission manipulation [161–164]. Typically, a resonant plasmonic dipole or feedgap antenna is used as a nanoantenna feed element, providing a strong near-field enhancement and thus a high enhancement of the radiative decay rate. Then, in order to shape the radiation pattern of the hybrid nanoantenna without introducing notable additional losses, a dielectric nanoantenna is employed as a director element. This allows us to capitalize on the strong field enhancement provided by the plasmonic feed element and, at the same time, to efficiently direct the emission in a specific direction. As a result, this sequential approach where nearfield coupling between metallic and dielectric particles results in designed far-field radiation patterns can provide record values for directional emission enhancement from a dipole source which cannot not be achieved with plasmonic or all-dielectric nanoantennas alone under the same conditions [164]. In addition to their prospective use for tailoring emission from nanoscopic sources, metal-dielectric nanoantennas can also offer very interesting opportunities for bidirectional scattering [6,146]. For example, coupling of a plasmonic antenna element (with a low quality factor) to a dielectric antenna element (with a high quality factor) allows to combine resonances of very different quality factors and results in Fano resonances which, in turn, can be used to achieve extended control over the directional radiation characteristics [6,146].

Altogether, hybrid nanoantenna geometries are interesting candidates for a range of photonic applications, including directional nanoscale light sources [161–164], biosensing [165], as well as optical switching and routing [166]. By employing hybrid nanoantennas as meta-atoms for functional nanoantenna arrays we, thereby, define a new type of *hybrid nanoantenna arrays* with radiation properties defined by the properties of the underlying constituents. Since we use metal-dielectric nanoantennas as meta-atoms, these hybrid nanoantenna arrays can provide new functionalities to realize directional and emission-shaping nanoantenna arrays when, e.g., quantum emitters are coupled to the plasmonic feed elements [39,156]. However, due to their structural complexity, the fabrication of resonantly coupled metal-dielectric nanoantenna array is considered as a challenge and not many works has been demonstrated so far.

5.2 Metal-dielectric multi-layer structure fabrications

Here, we address this challenge and fabricate stacked metal-dielectric nanoantennas consisting of subwavelength arrays of gold nanorods coupled to silicon nanodisks

[Fig. 5.1 (a)] and investigate the optical response and directional radiation properties at near-infrared wavelengths.

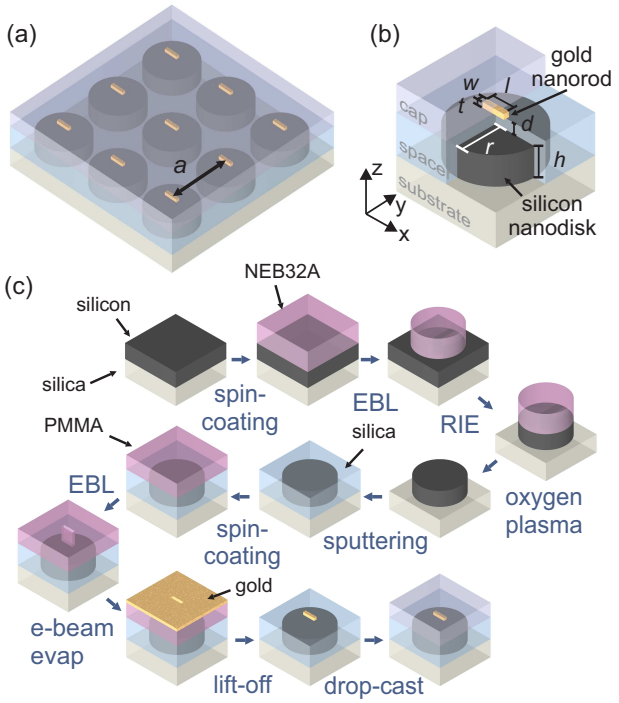

Figure 5.1: (a) Sketch of the two-dimensional hybrid nanoantenna arrays and (b) the detailed geometry of a single metal-dielectric nanoantenna. (c) Steps performed for fabrication of the stacked hybrid nanoantenna arrays.

A sketch of the considered hybrid nanoantenna arrays and the meta-atom geometry is shown in Fig. 5.1 (a,b). A gold nanorod with its fundamental resonance tuned to the design wavelength of 1.1 μm for an electric field polarized along its long axis is used as a feed element. The gold nanorod is placed in a specific distance above a silicon nanodisk featuring strong quadrupolar resonances [167] around the same wavelength. This silicon nanodisk acts as a director element. The nanoantenna array is processed on a SiO_2 substrate with a refractive index of 1.45. The dimensions of the gold rod are l =180 nm, w =40 nm, and t =40 nm. The silicon nanodisk has a height of h =220 nm and a radius of r =235 nm and is covered by a 75 nm-thin layer of SiO_2 that acts a spacer layer between the two elements. The spacer layer is optimized to achieve maximum directivity in forward direction [$-z$-direction in Fig. 5.1 (b)]. The entire structure is embedded into an index-matching oil. In order to produce the nanoantenna array, we arranged the meta-atoms in a two-dimensional array with a lattice constant of a = 670 nm as shown in Fig. 5.1 (a).

To fabricate the hybrid meta-atoms, we have developed a two-step electron-beam-lithography (EBL) procedure, which is schematically illustrated in Fig. 5.1 (c). The first step of EBL defining the silicon-nanodisk director elements is performed on a silicon-on-insulator wafer (SOITEC) with a silicon-layer thickness of 220 nm using

the negative-tone e-beam resist NEB32A. The resulting resist pattern serves as a mask for reactive-ion etching (RIE) of the device layer. Any residual resist is removed by oxygen-plasma etching. In the second step, we concentrate on hybridizing these dielectric elements with the plasmonic gold nanorods in a defined fashion. To this end, we first sputter a thin layer (approx. 5 nm) of Indium-Tin-Oxide [not shown in Fig. 5.1 (c)] to restore the DC conductivity of the sample which has been lost during the etching procedure in the previous step. Next, cross-shaped gold alignment marks are lithographically defined at the corners of the nanodisk arrays and the sample is carefully mapped in a scanning electron microscope. Note that the latter two steps are not mandatory and have not been depicted in Fig. 5.1 (c) as alignment markers can also be directly incorporated into the first EBL step. Next, we deposit a 75 nm-thin layer of SiO_2 as a spacer defining the separation distance between the feed element (gold nanorod) and the director element (silicon nanodisk).

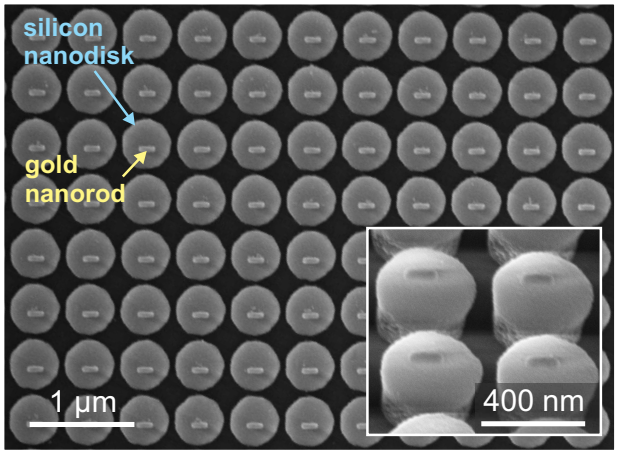

Figure 5.2: Scanning electron micrograph of the fabricated hybrid metal-dielectric nanoantenna array. The inset shows a magnified and oblique view of the same sample.

We then perform the second step of EBL defining the gold nanorod feed elements using the positive-tone electron-beam resist PMMA 950K A4 from Microchem. The predefined marks enable the precise alignment of the second exposure step with regard to the pre-defined silicon nanodisks. Following exposure and development, we deposit 40 nm of gold via electron-beam evaporation and we perform a lift-off procedure in hot acetone. As a last step, in order to ensure that the resulting structures are situated in an isotropic, low refractive-index environment during measurement, we drop-cast an index-matching oil (n=1.45) onto the sample. Alternatively, the application of a thick SiO_2 layer can be considered to provide a homogeneous dielectric environment. A scanning electron micrograph of the resulting nanoantennas before drop-casting the oil is displayed in Fig. 5.2. The inset shows a close-up of a few hybrid nanoantennas in the array.

5.3 Nanoantenna array characterization

In the following, the fabricated structures are optically characterized, the measured spectra are compared to numerical simulations and the directional radiation properties of the hybrid antenna design are studied. For optical characterization we perform linear-optical transmittance measurements using a home-built white-light spectroscopy setup which employs a tungsten-halogen lamp as a light source. By inserting a linear polarizer behind the light source we can choose the electric-field polarization of the incident light to be aligned parallel or perpendicular to the long axis of the gold nanorod, respectively. This allows us to selectively excite the nanorod resonance at approximately 1.1 μm wavelength only for the polarization parallel to the long axis of the gold nanorod. An aperture is introduced in an additional image plane behind the sample to select the light that is passing through the nanoantenna array only. All measurements are referenced to an unstructured sample area of equal size next to the nanoantenna array. The measurement results are displayed in Fig. 5.3 (a). A significant difference between the transmittance of the nanoantenna array for the two incident polarization directions is observed in the spectral region around the operation wavelength of the nanorod at 1.1-1.2 μm wavelength and in a second spectral region at 1.3-1.4 μm wavelength as well. Since the silicon material tends to be notably lossy below a wavelength of 1 μm, the experimental spectra become noisy when the wavelength approaches 1 μm.

In order to provide an explanation for the observed spectral behavior, we compare our experimental results with numerical finite-integral frequency-domain calculations using the commercial software package CST Microwave Studio. In these simulations the nominal geometry of the fabricated sample has been fully considered. For the optical properties of gold we use the data from Ref. [168] and for silicon we consider a refractive index of 3.5, respectively. Calculated transmittance spectra for the two linear polarizations are displayed in Fig. 5.3 (b), showing good qualitative agreement with the experimental spectra. In particular, we note that the difference in the transmittance for the two orthogonal polarizations is less pronounced in the experimental spectra as compared to the numerical ones. This is mainly due to sample imperfections, such as imperfections in the alignment of the plasmonic nanorod with respect to the center of the silicon nanodisk.

To shed light on the directional radiation properties of the hybrid nanoantennas, we furthermore calculate the radiation cross-section of the corresponding single metal-dielectric meta-atom [Fig. 5.4 (a)] and calculate the radiation pattern at the two resonance positions. We additionally calculate the front-to-back ratio [Fig. 5.4 (b)] defined here as the radiated power in the forward direction [$-z$-direction in Fig. 5.1 ,(b)] divided by the radiated power into the backward ($+z$-) direction. The obtained front-to-back ratio for the two relevant spectral regions is above 60 and 100, respectively. We note that the occurrence of the characteristic radiation properties shown in Fig. 5.4 (a,b) can, in principle, be qualitatively explained by a superposition of the electric and magnetic dipoles of the silicon nanodisk [148,149] and the electric dipole of the gold nanorod that is displaced by 185 nm in +z-direction from the overlap-

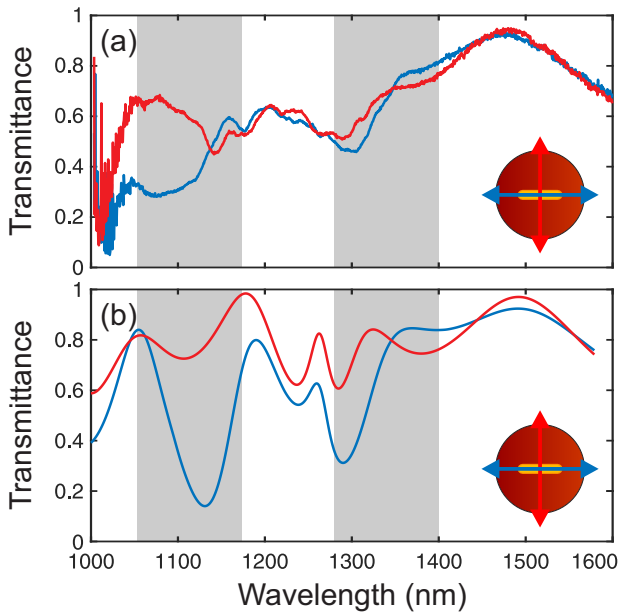

Figure 5.3: (a) Measured and (b) numerically calculated normal-incidence linear-optical transmittance spectra for incident light polarized parallel (blue) and perpendicular (red) to the long axis of the gold nanorod. The interplay of the plasmonic and the dielectric nanoantenna elements results in a significant difference between the transmittance for the two incident polarizations for the spectral region where the nanorod resonance is excited but also for the off-resonant case at 1.3-1.4 μm wavelength.

ping dipoles of the nanodisk. However, due to interactions in the system this picture doesn't reflect the quantitative radiation properties shown in Fig. 5.4 (a,b). To shed, nevertheless, light on the scattering properties of such a hybrid device, we perform a multipole decomposition of the local fields of a single metal-dielectric meta-atom to identify the multipole components that give rise to the characteristic radiation properties. In the multipole analysis we consider a situation in the simulation where the antenna is illuminated by a plane wave according to the experimental situation. We use again CST Microwave Studios to solve the full wave problem and to extract the scattered field. The scattered field is afterwards projected onto the different spherical harmonics, which represent eventually the fields of electric and magnetic dipoles and quadrupoles. This allows to extract the multipole moments induced in the antenna by the respective illumination. Fig. 5.4 (b) shows afterwards the contribution of each multipole moment to the scattering cross-section. This allows to understand the importance of each multipole moment and constitutes an excellent base to understand the ability of the hybrid antenna to preferentially scatter the light into the forward direction. More details on the multipole analysis can be found in Ref. [169]. Using this method, we extract the dominating multipole contributions with respect to the central coordinate of the silicon nanodisk from the local near-fields of the meta-atom and plot the dominating multipole contributions in Fig. 5.4 (c). From Fig. 5.4 (c) we

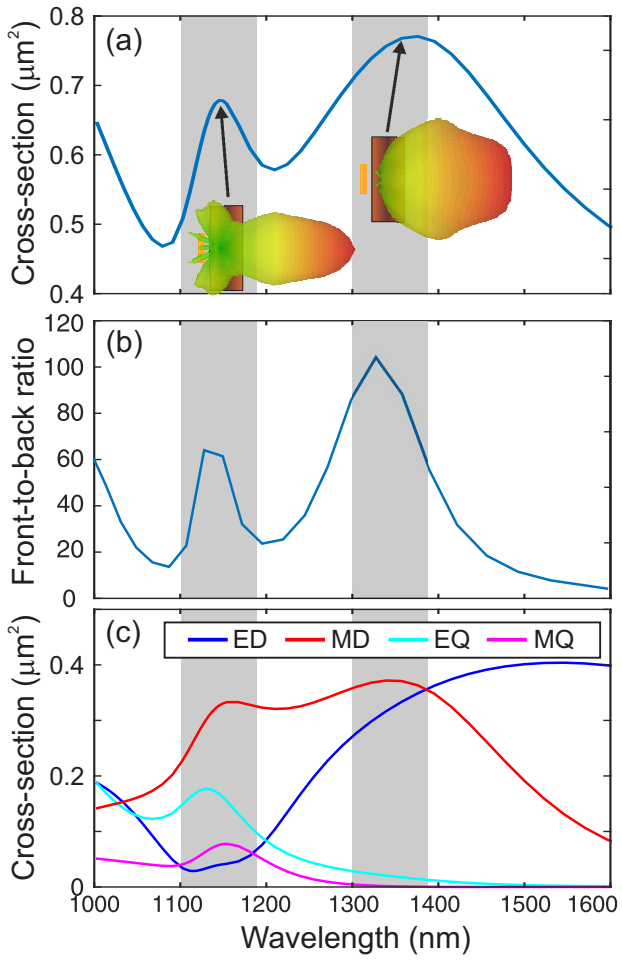

Figure 5.4: (a) Numerically calculated radiation cross-section for a single metal-dielectric nanoantenna and (b) the calculated front-to-back ratio of the light radiated by the hybrid nanoantenna for incident polarization along the long axis of the gold nanorod. (c) Multipole decomposition of the local fields composed of electric dipole (ED), magnetic dipole (MD), electric quadrupole (EQ), and magnetic quadrupole (MQ) contributions. The insets in (a) show the radiation patterns at the spectral positions marked by the arrows.

can identify that at wavelengths from 1.1-1.2 μm, i.e. when the plasmonic nanorod is in resonance, the directional radiation is caused by the superposition of a pronounced magnetic dipolar contribution with electric (and weaker magnetic) quadrupolar components of the combined system in accordance with previous theoretical findings where a directional radiation behaviour has been attributed to the superposition of electric and magnetic multipole moments in plasmonic nanoantennas [45]. We note that, even though the plasmonic nanorod has a scattering response that is purely electric dipolar, the scattered field from the nanorod in the hybrid design is expanded with respect to a central coordinate that is outside of the nanorod, i.e. it is in the center of the silicon nanodisk. Therefore, additional multipole moments than the electric

dipole moment are necessary to describe the scattered field of the gold nanorod. In the specific situation the displacement, however, is small and the scattered field is well described by those multipole moments depicted in Fig. 5.4 (c). Nevertheless, when exploring the ability to suppress the backscattering from those hybrid nanoantennas using e.g. generalized Kerker conditions, the characteristic radiation pattern shown in the inset of Fig. 5.4 (a) can be explained by the superposition of the corresponding multipole components [170]. As such, although the front-to back ratio is higher at the longer-wavelength resonance, the scattering pattern becomes more directive at the resonance of the plasmonic nanorod due to this excitation of higher-order multipoles in the nanodisk.

In contrast to this, the spectral region from 1.3-1.4 μm wavelength is dominated by a superposition of the electric and magnetic dipole components of the nanodisk director element that ultimately gives rise to unidirectional radiation with the corresponding characteristic radiation pattern shown in the inset of Fig. 5.4 (a). Remarkably, in this regime the hybrid meta-atom acts as a Huygens' element [149] and could, therefore, be also used as a fundamental building block for efficient wave-shaping devices.

5.3.1 Multipole expansion for the individual elements of the hybrid metal-dielectric nanoantenna

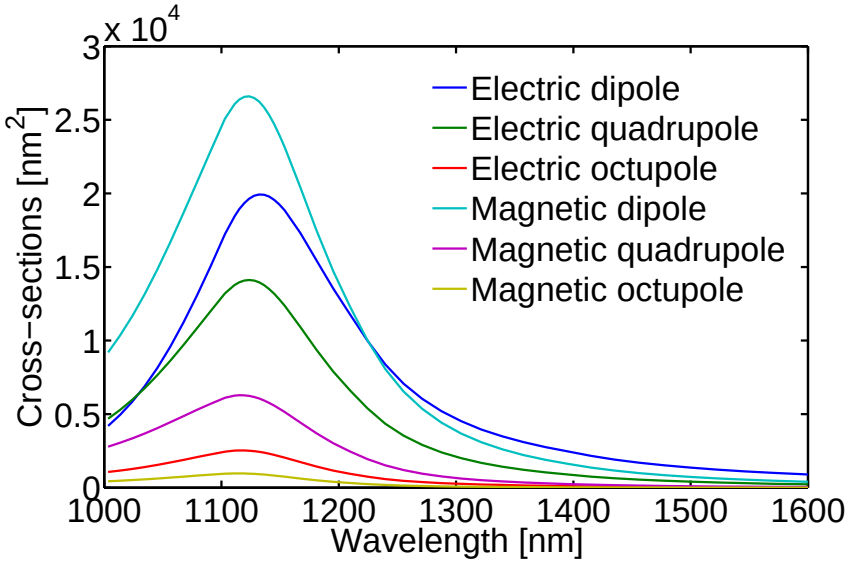

Figure 5.5: A single gold nanorod multipole expansion.

Figure 5.5 and Figure 5.6 are the multipole expansion for a single gold nanorod and a single silicon nanodisk, respectively. Both multipole decompositions are done at the center of the silicon nanodisk. We chose this origin so that all expansions can be compared, and this is why the gold nanorod does not appear as a perfect electric dipole. This indicates that the quadruopole mode of the disk gives the directionality

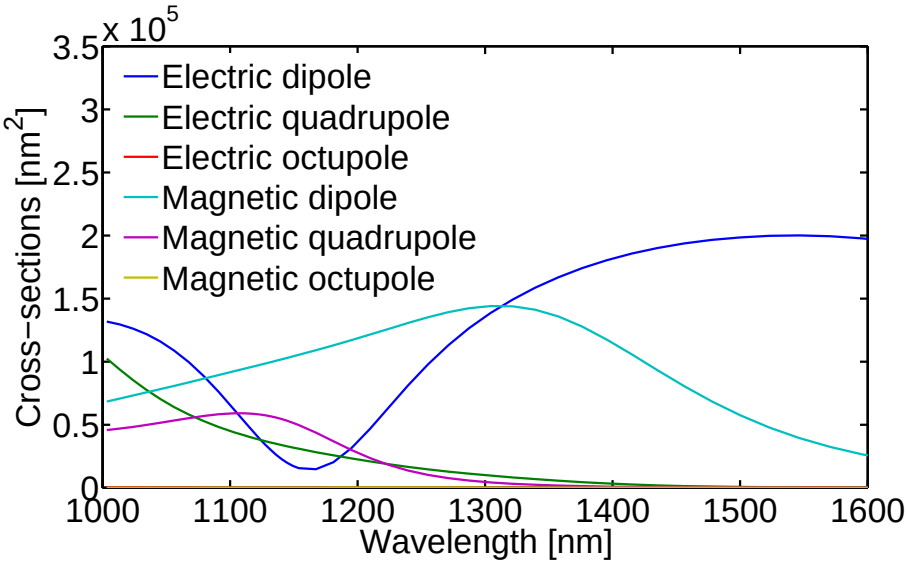

Figure 5.6: A single silicon nanodisk multipole expansion.

together with the nanorod.

The multipolar expansion shows that the hybrid structure contains both the electric dipole and the magnetic quadrupole, and since these modes are not orthogonal, they can couple to each other. Hence, in general, the two modes can be excited by the other one.

5.4 Summary

In conclusion, we have realized a hybrid metal-dielectric nanoantenna array composed of gold nanorods that are coupled to silicon nanodisks. To this end, we have implemented and successfully demonstrated a multi-layer fabrication approach to realize stacked metal-dielectric meta-atoms that combine the advantages of both plasmonic and dielectric elements. We have studied the optical properties of this nanoantenna array and investigated its directional radiation properties. We show that our design supports uni-directional radiation of light with a maximum front-to-back ratio of above 100 and analyzed the interplay of its multipolar electric and magnetic contributions that lead to the directed radiation behaviour of the single constituent elements. In particular, we have identified the operation band where the meta-atoms effectively behave as Huygens' elements that, in principle, allow for full 2π phase manipulation. Therefore, our hybrid nanoantenna array can be used in a range of photonic applications, including wave-front manipulation, directional nanoscale light sources, biosensing, or optical switching and routing.

*Silicon nano-disks were fabricated in Sandia National Lab by our collaborators.

Chapter 6

All-dielectric metasurface in biosensing and opto-mechanics applications

Unlike plasmonic metasurfaces, all-dielectric metasurfaces benefit a lot from its high transmission, low losses and compatibility with current semiconductor technologies. Furthermore, high-index low-loss dielectric material is always a promising candidate for engineering functional metasurfaces structures due to the large index contrast between the metasurface layer and the substrate. Amorphous silicon is an ideal one thanks to its wide spectra transparent window starting from 700 nm to mid-infrared region and high refractive index property. Therefore, in this chapter, we will discuss about all-dielectric amorphous silicon metasurface in biosensing and opto-mechanics fields.

6.1 Dielectric metasurfaces for biosensing

6.1.1 Introduction

Biosensors are pivotal in diagnosing epidemics for public and global health, discerning drugs and materials for national security and defense, assisting in disease detection and drug discovery for fundamental biology and pharmacology. These applications demand biosensors to be sensitive and rapid enough. Nowadays, researchers in the bio-sensing field are pushing the performance of optical sensors at a higher level, utilizing either plasmonic or all-dielectric nanostructures. Both of them have their own advantages. Plasmonic bio-sensors [32] can confine and enhance light at the surface of the nanostructures, therefore, they can increase the light matter interaction, which is advantageous for detection of single molecules or monolayer substances. On the other hand, all-dielectric sensors cannot provide the localized field enhancement as plasmonic ones, however, due to their low loss and near unity efficiency characters, all-dielectric ones can provide a significant resonance contrast and high quality factors. Based on good designs, all-dielectric metasurfaces can provide clean, narrow, deep, one-peak resonance which can be analyzed in more obvious and

convenient ways. In this chapter, we will talk about this new design which can provide a narrow, pronounced, clean one-peak resonance metasurface for bio-sensing applications.

6.1.2 Design the metasurface for biosensing

We use tilted elliptical pillar pairs as our design. This design can provide a very sharp and pronounced resonance, which gives high quality factor. Moreover, dipole coupling in the pair forces the electric field localizing on the particle edges rather than their centers. The other reason to use this specific design is we want the adjacent elements to have forces which are perpendicular to the metasurface plane when they are excited via external electromagnetic field, and this will be described in detail in the next chapter. The sharp line-width (Fig.6.1(a)) is due to the collective resonance rather than the specific design of elliptical shape or the diffraction grating effect. The elliptical shape of the meta-atoms could be changed into rectangular without losing the metasurface properties. We chose elliptical shape because it is better for the fabrication, while the rectangular shape is difficult to fabricate in practice when the element size is very small (the edges can't be sharp corners). If the design is parallel ellipses, the resonances of the nanoparticles or metasurfaces cannot be excited. We can see in Figure6.1(b), and the excitation electric field is more overlapped to the minor axis of the ellipse. The periods of the pairs are x = 490 nm, y = 368 nm, the ellipse tilted angle is 13 deg, the ellipse long axis length is 269 nm, the ellipse short axis length is 98 nm and their thickness is 100 nm.

The standard definition of *Spectral Sensitivity* [171] is the wavelength shift divided by the refractive index change

$$S = \Delta\lambda / \Delta n. \tag{6.1}$$

The spectral sensitivity has a unit of nm/RIU, where RIU is the abbreviation of refractive index unit. Sensitivity is not enough to determine how good the sensing device truly is, and the resonance width of the sensing device is also crucial to the quality of the device. Therefore, full width half maximum (FWHM) of the resonance is introduced here to define the resonance's width of the sensing device. Hence, a more comprehensive index of Figure of Merit (FOM) is defined as the following equation

$$FOM = S / FWHM. \tag{6.2}$$

Figure 6.1(a) shows the design of metasurface which is made from an array of tilted elliptical amorphous silicon pillar pairs on glass substrate embedded with liquid on top. We simulated the metasurface's spectra with different immersion liquid (water and ethanol). We calculate the sensitivity and conclude that it is 250 nm/RIU, FWHM is about 1.5 nm, and FOM is 167. The reason for the spectral shift is the surrounding medium's refractive index change, which leads changing the contrast

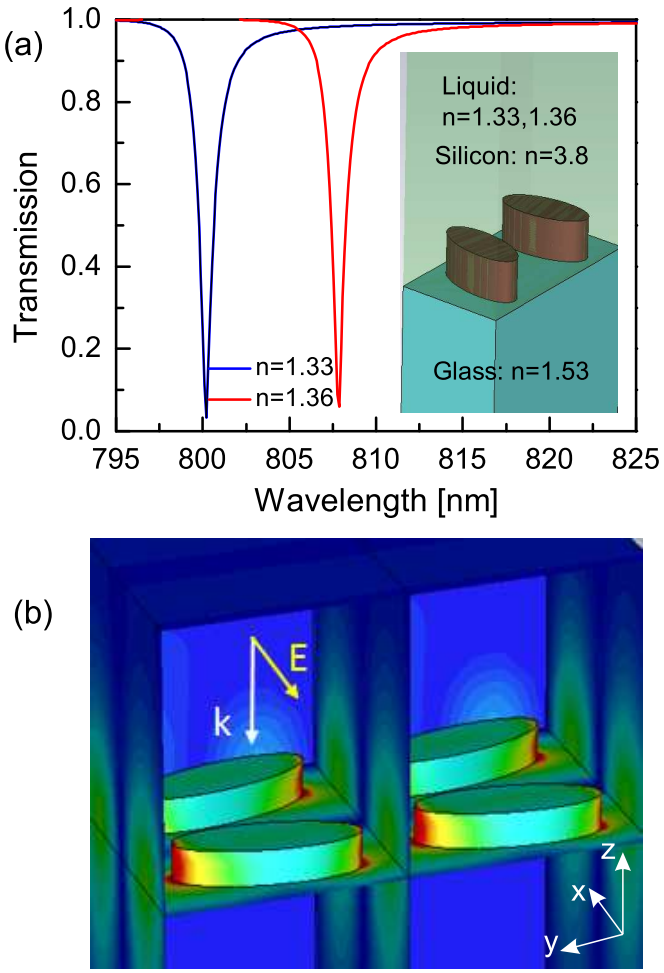

Figure 6.1: (a) The numerically calculated normal-incidence linear optical transmittance spectra of the metasurface in the liquid with refractive index of 1.33 (water) in blue color, and 1.36 (ethanol) in red color. The inset shows metasurface's geometry. (b) The power distribution of EM field on metasurface with x-polarized excitation at 800 nm.

of the refractive index between the metasurface and the surrounding medium. Figure 6.1(b) indicates the power distribution on the metasurface. Our design utilizes high index amorphous silicon and electric dipoles coupling, and the most of the field can be distributed in the gap among the elements (Fig.6.1(b)). Therefore, the field can interact with sensed objects strongly at the area adjacent to the metasurface. We use the high refractive index (RI) of Si for the design because we want to increase the contrast of the RI between the metasurfaces layer and the surrounding medium (such as the substrate or the immersion liquid). The high contrast gives better resolution of the sensing device as well as gives a better resonance (sharper linewidth, and higher resonance contrast). Coupling of the individual dipoles can provide the collective effect, which makes the most of the field at the gap between the elements,

rather than in the elements.

6.1.3 Dielectric metasurface fabrication

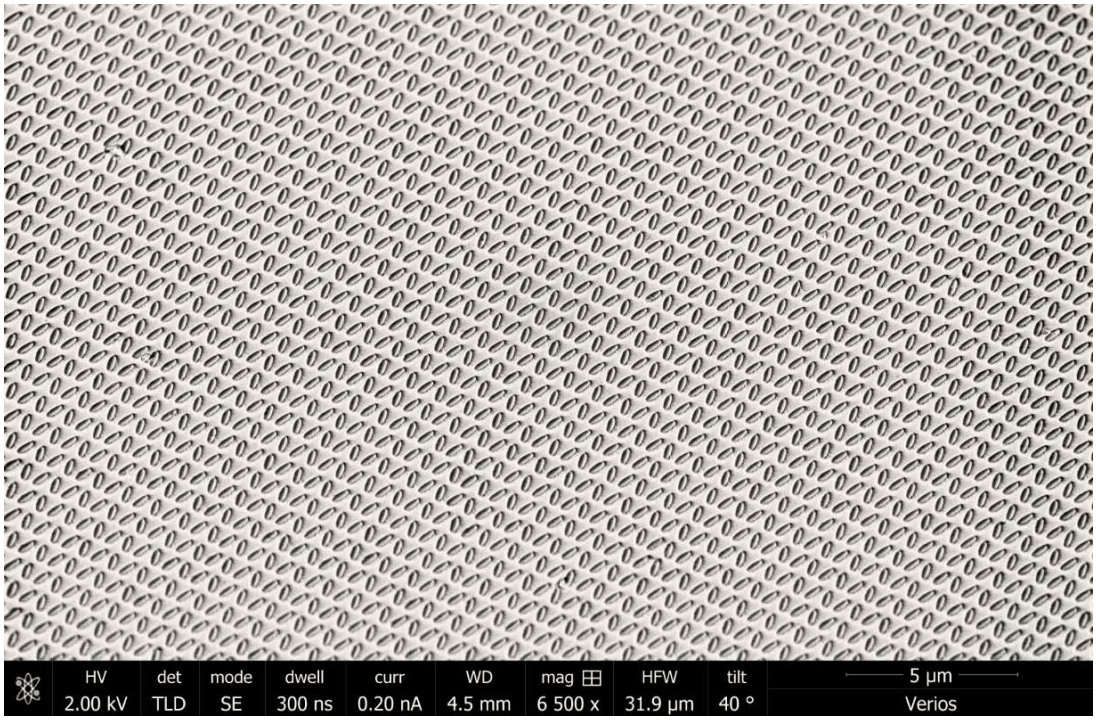

Figure 6.2: Scanning electron microscope image of the fabricated silicon metasurface on glass substrate with the oblique view.

To fabricate the biosensing metasurface, we firstly deposit a layer of 100 nm thick amorphous silicon on glass substrate. We process the deposition with an Oxford Instrument Plasma-enhanced chemical vapor deposition (PECVD) machine with 475 sccm Helium and 25 sccm Silane at 250 degree Celsius, 1500 mTorr chamber pressure, 15 W forward power. We then performed an electron-beam lithography (EBL) on a silicon-glass wafer (100 nm top silicon thickness, 200 μm glass thickness) using the negative-tone resist ma-N 2403. After cleaning the top silicon surface by oxygen plasma (2 min, 200 W) with barrel etcher, we first spin-coated HMDS (Hexamethyldisilazane) as an adhesion promoter (3000 rpm, 30 s), directly followed by spin-coating the electron-beam resist (3000 rpm, 30 s), resulting in a resist thickness of 300 nm. We performed both a pre-exposure bake (100 C, 1 min) and a post-exposure bake (90 C, 1 min). After electron-beam exposure (7.5 μm aperture, 30 kv electron gun voltage), development was performed by inserting the sample into ma-D 525 developer for 35 s, followed by rinsing it in de-ionized water for 2 minutes. The resulting resist pattern was then used as an etch mask for an inductively coupled plasma (ICP) etching process (15 mTorr chamber pressure, 15 W RF power, 400 W ICP power) using CHF_3 (50 sccm) and HF_6 (1.8 sccm) as etch gases. Remaining resist was removed by oxygen

plasma.

6.1.4 Protein A/G and antibody IgG detection

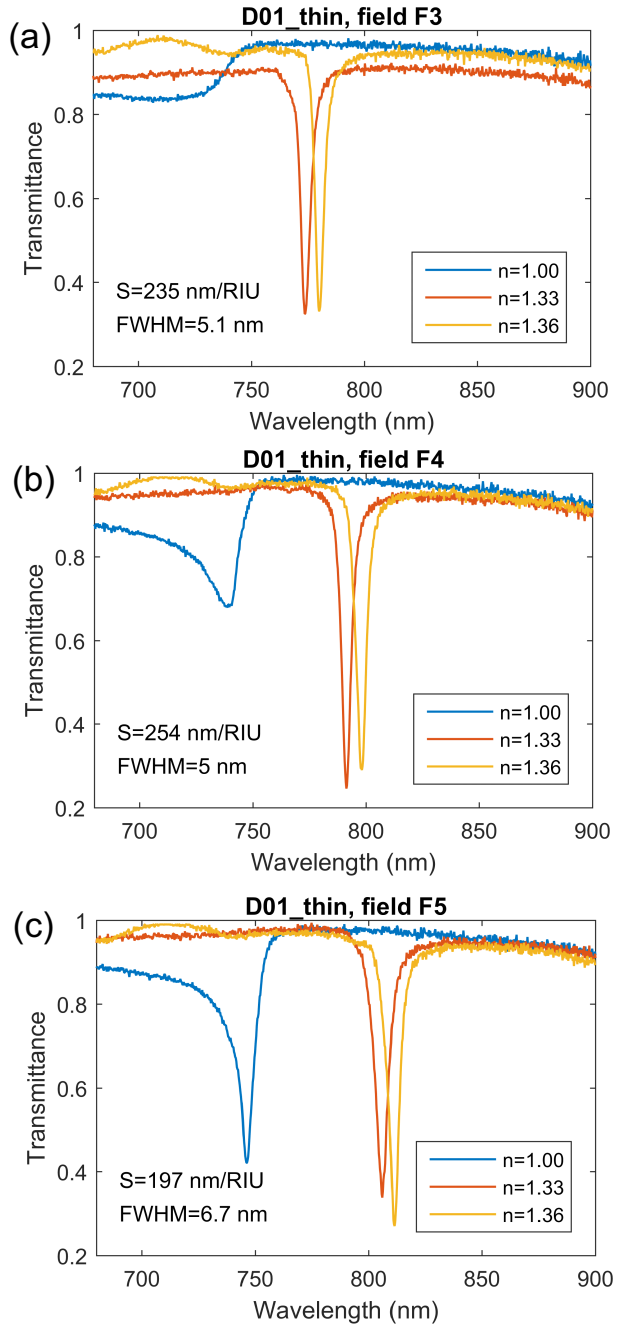

Figure 6.3: The measured transmission spectra of field F3 (a), field F4 (b), and field F5 (c) in air, water and ethanol, respectively.

We use protein A/G and antibody IgG for the experiment. IgG stands for Im-

munoglobulin G, which is a type of antibody. The protein A/G is a recombinant fusion protein that combines IgG binding domains of both Protein A and Protein G. Optical characterization of the elliptical pillar arrays is performed through spectroscopy measurements, where we use a polarized broadband white light source. Light transmitted from the sensor chip is collected by a high-magnification objective lens (100X Nikon objective lens with NA: 0.6 embedded in a Nikon Eclipse-Ti microscope) and then detected with a SpectraPro 500i spectrometer. Transmission spectra are determined by taking the ratio between the spectra of light transmitted from the aperture system and the spectra of the bare light source. This method helps us to consider the spectral shape of the halogen light source in order to accurately determine the linewidth of the metasurface resonances. We measured the transmission spectra in different refractive index liquids (Fig. 6.3). We compared the spectra in air (blue curve), water (red curve) and ethanol (yellow curve). The spectral red-shifts as the refractive index increases. We designed metasurface in water and ethanol, and it does not optimized in air, so in air it has much less response than the others. The devices' sensitivities (Fig. 6.3) are comparable with the simulation results. However, the spectra line width in experiment (5-6 nm) is much wider than in simulation (1.5 nm). This is due to the fabrication imperfections, such as the etched silicon nano pillars' surfaces are not smooth and it gives rise to some scattering loss; the metasurface field is not large enough in experiment compared with simulation one (infinite array), so that the coherent length is influenced. We manufactured 5 different metasurfaces fields using different exposure doses in fabrication process. These are named as field F1 to field F5. Because the field F1 and the field F2 are underexposed, they do not show any resonance in the transmission spectral measurements. Therefore, we just take analysis on the remaining three fields, namely field F3, field F4 and field F5 (Fig. 6.3).

After the spectra measurement of metasurface in different liquids, we performed a protein/antibody binding experiment using protein A/G and antibody IgG on functionalized sensor chips. Firstly, we performed the functionalization of our sensors such that the protein A/G is binding uniformly on the surface of glass substrate as well as silicon pillars which naturally contain a thin layer of native oxide. Secondly, we perform the microfluid experiment. Fig. 6.4(a) presents the real-time results of resonance peak shifts ($\Delta\lambda$) with different density of IgG, which is measured in a microfluid chamber, and our metasurfaces were able to resolve the capture of 5 ng/ml IgG on protein A/G with acceptable signal to noise levels. Then, we use the stable wavelength shift value of Fig. 6.4(a) to compare the density of IgG as Fig. 6.4(b) shows. We only consider the linear portion (inset of Fig. 6.4(b)) because the total amount of protein A/G on metasurface is fixed, which requires the limited dose of IgG to be detected. If the IgG's density is above a certain threshold, the surface protein A/G will quickly be fully bound with IgG, which leads to the saturation. The refractive index difference will stay the same level, even the density of the IgG increases. Therefore, this sensing device is only applicable for low density detections, which is an excellent candidate for sensitive detection.

In order to test if multi-functional chip is possible for the future detection ap-

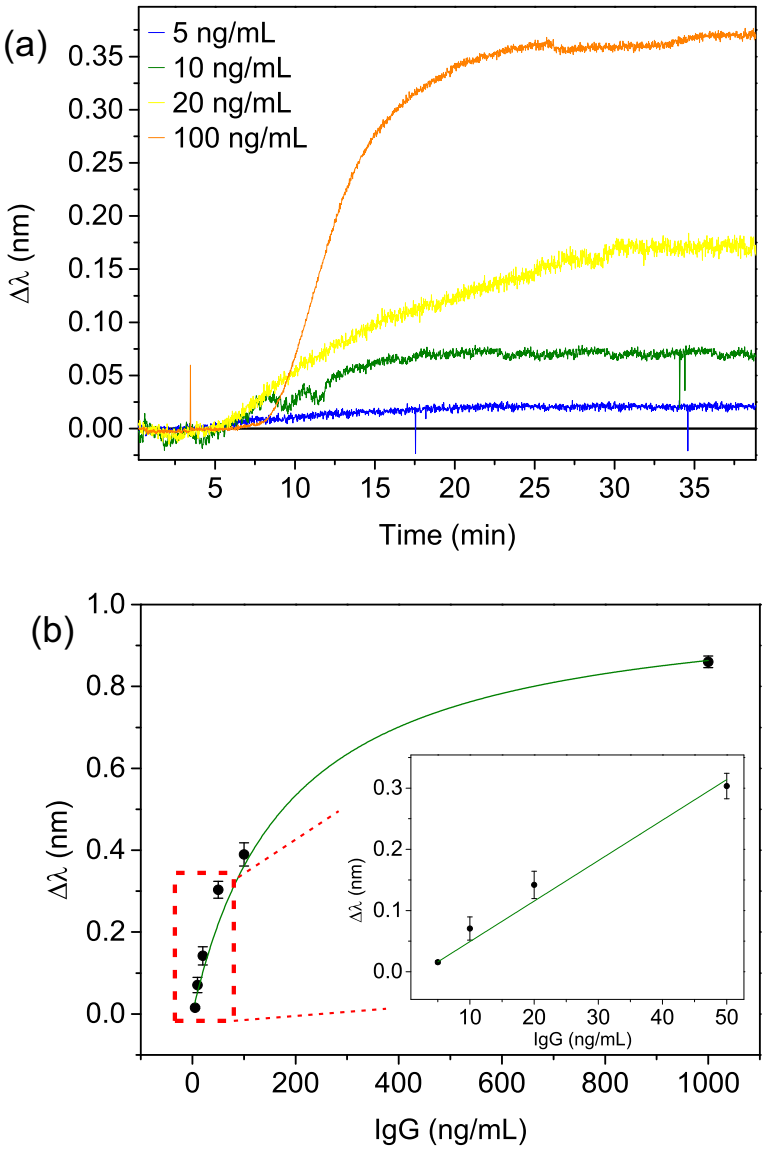

Figure 6.4: The real-time microfluid bioassay measurements. (a) Monitor metasurface resonance peak wavelength shifts as protein (A/G) and antibody (lgG) binding with different density of lgG. (b) The final wavelength shift with respect to lgG's density, according to Fig. (a). The inset shows the zoomed in image of linear part.

plications, the next experiment we perform is monitoring the real-time results of resonance peak shifts ($\Delta\lambda$) with different density of IgG for three different metasurfaces with different resonances at the same time. We can see from Fig. 6.5 that our metasurfaces not only can detect low density of IgG, but also can distinguish the shift difference between metasurfaces with the same amount density of IgG. Although Fig. 6.5(c) indicates too much noise for distinguishing different sensors due to the wide linewidth (Fig. 6.3) of the metasurfaces, our sensors are good enough for low density antibody detections already. We can decrease the metasurfaces res-

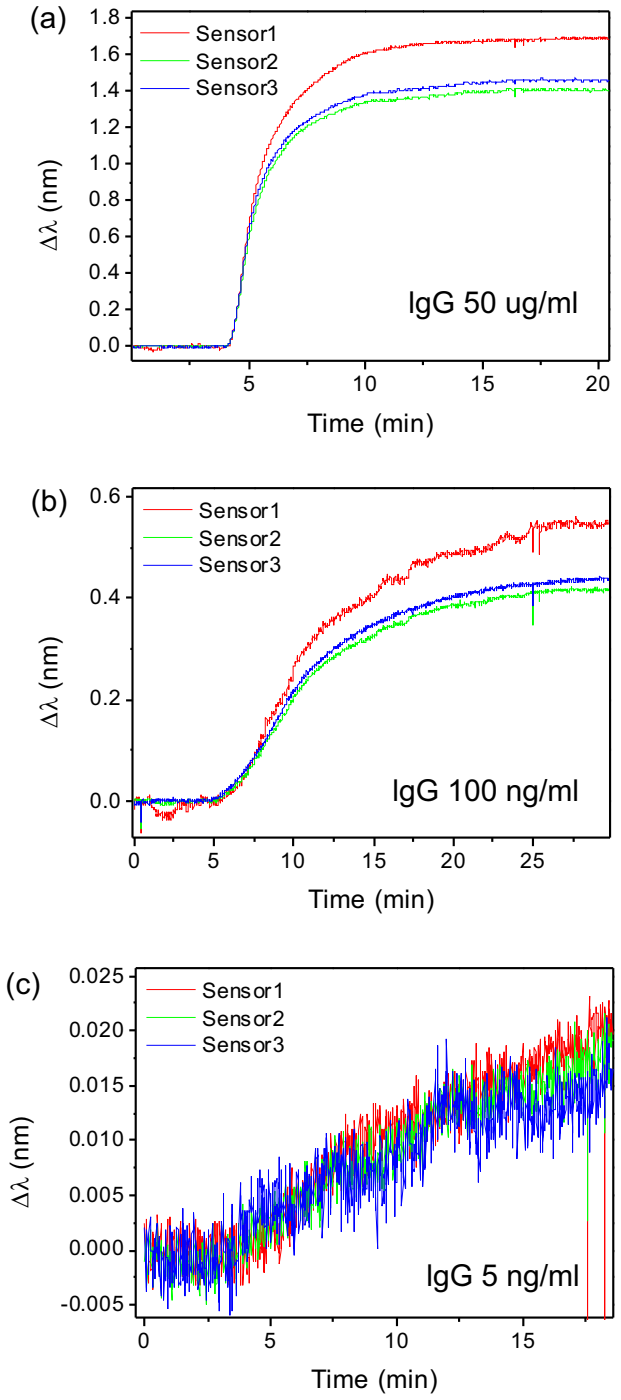

Figure 6.5: The real-time microfluid bioassay measurements for the three sensors (sensor1(field F3), sensor2(field F4), sensor3(field F5)) at the same time, with the density of IgG (a) 50 μg/ml, (b) 100 ng/ml, (c) 5ng/ml.

onance linewidth by increasing the detection area size to get larger coherent length, and improve the quality of metasurfaces.

6.1.5 Conclusion

In conclusion, we have realized an all-dielectric metasurface composed of array of amorphous silicon nano-elliptical pillar pairs. To this end, we have implemented and successfully demonstrated sharp resonances dielectric metasurface bio-sensors. We have studied the optical properties of this metasurface and investigated its sensitivities for bio-detection. We show that our design supports sharp resonance with figure of merit over 50 experimentally and performed our detection limit which is below 5 ng/ml. In particular, we have identified that the multi-functional chips are possible based on our three metasurfaces real-time experiment. Therefore, our dielectric metasurface can be used in a range of sensing applications.

∗This chapter's measurement results are based on our collaboration with Mr. Cenk Ozdemir, Dr. Andreas Tittl and Prof. Hatice Altug from EPFL Lausanne. Dr. Mingkai Liu designed this metasurface.

6.2 Polarization-induced symmetry breaking in metamaterials

6.2.1 Introduction

Metamaterials provide a unique tool-kit to tailor the electromagnetic space and control the propagation of electromagnetic waves in ways unimagined before. The great design flexibility of these structures allows one to manipulate the amplitude, phase and polarization of waves on demand. [61, 99, 113, 172–174] In the design of metamaterials, structural symmetry sets fundamental bounds on the electromagnetic properties that can be achieved. For example, optical chiral effects including circular dichroism and circular birefringence typically require stereoscopic structures with broken mirror symmetry (three-dimensional chirality), [175–179]while circular conversion dichroism (elliptical dichroism) can be found in planar chiral geometries (two-dimensional chirality). [180–182]

Recently, much effort has been devoted to the development of dynamically tunable metamaterials [183–186]. Although the modulation of optical chiral effects is achieved by hybridizing chiral metamaterials with tunable media, [187, 188] the effects demonstrated are highly dispersive since they are based on a resonance shift. To arbitrarily manipulate the optical chiral effect, i.e. to not only control the strength but also the sign of chirality over the entire resonance band, one needs to dynamically and spatially control the *structural symmetry* at the *subwavelength* scale. This becomes challenging for metamaterial structures operating at infrared or optical frequencies,

and introducing dielectrics to avoid the high losses of metals further increases the demands on the design.

One of the promising approaches for reconfiguring metamaterials is to exploit optomechanical effects [118, 189–193]. As has been shown in previous studies, the direction of the optical force acting on optomechanical structures is determined by the symmetry of the eigenmode profiles. [194–196] To generate an optical force in a certain direction, one also needs to break the structural symmetry in that direction [118, 190, 197] – this is the case when the gradient force of the system dominates. However, in metamaterials, gradient and scattering forces coexist, and the latter can be designed to be much stronger than the former. Importantly, since the scattering force has many degrees of freedom controlled by the incident wave, it provides a new possibility to generate an optical force and even control its direction without the restrictions imposed by structural symmetry.

Here, we introduce an optomechanical paradigm that allows full spatial control of metamaterials working at infrared and optical frequencies. We first show analytically that for a general two-resonator coupled system, the optical forces acting on the two resonators are asymmetric as long as the incident wave overlaps with the two normal modes of the system, i.e. the symmetric and antisymmetric modes. We propose a simple system based on non-parallel coupled electric dipoles which is inherently achiral (mirror symmetric). We show analytically and numerically that due to the interaction and the collective enhancement in the array structure, the *scattering* force acting on the dipole meta-atoms can become highly asymmetric if the incident polarization *explicitly* breaks the mirror symmetry of the system, i.e. when it is not aligned with the symmetry axes of the system or becomes circularly polarized. This relative force can be employed to actuate the structure and transform it into a *stereoscopic chiral metamaterial*. Importantly, the induced optical activity is purely nonlinear, and the handedness of the nonlinear optical activity can be controlled with the polarization of the incident pump wave. By further introducing a spatial gradient in the incident polarization, one can generate chiral domains and spatially control the scattering of left and right circular polarizations, paving a way towards *dynamic spatial modulation* of light with *subwavelength resolution*.

6.2.2 Results and Discussions

6.2.2.1 Analytical Modeling of Optical Forces in Coupled Pairs of Non-parallel Dipoles

To provide clear physical insight to this effect, we start with the simplest unit: a coupled pair of non-parallel electric dipoles, in which the dipole moments are aligned in the $x-y$ plane, as shown in Fig. 6.6 (a). Although we use dipole model here, there is no limitation on the actual implementation of the meta-atom as long as its electric response is highly polarization-dependent. The dipole meta-atoms have identical geometries but opposite orientation angles, and they form a coupled unit satisfying mirror symmetry. We define the two different orientations of meta-atoms with respect to y axis as $\theta_1 = -\theta_2 = \theta$. It will be subsequently shown that the effect

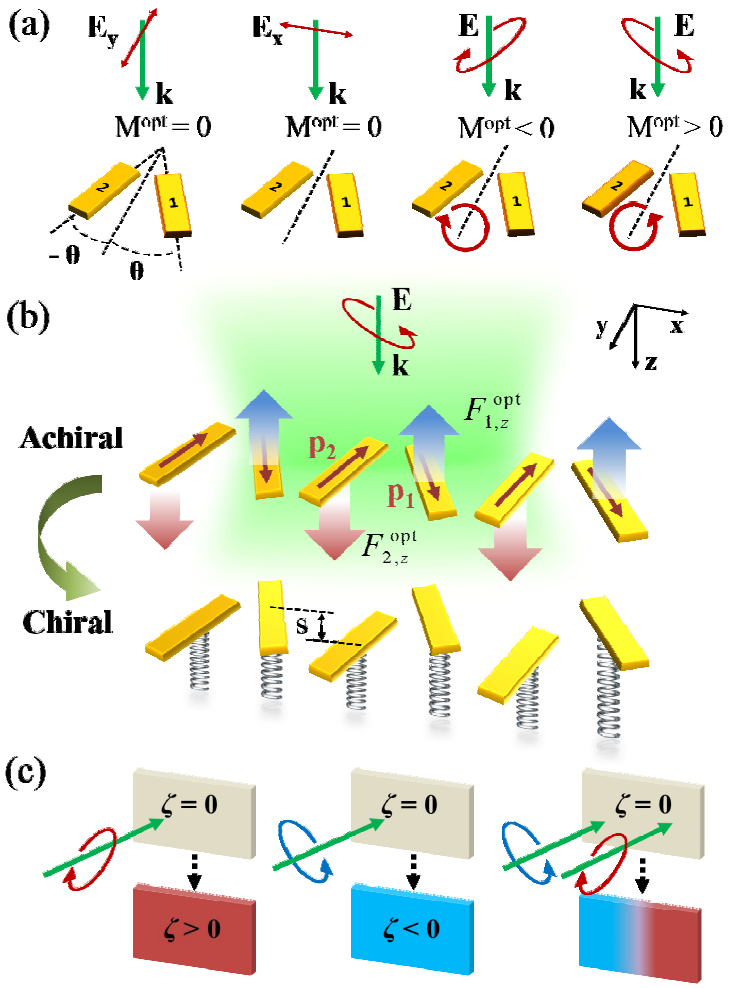

Figure 6.6: (a) Schematic of a pair of non-parallel coupled dipoles. The optical forces acting on the dipoles become different when the incident polarization is not aligned with the symmetry axes, leading to a transverse optical torque $M^{\text{opt}} \neq 0$; the direction of torque can be controlled with incident polarization. (b) Schematic of a zig-zag array of dipole meta-atoms. When excited with an appropriate incident polarization, the optical force acting on the dipoles becomes highly asymmetric near the resonant frequency of the antisymmetric mode. By introducing flexible mechanical feedback, the relative force can be employed to transform the planar achiral structure ($s = 0$) into a stereoscopic chiral metamaterial ($s \neq 0$). (c) The handedness of the optomechanically induced chirality, denoted by chiral index ζ, can be controlled with the incident polarization.

in a one-dimensional or two-dimensional array is qualitatively the same and can be substantially enhanced due to collective resonance.

The key effect studied in this paper is the optical force acting on the dipole meta-atoms: $F^{\text{opt}} = F^{\text{int}} + F^{\text{ext}}$, where F^{int} is the internal force (gradient force) due to the near field interaction of meta-atoms via the scattered field ($\mathbf{E}^{\text{s}}, \mathbf{B}^{\text{s}}$), and F^{ext} is

the external force (scattering force) due to the interaction of meta-atoms and the excitation plane wave ($\mathbf{E}^{\mathrm{i}}, \mathbf{B}^{\mathrm{i}}$). We are particularly interested in the z component of the time-averaged optical force. The forces can be determined from the following equations (see supplementary material for details):

$$F_z^{\mathrm{int}} \propto \left[\rho(\mathbf{r})\rho^*(\mathbf{r}') - \mathbf{J}(\mathbf{r}) \cdot \mathbf{J}^*(\mathbf{r}')\right] \mathbf{e_R} \cdot \mathbf{z}, \tag{6.3}$$

$$F_z^{\mathrm{ext}} = \frac{k_{\|}}{2} \mathrm{Im}\left[\mathbf{p} \cdot (\mathbf{E}^{\mathrm{i}})^*\right], \tag{6.4}$$

Here, ρ and $\mathbf{J}$ are the polarization charge and current of a meta-atom with an effective electric dipole moment $\mathbf{p}$. F_z^{int} discribes the internal force between two coupled meta-atoms, with their displacement vectors denoted by $\mathbf{r}$ and $\mathbf{r}'$, respectively; $\mathbf{e_R} = (\mathbf{r} - \mathbf{r}')/|\mathbf{r} - \mathbf{r}'|$. Note that for a more general excitation field, Eq. (6.4) can contain additional terms due to the local gradient of intensity $\nabla|\mathbf{E}^{\mathrm{i}}|^2$ and the local curl of spin density $\nabla \times [\mathbf{E}^{\mathrm{i}} \times (\mathbf{E}^{\mathrm{i}})^*]$ [198], but they all vanish for homogeneous plane wave excitation.

Equations (6.3) and (6.4) show that while the direction of F_z^{int} is inherently bounded by the mode symmetry of the coupled system, the direction of F_z^{ext} is determined by the relative phase with respect to the incident field. For example, for a meta-atom in the coupled system, F_z^{int} changes sign when the coupled mode changes from symmetric to antisymmetric state [consider $\rho(\mathbf{r}') \to -\rho(\mathbf{r}')$ and $\mathbf{J}(\mathbf{r}') \to -\mathbf{J}(\mathbf{r}')$], and it vanishes when all the meta-atoms are on the same plane ($\mathbf{e_R} \cdot \mathbf{z} = 0$). Thus it is *impossible* to actuate the originally planar structure in the z direction and transform it into a stereoscopic structure if only F^{int} is employed. In contrast, F^{ext} is free from such restriction, and the strength of F^{ext} can become much stronger in an array due to the collective enhancement (as shown below).

To model the electromagnetic interaction, we employ a semi-analytical model based on the free space Green's function [199–202] (see supplementary material for details). The coupled equations for a two-resonator system can be expressed explicitly as follows:

$$\mathrm{i}\omega \begin{bmatrix} Z_{11} & Z_{12} \\ Z_{21} & Z_{22} \end{bmatrix} \begin{bmatrix} Q_1 \\ Q_2 \end{bmatrix} = \begin{bmatrix} \mathcal{E}_1 \\ \mathcal{E}_2 \end{bmatrix}, \tag{6.5}$$

where Q is the mode amplitude that describes the resonant behavior of meta-atoms. The impedance matrix describes the self and mutual interaction of the meta-atoms, in which Z_{ii} and Z_{ij} are the effective self impedance and mutual impedance, respectively. All the matrix elements can be defined from the normalized current and charge distribution of the eigen mode of each individual meta-atom [199–202]; from symmetry we get $Z_{11} = Z_{22}$, $Z_{12} = Z_{21}$. $\mathcal{E}$ is the effective electromotive force imposed by the incident field; for plane wave excitation, $\mathcal{E} = \mathbf{l} \cdot \mathbf{E}^{\mathrm{i}}$,where $\mathbf{l} = \mathbf{p}/Q$ is the normalized dipole moment of a single meta-atom.

Our two-resonator coupled system supports two normal modes: symmetric mode $\hat{\mathbf{e}}_{\mathrm{S}} = \frac{1}{\sqrt{2}}[1, 1]$ and antisymmetric mode $\hat{\mathbf{e}}_{\mathrm{A}} = \frac{1}{\sqrt{2}}[1, -1]$. The coupled equations can

be rewritten in a more instructive form based on the eigenbasis of normal modes:

$$\mathrm{i}\omega \begin{bmatrix} Z_\mathrm{S} & 0 \\ 0 & Z_\mathrm{A} \end{bmatrix} \begin{bmatrix} Q_\mathrm{S} \\ Q_\mathrm{A} \end{bmatrix} = \begin{bmatrix} \mathcal{E}_\mathrm{S} \\ \mathcal{E}_\mathrm{A} \end{bmatrix}, \tag{6.6}$$

in which $Z_\mathrm{S} = Z_{ii} + Z_{ij}$, $Z_\mathrm{A} = Z_{ii} - Z_{ij}$ are the impedances of symmetric and antisymmetric modes, respectively; $Q_S = (Q_1 + Q_2)/\sqrt{2}$ and $Q_A = (Q_1 - Q_2)/\sqrt{2}$ are the corresponding mode amplitudes; $\mathcal{E}_S = (\mathcal{E}_1 + \mathcal{E}_2)/\sqrt{2}$ and $\mathcal{E}_A = (\mathcal{E}_1 - \mathcal{E}_2)/\sqrt{2}$ are the corresponding effective electromotive forces. They can be obtained via the following transformation:

$$\begin{bmatrix} Z_\mathrm{S} & 0 \\ 0 & Z_\mathrm{A} \end{bmatrix} = \overleftrightarrow{T} \begin{bmatrix} Z_{11} & Z_{12} \\ Z_{21} & Z_{22} \end{bmatrix} \overleftrightarrow{T}^{-1}, \tag{6.7}$$

$$\begin{bmatrix} Q_\mathrm{S} \\ Q_\mathrm{A} \end{bmatrix} = \overleftrightarrow{T} \begin{bmatrix} Q_1 \\ Q_2 \end{bmatrix}, \tag{6.8}$$

$$\begin{bmatrix} \mathcal{E}_\mathrm{S} \\ \mathcal{E}_\mathrm{A} \end{bmatrix} = \overleftrightarrow{T} \begin{bmatrix} \mathcal{E}_1 \\ \mathcal{E}_2 \end{bmatrix}, \tag{6.9}$$

where

$$\overleftrightarrow{T} = [\hat{\mathbf{e}}_\mathrm{S}, \hat{\mathbf{e}}_\mathrm{A}]^T = \frac{1}{\sqrt{2}} \begin{bmatrix} 1 & 1 \\ 1 & -1 \end{bmatrix} \tag{6.10}$$

is the transformation matrix.

We assume that both meta-atoms are initially in the same plane, i.e. the separation of the two meta-atoms in the z direction is $s = r_{1,z} - r_{2,z} = 0$. In this case, $F_z^{\mathrm{int}} = 0$. From Eq. (6.4), we can get the relative force with an explicit expression

$$\Delta F_z = F_{1,z} - F_{2,z} = \frac{k_\parallel}{2} \mathrm{Im}\left(Q_1 \mathcal{E}_1^* - Q_2 \mathcal{E}_2^*\right). \tag{6.11}$$

Using Eq. (A.7) and Eq. (A.8), the relative force can be rewritten as

$$\begin{aligned} \Delta F_z &= \frac{k_\parallel}{4} \mathrm{Im}\left(Q_S \mathcal{E}_A^* + Q_A \mathcal{E}_S^*\right) \\ &= -\frac{k_\parallel}{4\omega} \mathrm{Re}\left(\frac{\mathcal{E}_S \mathcal{E}_A^*}{Z_\mathrm{S}} + \frac{\mathcal{E}_A \mathcal{E}_S^*}{Z_\mathrm{A}}\right). \end{aligned} \tag{6.12}$$

Equation (6.12) shows that in order to achieve a nonzero relative force, it is essential to have the excitation field overlap with both symmetric and antisymmetric modes so that neither $\mathcal{E}_S$ nor $\mathcal{E}_A$ vanishes. It should be noted that this conclusion is quite general since the model used from Eq. (6.5) to Eq. (6.12) is valid for any two-resonator coupled systems.

Now consider an incident plane wave propagating in the $x-z$ plane:

$$\mathbf{E}^{\mathrm{i}} = \begin{pmatrix} E_x \\ E_y \\ E_z \end{pmatrix} = E \begin{pmatrix} \sin\psi\cos\alpha \\ e^{\mathrm{i}\varphi}\cos\psi \\ \sin\psi\sin\alpha \end{pmatrix} e^{i(-\omega t + k_{\parallel} z + k_{\perp} x)}, \tag{6.13}$$

where α is the angle of incidence, and ψ and φ describe the polarization state. At normal incidence, the relative force can be written in a concise form

$$\Delta F_z = -\frac{kl^2|\mathbf{E}^{\mathrm{i}}|^2 \sin 2\theta \sin 2\psi}{2\omega} \mathrm{Re}\left(\frac{e^{-\mathrm{i}\varphi}}{Z_{\mathrm{S}}} + \frac{e^{\mathrm{i}\varphi}}{Z_{\mathrm{A}}}\right). \tag{6.14}$$

Equation (6.14) shows that for the non-degenerate configuration, i.e. $\theta \neq 0^\circ$ or 90°, the optical forces acting on the two meta-atoms can become asymmetric if the incident polarization explicitly breaks the system mirror symmetry, i.e. $\psi \neq 0^\circ$ or 90° [note that $\mathcal{E}_A$ ($\mathcal{E}_S$) becomes zero when $\psi = 0^\circ$ (90°)]. Importantly, the sign of the relative force can be manipulated by the incident polarization state ψ and φ, and the optimum value of ψ is $\pm 45^\circ$ at normal incidence. The force asymmetry can be enhanced at the resonances of symmetric and anti-symmetric modes, and the enhancement factor is directly proportional to the quality factor of the resonance (as shown below). Note that while there are many ways to construct an anisotropic dipole meta-atom, the optimum design should provide the maximum normalized dipole moment l.

From energy conservation, it can be proved that for electric dipoles without material loss, the square of the normalized dipole moment l is proportional to the real part of the self-impedance that represents the radiative loss

$$\mathrm{Re}(Z_{ii}) = \frac{k^3 l^2}{6\pi\epsilon\omega} = \frac{k^2 \eta l^2}{6\pi}, \tag{6.15}$$

where $\eta = \sqrt{\mu/\epsilon}$ is the wave impedance of the environment. Substituting Eq. (6.15) into Eq.(6.14), we get

$$\Delta F_z = -\frac{3\pi|\mathbf{E}^{\mathrm{i}}|^2 \sin 2\theta \sin 2\psi}{\omega^2 \mu} \mathrm{Re}(Z_{ii}) \mathrm{Re}\left(\frac{e^{-\mathrm{i}\varphi}}{Z_{\mathrm{S}}} + \frac{e^{\mathrm{i}\varphi}}{Z_{\mathrm{A}}}\right). \tag{6.16}$$

Note that the factor $\mathrm{Re}(Z_{ii})\mathrm{Re}(1/Z_{S(A)})$ represents the enhancement of the relative force, and for linearly polarized exciation ($\varphi = 0$), it reaches the maximum value of $\mathrm{Re}(Z_{ii})/\mathrm{Re}(Z_{S(A)})$ at the resonant frequencies of the normal modes. Therefore, the enhancement of the relative force is directly proportional to the ratio of the linewidths of the single dipole resonance and the coupled normal modes.

6.2.2.2 Collective Enhancement in Arrays

The force asymmetry can be significantly enhanced when such non-parallel coupled dipole pairs form a zig-zag array, as shown in Fig. 6.6 (b). For simplicity, we start with a one dimensional infinite periodic array, of which the coupled equations can be simplified to the same form as Eq. (6.5) using the Bloch boundary condition:

$$Q_{(i,n)} = Q_{(i,0)} e^{\mathrm{i}k_\perp n A_x} = Q_i e^{\mathrm{i}k_\perp n A_x}. \tag{6.17}$$

Here the subscript $i = 1$ or 2, denoting the two types of meta-atoms with different orientations, and n denotes the n_{th} meta-atom of type "i". A_x is the lattice constant in the x direction. The elements of the impedance matrix in Eq. (6.5) for the infinite array are redefined as:

$$Z_{ii} = Z_{(i,0),(i,0)} + 2\sum_{n=1}^{\infty} Z_{(i,0),(i,n)} \cos(k_\perp n A_x), \tag{6.18}$$

$$Z_{ij} = 2\sum_{n=0}^{\infty} Z_{(i,0),(j\neq i,n)} \cos[k_\perp (n+1/2) A_x]. \tag{6.19}$$

Since the coupled equation for the infinite array has the same form as the coupled dimer, the analysis and the conclusion from Eq. (6.5) to Eq. (6.16) is qualitatively the same. The quantitative difference comes from the collective enhancement that leads higher quality factor of the resonance. By properly manipulating the incident polarization, it is possible to generate a highly asymmetric F_z^{ext} along the array, which can be employed to trigger the symmetry breaking in the z direction, as shown below. As noted above, such flexibility is highly desirable for the optomechanical manipulation of metamaterials, since it provides the possibility to generate the optical force in directions prohibited by the symmetry of the normal modes.

To show a particular example, we first use the analytical model to calculate the scattering force acting on an infinite chain of short metallic dipoles; the forces shown in this paper are all normalized to an incident power density of 1 mW/μm^2. For simplicity, the dipoles are treated as thin current lines made from perfect electric conductors, with a sinusoidal current distribution. The angles and the length of the dipoles, the periodicity of the array are chosen as $\theta = \pm 15^\circ$, 670 nm and 1000 nm, respectively.

To maximize the relative force, we choose $\psi = 45^\circ, \varphi = 0$. Figure 6.7 (a) and (b) show the spectra of the amplitudes and phases of meta-atoms "1" and "2". The asymmetric Fano lineshape in Fig. 6.7 (a) is due to the interference of the broad symmetric mode and the narrow antisymmetric mode. At the antisymmetric mode around 201 THz [see Fig. 6.7 (b)], the optical forces acting on meta-atoms "1" and "2" become highly asymmetric. One unique feature is that the optical force acting on meta-atoms "2" can become negative [see Fig. 6.7 (c)]. In contrast to previous studies, the origin of this negative force is neither a strong gradient force [203] nor the excitation of high order multipole moments [204,205]. It is due to the unusual phase response of the meta-atoms around the antisymmetric mode. For a single electric

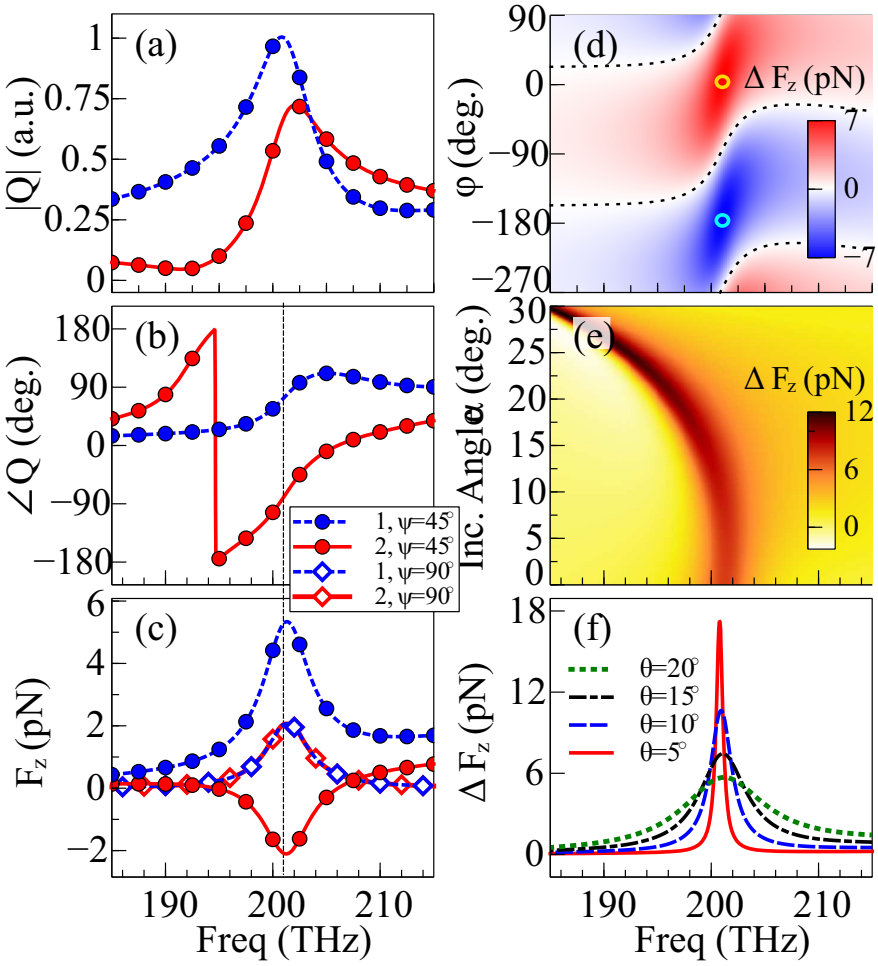

Figure 6.7: (a) The mode amplitudes, (b) the phases, and (c) the optical forces of the two types of meta-atoms "1" and "2" in an infinite array. The incident polarization is $\psi = 45°, \varphi = 0$ (45° linear polarization); the orientation angle $\theta = 15°$. The dashed line indicates 201 THz. (d) The relative force ΔF_z as a function of φ, with $\psi = 45°$; the black dotted lines indicate $\Delta F_z = 0$. (e) The relative force as a function of incident angle α, with $\psi = 45°$ and $\varphi = 0$. (f) The relative force ΔF_z for different orientation angle θ, with $\psi = 45°$ and $\varphi = 0$.

dipole, its phase around the resonance should be within $(0, \pi)$ due to causality and passivity, and therefore the imaginary part of Eq. (6.4) is positive. However, when the meta-atoms are coupled and support the antisymmetric mode, the phase of one type of meta-atom can fall into $(-\pi, 0)$ [see Fig. 6.7 (b)], leading to a negative force. As a comparison, we plot the optical forces when the incident polarization becomes 90°. In this situation, only antisymmetric mode is excited, and the forces are identical and positive [see curves marked with diamonds in Fig. 6.7 (c)].

At normal incidence, the strongest relative force exists at $|\psi| = 45°$, while the

phase φ provides an additional degree of freedom to modify the effect. As depicted in Fig. 6.7 (d), since antisymmetric mode dominates around 201 THz, the strongest effect exists when the incident polarization is close to linear [see the circles in Fig. 6.7 (d)], and the direction of the relative force reverses as φ varies by 180°. The relative force drops from maximum to zero at the resonant frequency, when the incident polarization changes from linear ($\varphi = 0, 180°$) to circular ($\varphi = \pm 90°$), which is consistent with the prediction from Eq. (6.14). Due to the collective nature of the resonance, the resonant frequency can be further red shifted by increasing the incident angle α, and the relative force becomes even stronger due to the enhanced quality factor of the resonance [Fig. 6.7 (e)]. The relative force can be further enhanced by reducing the orientation angle θ, which leads to a higher quality factor of the resonance; however the relative force starts to decrease and vanishes when the orientation angle reduces to the degenerate configuration of $\theta = 0$.

6.2.2.3 Polarization-induced Chirality

The highly asymmetric optical force shown above provides a new opportunity to control the structural symmetry of metamaterials. By hybridizing these meta-atoms with flexible mechanical feedback, it is possible to achieve controllable symmetry breaking and optical chiral effect [see schematics of Fig. 6.6 (b) and (c)]. As the meta-atoms "1" and "2" are driven towards opposite directions by the external force F_z^{ext}, the mirror symmetry of the system is broken, and the initially planar metasurface becomes a stereoscopic chiral metamaterial. Meanwhile, the internal force F_z^{int} starts to exist once the meta-atoms are no longer in the same plane. Figure 6.8 (a) and (b) depict the external force and internal force as a function of the mutual separation s with incident polarization $\psi = 45°$, $\varphi = 0$. Unlike previous studies where the internal force/torque dominates [189,190,192,193], the external force plays a major role in the current design parameters. This is mainly due to the relatively large center-to-center distance of the neighboring meta-atoms, which significantly reduces the strength of near-field interaction and the internal force.

The force induced in a finite array is quantitatively very similar. We calculate the optical force acting on an array consisting of 30 pairs of meta-atoms with the same incident polarization used in Fig. 6.7 (c). At the resonant frequency of 201 THz, the optical force shows high uniformity along the array, and apart from edge effects it agrees well with the results of the infinite array [see the Fig. 6.7 (c) and Fig. 6.8 (c) for comparison].

To estimate the nonlinear optomechanical interaction, we introduce elastic mechanical feedback into each meta-atom, with a spring constant $\kappa = 100$ pN/μm. We assume that the meta-atoms are only allowed to move in the z direction. A rigorous calculation of the system can be performed by solving both the optical response and the mechanical response simultaneously in the time-domain. However, since the mechanical oscillation period in our system is much longer than the life time of the optical resonance ($10^5 \sim 10^6$ times longer), the optical force at each integration time step of the mechanical dynamics can be approximated with the stationary solu-

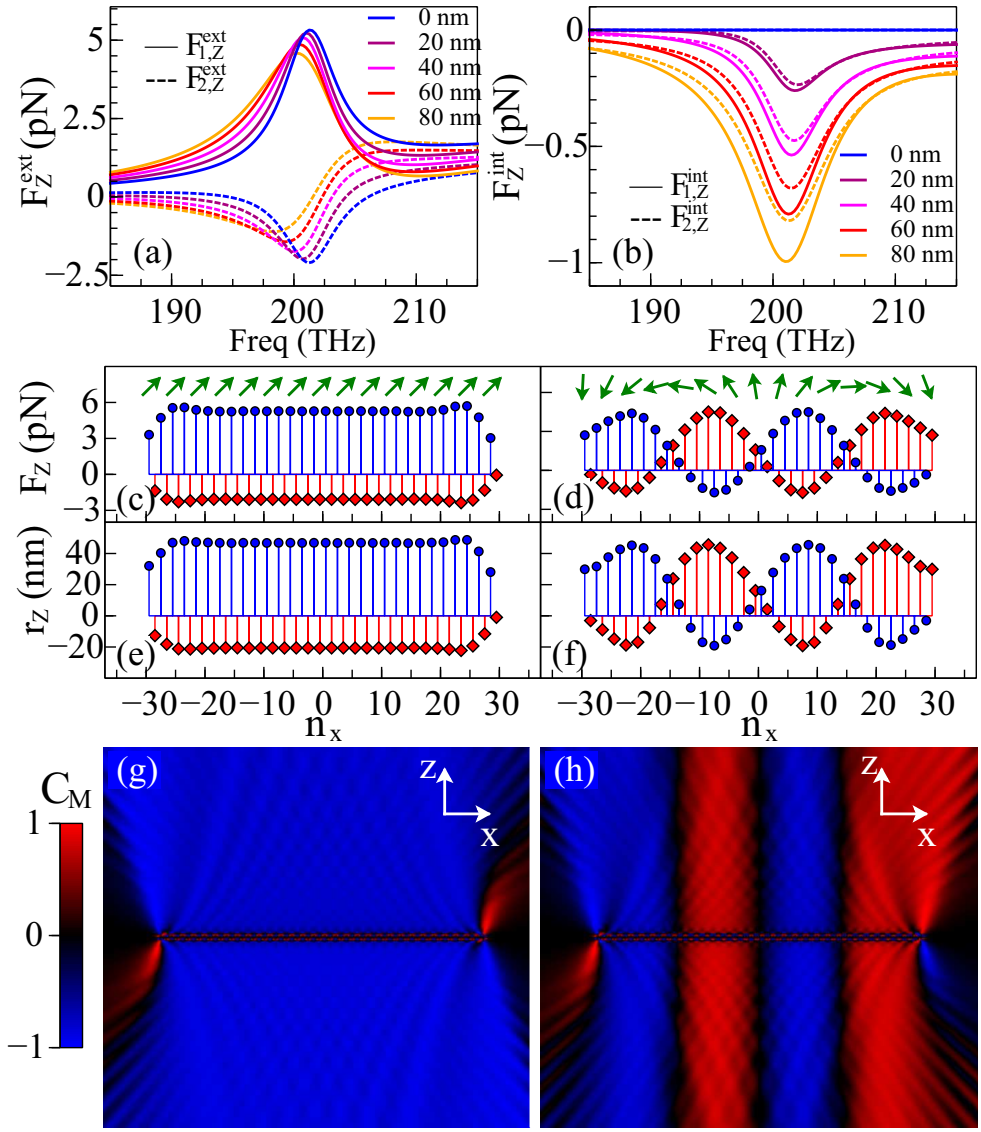

Figure 6.8: (a) and (b) The external force and the internal force acting on meta-atoms "1" and "2" in an infinite array under different separation s in the z direction, as denoted in Fig. 6.6 (b). The incident frequency is 201 THz; the orientation angle $\theta = 15°$; the incident polarization $\psi = 45°, \varphi = 0$. (c) and (d) The input optical force acting on a finite array. The blue circles and the red diamonds indicate meta-atoms "1" and "2". The green arrows show the spatial variation of the incident polarization on the $x - y$ plane. (e) and (f) The corresponding final stable displacement of the meta-atoms in the z direction. (g) and (h) The corresponding spatial distribution of the modulation contrast C_M of the scattered field in the plane of y=0, generated by an x-polarized plane wave impinging on the chiral array and chiral domains shown in (e) and (f), respectively.

tion and only depends on the instantaneous positions of the meta-atoms. Under this approximation, the coupled dynamic equations can be written as:

$$\sum_{j=1}^{2}\sum_{n=1}^{N} Z_{(i,m),(j,n)}Q_{(j,n)} = \mathcal{E}_{(i,m)}, \tag{6.20}$$

$$\mathcal{M}\ddot{\mathbf{r}}^{(c)}_{(i,m)} + \Gamma\dot{\mathbf{r}}^{(c)}_{(i,m)} = F^{opt}_{(i,m)} + F^{mech}_{(i,m)}. \tag{6.21}$$

Here $\mathcal{M}$ is the mass of the meta-atom, estimated as $5.4\times10^{-14}\mu$g based on the geometry of a silicon meta-atom proposed in Fig. 6.9. Γ is the mechanical damping due to the viscosity of the environment, $\mathbf{r}^{(c)}_{(i,m)}$ is the center of mass of the meta-atom, and $F^{mech}_{(i,m)} = -\kappa\mathbf{r}^{(c)}_{(i,m)}\cdot\mathbf{e}_z$ is the mechanical feedback force approximated with Hooke's law. Note that the electromagnetic and mechanical equations are coupled because the mutual impedance $Z_{(i,m),(j,n)}$, the mode amplitude $Q_{(i,m)}$ and the resulting optical force $F^{opt}_{(i,m)}$ are functions of the displacements of *all* the meta-atoms in the array, which in turn depend on the optical forces acting on them.

We focus on the stationary response of the system. As shown in Fig. 6.8 (e), the final stable state agrees well with the input optical force, this is mainly due to the weak nonlinear response of the force to the displacement change. To evaluate the chiral optical effect, we use an x-polarized plane wave to excite the chiral structure shown in Fig. 6.8 (e), and decompose the scattered field on the plane of $y = 0$ into left and right circular polarizations. The modulation contrast, defined as $C_M = (|E_{LCP}|^2 - |E_{RCP}|^2)/(|E_{LCP}|^2 + |E_{RCP}|^2)$, clearly demonstrates that the induced chiral structure is "right-handed" since it scatters right circularly polarized waves much more strongly.

Apart from uniform deformation, we can also generate spatially varying deformation by introducing a spatial gradient in the incident polarization. As an example, Fig. 6.8 (d) depicts the spatially varying force along the array. The input polarization shown in the figure (green arrows) can be synthesized by interfering two coherent plane waves with left and right elliptical polarizations, of which the in plane components are circularly polarized: $\mathbf{E}_\perp = E[(\mathbf{x}+\mathrm{i}\mathbf{y})e^{-\mathrm{i}k_\perp x} + (\mathbf{x}-\mathrm{i}\mathbf{y})e^{\mathrm{i}k_\perp x}] \propto E[\mathbf{x}\cos(k_\perp x) + \mathbf{y}\sin(k_\perp x)]$. The final stable state of the system consists of chiral domains that allow effective spatial modulation of circular polarizations [Fig. 6.8 (f) and (h)]. Unlike the case in our previous study, where chiral domains are generated via *spontaneous* chiral symmetry breaking [193], the method shown here is well controlled by the *explicit* symmetry breaking from the input.

6.2.2.4 Proposed Implementation in Optics

To estimate the practicality of the concept, we propose an implementation by combining the meta-atoms with flexible nano-beams [206–208]. We calculate a two-dimensional infinite array composed of silicon meta-atoms supported by silicon nitride nano-beams, as shown in Fig. 6.9 (a). The relative force is quite significant when the wave is incident from the side of the nano-beams, and can be up to eight times

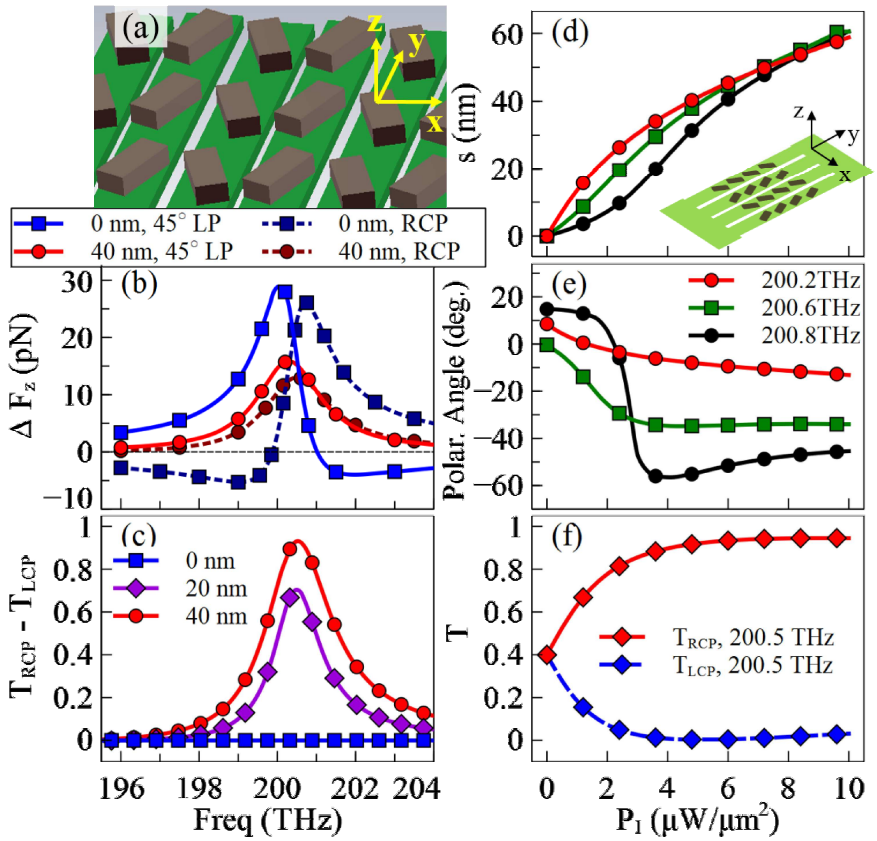

Figure 6.9: (a) Schematic of a metamaterial with silicon meta-atoms ($\varepsilon_{\mathrm{Si}} = 12.15$) supported by silicon-nitride nano-beams ($\varepsilon_{\mathrm{Si_3N_4}} = 3.92$). The lattice period in x and y directions are 1000 nm and 900 nm, respectively. The nano-beam width and thickness, and the inter-beam gap are 400 nm, 100 nm, and 100 nm, respectively. The length, width, thickness and orientation angle of the meta-atoms are 550 nm, 220 nm, 150 nm, and $\pm 22.5°$ respectively. (b) The relative force under linear and circular polarizations, and with different relative longitudinal displacement. (c) The circular dichroism under different relative displacement. (d) The relative displacement of nano-beams as a function of incident power density; the incident polarization is chosen as $\psi = 45°, \varphi = 0$. Inset is a schematic of the device. (e) The corresponding polarization angle of the transmitted wave. (f) Nonlinear circular dichroism of the metamaterial with right circularly polarized wave illumination.

the scattering force acting on the whole unit cell. Both 45° linear polarization and circular polarization can generate strong relative force [see Fig. 6.9 (b)], which can drive the meta-atoms towards opposite directions and transform the planar array into a stereoscopic chiral system, leading to giant optical chiral response. The effect of circular dichroism in transmittance becomes prominent when the relative displacement of neighboring beams $s = 40$nm [see Fig. 6.9 (c)].

To estimate the nonlinear response, we design the nano-beams to be 110 μm long and fixed at both ends, giving an effective spring constant $\kappa \approx 90$ pN/μm.

Note that there are other mechanical designs that can provide the same effective spring constant. We further assume that each nano-beam supports 40 meta-atoms on the central part [see inset of Fig. 6.9 (d)]. The relative displacement-dependent force calculated in the periodic structure is employed to calculate the stable state of the system under different input power levels. As shown in Fig. 6.9 (d), for a 45° linear polarized incident wave, the nano-beams can show a relative displacement of more than 50 nm with a pump power density of less than 10 $\mu W/\mu m^2$, which corresponds to a total power consumption of around 16 mW over a $40\mu m \times 40^{-}m$ area of metamaterial. The corresponding giant optomechanically induced chirality is shown in Fig. 6.9 (e); more than 70° of polarization rotation can be found at the frequency of 200.8 THz.

One important feature of our structure distinguished from previous studies is that we can control the handedness of the metamaterial directly using circularly polarized waves. For example, by pumping the metamaterial with a right circularly polarized wave, it becomes more transparent to right circular polarization and more opaque to the opposite handedness [see Fig. 6.9 (f)]. Note that in the linear regime the system is purely achiral. The current design provides a unique paradigm to achieve *pure nonlinear optical activity* with a controllable handedness in the optical frequency regime. In comparison to previous proposal [209], the nonlinear optical activity achieved here is based on the change of structural symmetry rather than resonance shifting; therefore the strength of nonlinear optical activity is symmetric for both handedness and it does not require any pre-introduced unbalancing (linear chirality).

6.2.3 Metasurface-Membrane Nano-fabrication

To fabricate the opto-mechanical metasurface, we performed a three-step electron beam lithography. We firstly deposit a layer of 100 nm thick amorphous silicon on 100 nm thick silicon nitride membrane (NORCADA). We process the deposition with an Oxford Instrument Plasma-enhanced chemical vapor deposition (PECVD) machine with 475 sccm Helium and 25 sccm Silane at 250 degree Celsius, 1500 mTorr chamber pressure, 15 W forward power. We then performed an electron-beam lithography (EBL) on a silicon-silicon nitride wafer (100 nm top silicon thickness, 100 nm silicon nitride thickness) using the negative-tone resist ma-N 2403. After cleaning the top silicon surface by oxygen plasma (2 min, 200 W) with barrel etcher, we first spin-coated HMDS (Hexamethyldisilazane) as an adhesion promoter (3000 rpm, 30 s), directly followed by spin-coating the electron-beam resist (3000 rpm, 30 s), resulting in a resist thickness of 300 nm. We performed both a pre-exposure bake (100 C, 1 min) and a post-exposure bake (90 C, 1 min) and after baking, we spin a layer of e-spacer for conductive surface. After electron-beam exposure (7.5 μm aperture, 30 kv electron gun voltage), development was performed by inserting the sample into ma-D 525 developer for 35 s, followed by rinsing it in de-ionized water for 2 minutes. The resulting resist pattern was then used as an etch mask for an inductively coupled plasma (ICP) etching process (15 mTorr chamber pressure, 15 W RF power, 400 W

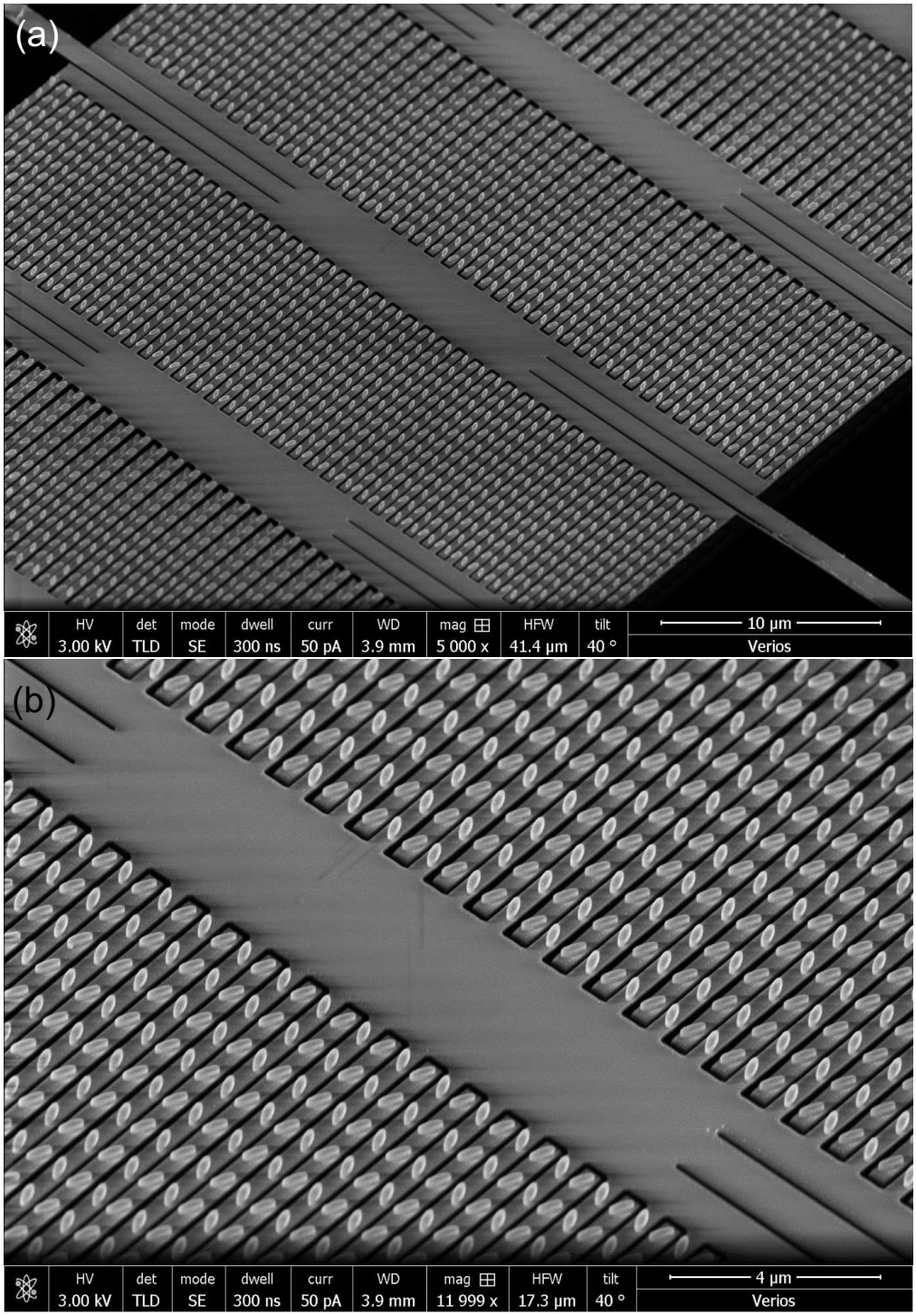

Figure 6.10: Scanning electron micrograph of the fabricated amorphous silicon elliptical pillar pairs metasurface on 100 nm thick silicon nitride nano-beams (a) whole view of the sample, and (b) magnified and oblique view of the same sample.

ICP power) using CHF_3 (50 sccm) and HF_6 (1.8 sccm) as etch gases. Remaining resist was removed by oxygen plasma. The second lithography we processed is for gold markers. We use PMMA 950 for the photoresist mask and perform EBL, following by applying electron-beam evaporator to deposit 30 nm gold film. After deposition, we use hot acetone for lifting-off the film to obtain gold markers. At the final EBL step, we use ZEP 520A as a positive-tone photoresist (4000 rpm, 2 min) and perform positioning lithography (7.5 μm aperture, 30 kv electron gun voltage), development was applied by using cold ZEP developer for 80 s, followed by rinsing it in isopropanol for 1 min. Finally, use the same recipe to etch silicon nitride membranes to achieve the nano-beams.

6.2.4 Conclusion and future work

We have proposed a novel paradigm to achieve full spatial control of metamaterials working at infrared and optical frequencies. We found that scattering forces may play a significant role in triggering the structural symmetry breaking. We have analytically and numerically investigated the force asymmetry in pairs and arrays based on non-parallel coupled dipoles, showing that this effect is quite general as long as the incident wave can simultaneously overlap with the two normal modes. The effect in an array becomes more significant due to the collective enhancement, which can be used to achieve achiral-chiral phase transition with controllable handedness. While the designs presented here are focused on the manipulation of structural symmetry and optical chirality, it can also be employed to achieve other types of spatial modulation. Due to the subwavelength nature of metamaterials, the proposed paradigm holds great potential to achieve dynamic spatial control of the near-field components of light.
In the future, we will measure the spectra of the fabricated devices. Secondly, we will apply nonlinear measurement for the optical forces, such as Fig.6.9(f). We can apply two different circular polarized light to excite the metasurfaces and observe the transmission. Furthermore, we could also measure the polarization state regarding to different incident powers.

∗This chapter's theory part is from Dr. Mingkai Liu, and the fabrication was performed by myself and Prof. Duk-Yong Choi.

Chapter 7

Conclusion and Outlook

7.1 Conclusion

In the 21st century, human beings are drastically developing their technologies and civilizations, spanning from the space exploration and colonization, to human bodies health and gene engineering; from brain study to artificial intelligence; from wearable devices to robots. The boom of those technologies are originated from the demand of human beings for biological advancement, and the tools that can help to realize our desires. Physics and engineering are always the pivotal fundamentals for those technologies. In order to benefit the development of those fields, *nano-optics* and *nano-photonics* are the ones which are crucial tools assisting the detection and diagnostics of substances and elements, such as biological molecules, drugs, and human bodies' health conditions (such as wearable devices for heartbeat rate, blood pressure, blood glucose level measurement and so on). Moreover, they can also help the advanced logical calculations and super fast information deliveries, such as quantum computing and optical communications. Based on this big picture, this thesis is focused on integrated nanoantennas in advanced optical communications fields and two-dimensional metasurfaces for quantum light manipulation, dynamic spatial controlling near-field light, bio-detections and compact optical devices.

Generally, in this thesis, we have designed, fabricated, and characterized the devices that we proposed. We normally design our devices with an FDTD software CST Microwave studio, such as calculating optical waveguides modes and dispersions; single nano-particle cross-sections, electric field, phase, scattering pattern; and metasurface transmission, reflection spectra, surface fields, phase. Then, we perform different fabrication techniques for different circumstances. Normally, we use electron-beam lithography (EBL) to generate a mask layer of photoresist for the nanostructures, and those masks can be utilized either for lifting-off or etching. For those metallic nanoantennas and alignment markers, we use lift-off techniques by immersing samples into hot acetone or photoresist remover, depending on what resist we use. On the other hand, for those dielectric materials such as silicon and silicon nitride, we perform inductive coupled plasma (ICP) to etch the materials. Multiple EBL processes should be performed for the multilayer-structure samples. For most metallic film deposition, we use an electron beam evaporator or thermal evaporator,

while, for the dielectric film deposition, we use sputter, plasma-enhanced chemical vapor deposition (PECVD) or atomic layer deposition (ALD) machines.

Chapter 2 - chapter 4 are focused on nanoantenna waveguide integration. While in chapter 5 and chapter 6, we aimed at the study of nanoantenna arrays–metasurfaces.

Specifically, Chapter 2 mainly talked about directional scattering with two dipoles interference model and how Fano resonance makes bidirectional scattering. We combined the above two concepts with Babinet's principle, and designed an innovative and compact single particle nanoantenna that can split different wavelengths of light into opposite directions which can be potentially used as a nanoscale wavelength demultiplexer.

Continuing Chapter 2's design and idea, in Chapter 3, we experimentally realized Fano nanoantenna and silicon waveguide integration. We fabricated a gold plasmonic Fano nanoantenna and a ring grating on the slab silicon waveguide. We measured the nanoantenna's directivities with 1550 nm and 1310 nm laser light via the ring grating and we achieved excellent results. Finally, we excited our nanoantennas by two different wavelength of laser light with different modulation frequencies and the coupling signals were captured by an InGaAs camera. In this way, we can measure how our nanoantennas can simultaneously demultiplex two different wavelengths of light and couple them into opposite directions of the waveguide.

Following the nanoscale wavelength-demultiplexer in chapter 3, in chapter 4, we proposed a nano polarization demultiplexer. Firstly, we discussed the design of polarization sensitive uni-directional waveguide coupler nanoantennas, and we combined two orthogonal polarizations sensitive nanoantennas together to realize an integrated polarization-sensitive mode-selective demultiplexer. We then fabricated low loss single-mode silicon rib waveguides and integrated plasmonic polarization sensitive nanoantennas on top of waveguides. We achieved high coupling front to back ratios measured with the help of plasmonic gratings at the each side of nanoantennas. We also characterized the response of the waveguide modes with respect to the incident light polarizations, and it indicates that the waveguides modes polarizations can be controlled by the polarizations of the incident light with our nanoantenna. Finally, we successfully presented low bit-error-rate penalty with a 10 GHz modulated 1550 nm light applied on our antenna-waveguide device. Therefore, this nano-scale polarization demultiplexer is ready for commercial telecommunication applications.

Chapter 5's goal is to provide a possibility for high efficient quantum or localized light manipulation. We presented the fabrication procedures for hybrid multilayer metasurfaces and experimentally characterized the sample with its transmission spectra for different polarizations responses. In addition, we also numerically analyzed the cross-sections, front to back ratio, and multipole expansion with a single pair of our hybrid elements. Our design can not only enhance the localized source

with a plasmonic feed element, but also efficiently and uni-directionally scatter light with a dielectric director element.

In chapter 6 we proposed an all dielectric metasurface made from arrays of tilted elliptical pillar pairs. This metasurface can provide a narrow, clean, well-pronounced resonance with high efficiency. Based on those characters, we applied this design into two different projects – bio-sensing and opto-mechanical applications. For bio-sensing metasurface application, we fabricated amorphous silicon nano pillar arrays on glass substrate, followed by the spectra measurement, which achieved high sensitivity and high figure of merit. We also performed the real-time microfluid bioassay measurement with protein (A/G) and antibody (IgG) for the single sensor detection and for the multiple sensors detections. Finally we achieved the multiple sensors detection's limit is below 5 ng/ml and for the single sensor detection, it is far below this limit. For opto-mechanics applications, we designed and fabricated the fish-bone structure metasurface. It consists of two layers of structures. The first layer is formed by 100 nm thick amorphous silicon elliptical nano-pillar arrays, and the second layer consisted of 100 nm thick silicon nitride nano-beams. Furthermore, we have analytically and numerically investigated the force asymmetry in pairs and arrays based on non-parallel coupled dipoles, showing that this effect is quite general as long as the incident wave can simultaneously overlap with the two normal modes. The effect in an array becomes more significant due to the collective enhancement, which can be used to achieve achiral-chiral phase transition with controllable handedness. While the designs presented here are focused on the manipulation of structural symmetry and optical chirality, it can also be employed to achieve other types of spatial modulation. Due to the subwavelength nature of metamaterials, the proposed paradigm holds great potential to achieve dynamic spatial control of the near-field components of light.

7.2 Outlook

In this thesis, we have talked about nanoantenna-optical waveguide integration for vertical light coupling, and this is mainly for multilayer vertically crossed waveguides information exchange (Fig. 1.1 (a),(f)). Since this work is very meaningful for optical information interconnectors, as well as highly compact multilayer optical transceivers, more works could be done related to the previous ones, such as two (multi-) layers of vertically crossed waveguides light transition via nanoantennas (Fig. 1.1 (f)). The nanoantennas at the intersections could also be used as wavelength demultiplexer and polarization demultiplexer.

Furthermore, after we have demonstrated the possibility of fabrication of hybrid nanoantennas or metasurfaces, we have opened some very promising research opportunities, which could be explored in the future. In the field of quantum optics, we can use the plasmonic antennas to enhance the quantum dot light emission and

to utilize the dielectric antennas to direct single photons to a desired direction for the further quantum information processing. Moreover, in biosensing applications, the plasmonic nanoantennas can enhance the fluorophore's photoluminescence, while the dielectric ones can guide the photoluminescence light into the right direction to achieve highly efficient detections.

In addition, all dielectric metasurfaces have a lot of potentials in various fields, due to their low loss, sharp resonances characteristics. The sensitivity of their narrow-band resonances to the changes of the external environment can be applied for gas, liquid and dust detection applications. Furthermore, the low loss metamaterials are very suitable as an alternative of traditional optical components, such as lenses and waveplates. Although there are some meta-lens works published to date [98], a multilayer, aberration corrected meta-lens can be the next big field. This is because of the huge current demand for highly compact and integrated optics, such as portable virtual/augmented/mixed reality devices, and wearable technology.

Appendix

A.1 Theoretical model of electromagnetic interaction

We employ a nearfield interaction model based on the free-space Green's function to quantitatively evaluate the electromagnetic response of coupled meta-atoms. As we have shown in our previous studies [200–202], meta-atoms can support a number of eigenmodes, and the mode profiles, i.e. the spatial distributions of current and charge are in general frequency dependent. However, such variations are very small around the eigen frequencies, particularly for meta-atoms made from good conductors. In this situation, the current $\mathbf{J}(\mathbf{r},\omega)$ and charge $\rho(\mathbf{r},\omega)$ density of a single meta-atom can be separated into spatial distribution and frequency-dependent mode amplitude, i.e. $\mathbf{J}(\mathbf{r},\omega) = -\mathrm{i}\omega Q(\omega)\mathbf{j}(\mathbf{r})$, $\rho(\mathbf{r},\omega) = Q(\omega)\mathrm{q}(\mathbf{r})$. $\mathrm{q}(\mathbf{r}) = -\nabla\cdot\mathbf{j}(\mathbf{r})$, where the mode profiles are approximated by the ones at the eigen frequencies, which can be found numerically [202]. For the lowest order eigenmode of a cut-wire meta-atom, it has a sinusoidal-like current distribution. The advantage of using this eigenmode approximation is that we can calculate the resonant behavior of complex coupled systems over a broadband of frequencies.

The coupled mode equations of the zig-zag dipole system can be written as

$$\mathrm{i}\omega\sum_{j=1}^{2}\sum_{n=1}^{N} Z_{(i,m),(j,n)}Q_{(j,n)} = \mathcal{E}_{(i,m)}. \tag{A.1}$$

Q is the frequency-dependent mode amplitude that describes the resonant behavior. Z is the effective impedance that describes the interaction, which can be defined from the normalized current and charge distribution $\mathbf{j}$ and q. The first subscript i denotes the two different orientations of meta-atoms, i.e. $\theta_{i=1} = -\theta_{i=2} = \theta$; the second subscript denotes the number of meta-atoms. $\mathcal{E}$ is the effective electromotive force imposed by the incident field

$$\mathcal{E} = \int \mathbf{j}\cdot\mathbf{E}^{\mathrm{i}}\mathrm{d}\mathbf{r}^3. \tag{A.2}$$

For plane wave excitation, $\mathcal{E} = \mathbf{l}\cdot\mathbf{E}^{\mathrm{i}}$, where $\mathbf{l} = \mathbf{p}/Q$ is the normalized electric dipole moment of a single meta-atom.

The effective impedance $Z = \mathrm{i}\omega L + 1/(\mathrm{i}\omega C)$ can be calculated directly from the

spatial distributions of current $\mathbf{j}(\mathbf{r})$ and charge $\mathrm{q}(\mathbf{r})$ of the eigenmode, where

$$L_{(i,m),(j,n)} = \iint \frac{\mathbf{j}[\mathbf{r}_{(i,m)}]\cdot\mathbf{j}[\mathbf{r}_{(j,n)}]}{4\pi c^2\varepsilon_0}\frac{e^{\mathrm{i}k_0|\mathbf{r}_{(i,m)}-\mathbf{r}_{(j,n)}|}}{|\mathbf{r}_{(i,m)}-\mathbf{r}_{(j,n)}|}\,\mathrm{d}^3\mathbf{r}_{(i,m)}\,\mathrm{d}^3\mathbf{r}_{(j,n)}, \tag{A.3}$$

$$\frac{1}{C_{(i,m),(j,n)}} = \iint \frac{\mathrm{q}[\mathbf{r}_{(i,m)}]\mathrm{q}[\mathbf{r}_{(j,n)}]}{4\pi\varepsilon_0}\frac{e^{\mathrm{i}k_0|\mathbf{r}_{(i,m)}-\mathbf{r}_{(j,n)}|}}{|\mathbf{r}_{(i,m)}-\mathbf{r}_{(j,n)}|}\,\mathrm{d}^3\mathbf{r}_{(i,m)}\,\mathrm{d}^3\mathbf{r}_{(j,n)}, \tag{A.4}$$

The coupled matrix can be diagonalized and rewritten in the basis of normal modes. This can be done by using a transformation matrix $\overleftrightarrow{T}$ composed of the eigen-basis of normal modes. For a simple two-resonator coupled system, it supports two normal modes: symmetric $\hat{\mathbf{e}}_\mathrm{S} = \frac{1}{\sqrt{2}}[1,1]$ and antisymmetric $\hat{\mathbf{e}}_\mathrm{A} = \frac{1}{\sqrt{2}}[1,-1]$. The coupled equations can be rewritten in a more instructive form based on the eigenbasis of normal modes:

$$\begin{bmatrix} Z_\mathrm{S} & 0 \\ 0 & Z_\mathrm{A} \end{bmatrix}\begin{bmatrix} Q_\mathrm{S} \\ Q_\mathrm{A} \end{bmatrix} = \begin{bmatrix} \mathcal{E}_\mathrm{S} \\ \mathcal{E}_\mathrm{A} \end{bmatrix}, \tag{A.5}$$

in which $Z_\mathrm{S} = Z_{ii} + Z_{ij}$, $Z_\mathrm{A} = Z_{ii} - Z_{ij}$ are the impedances of symmetric and antisymmetric modes, respectively; $Q_S = (Q_1 + Q_2)/\sqrt{2}$ and $Q_A = (Q_1 - Q_2)/\sqrt{2}$ are the corresponding mode amplitudes; $\mathcal{E}_S = (\mathcal{E}_1 + \mathcal{E}_2)/\sqrt{2}$ and $\mathcal{E}_A = (\mathcal{E}_1 - \mathcal{E}_2)/\sqrt{2}$ are the corresponding effective electromotive forces. They can be obtained via the following transformation:

$$\begin{bmatrix} Z_\mathrm{S} & 0 \\ 0 & Z_\mathrm{A} \end{bmatrix} = \overleftrightarrow{T}\begin{bmatrix} Z_{11} & Z_{12} \\ Z_{21} & Z_{22} \end{bmatrix}\overleftrightarrow{T}^{-1}, \tag{A.6}$$

$$\begin{bmatrix} Q_\mathrm{S} \\ Q_\mathrm{A} \end{bmatrix} = \overleftrightarrow{T}\begin{bmatrix} Q_1 \\ Q_2 \end{bmatrix}, \tag{A.7}$$

$$\begin{bmatrix} \mathcal{E}_\mathrm{S} \\ \mathcal{E}_\mathrm{A} \end{bmatrix} = \overleftrightarrow{T}\begin{bmatrix} \mathcal{E}_1 \\ \mathcal{E}_2 \end{bmatrix}, \tag{A.8}$$

where

$$\overleftrightarrow{T} = [\hat{\mathbf{e}}_\mathrm{S}, \hat{\mathbf{e}}_\mathrm{A}]^T = \frac{1}{\sqrt{2}}\begin{bmatrix} 1 & 1 \\ 1 & -1 \end{bmatrix} \tag{A.9}$$

is the transformation matrix.

For one-dimensional infinite array with periodicity A_x in the main text, the equation can be simplified using the Bloch boundary condition: $Q_{(i,n)} = Q_{(i,0)}e^{\mathrm{i}k_x nA_x} = Q_i e^{\mathrm{i}k_x nA_x}$. The simplified coupled equation can be written as

$$-\mathrm{i}\omega\left[Z_\mathrm{s}Q_i + Z_\mathrm{m}Q_{j\neq i}\right] = \mathcal{E}_i,\ (i,j=1,2) \tag{A.10}$$

where the self-impedance Z_s and the mutual impedance Z_m are re-defined as

$$Z_s = Z_{(i,0),(i,0)} + 2\sum_{n=1}^{\infty} Z_{(i,0),(i,n)} \cos(k_x n A_x), \tag{A.11}$$

$$Z_m = 2\sum_{n=0}^{\infty} Z_{(i,0),(j\neq i,n)} \cos[k_x (n+1/2) A_x]. \tag{A.12}$$

In the main text, for better readability, we use $Z_{i,i} = Z_s$ and $Z_{i,j} = Z_m$. Solving the coupled equations gives the mode amplitudes of the two meta-atoms within a unit cell, $Q_1 = \mathcal{E}_1 A - \mathcal{E}_2 B, Q_2 = \mathcal{E}_2 A - \mathcal{E}_1 B$, with $A = Z_s/(Z_s^2 - Z_m^2)$, $B = Z_m/(Z_s^2 - Z_m^2)$.

A.2 Calculation of Optical Forces

Once the mode amplitude Q of each meta-atom is found, we can calculate the time-averaged optical force directly from the current density $\mathbf{J}(\mathbf{r},\omega)$ and charge density $\rho(\mathbf{r},\omega)$:

$$\mathbf{F}^{\text{opt}}(\mathbf{r}) = \mathbf{F}^{\text{ext}}(\mathbf{r}) + \mathbf{F}^{\text{int}}(\mathbf{r}), \tag{A.13}$$

where $\mathbf{F}^{\text{ext}}$ is the external force due to the interaction of the meta-atom and the incident wave $(\mathbf{E}^{\text{i}}, \mathbf{B}^{\text{i}})$, and $\mathbf{F}^{\text{int}}$ is the internal force due to the interaction of meta-atoms via their scattered field $(\mathbf{E}^{\text{s}}, \mathbf{B}^{\text{s}})$.

For a plane wave interacting with a meta-atom dominated by electric dipole moment (such as a cut-wire),

$$\begin{aligned} \mathbf{F}^{\text{ext}}(\mathbf{r}) &= \frac{1}{2} Re\left[\rho^*(\mathbf{r})\mathbf{E}^{\text{i}}(\mathbf{r}) + \mathbf{J}^*(\mathbf{r}) \times \mathbf{B}^{\text{i}}(\mathbf{r})\right] \\ &\approx \frac{1}{2}\text{Re}\left[\nabla \mathbf{E}^{\text{i}}(\mathbf{r}) \cdot \mathbf{p}^*\right] \end{aligned} \tag{A.14}$$

and

$$\begin{aligned} \mathbf{F}^{\text{int}}(\mathbf{r}) &= \frac{1}{2} Re\Big[\rho^*(\mathbf{r})\mathbf{E}^{\text{s}}(\mathbf{r}) + \mathbf{J}^*(\mathbf{r}) \times \mathbf{B}^{\text{s}}(\mathbf{r})\Big] \\ &= \frac{1}{2} Re\left\{\rho^*(\mathbf{r})\left[-\nabla\phi(\mathbf{r}) - \frac{\partial}{\partial t}\mathbf{A}(\mathbf{r})\right] + \mathbf{J}^*(\mathbf{r}) \times \Big[\nabla \times \mathbf{A}(\mathbf{r})\Big]\right\} \end{aligned} \tag{A.15}$$

where the scalar potential $\phi(\mathbf{r})$ and vector potential $\mathbf{A}(\mathbf{r})$ at the field point $\mathbf{r}$ are determined by the current and charge at the source point $\mathbf{r}'$

$$\phi(\mathbf{r}) = \int_{V'} \frac{\rho(\mathbf{r}')e^{ik_0|\mathbf{r}-\mathbf{r}'|}}{4\pi\epsilon_0|\mathbf{r}-\mathbf{r}'|} \mathrm{d}^3\mathbf{r}', \tag{A.16}$$

$$\mathbf{A}(\mathbf{r}) = \int_{V'} \frac{\mathbf{J}(\mathbf{r}')e^{ik_0|\mathbf{r}-\mathbf{r}'|}}{4\pi c^2\epsilon_0|\mathbf{r}-\mathbf{r}'|} \mathrm{d}^3\mathbf{r}'. \tag{A.17}$$

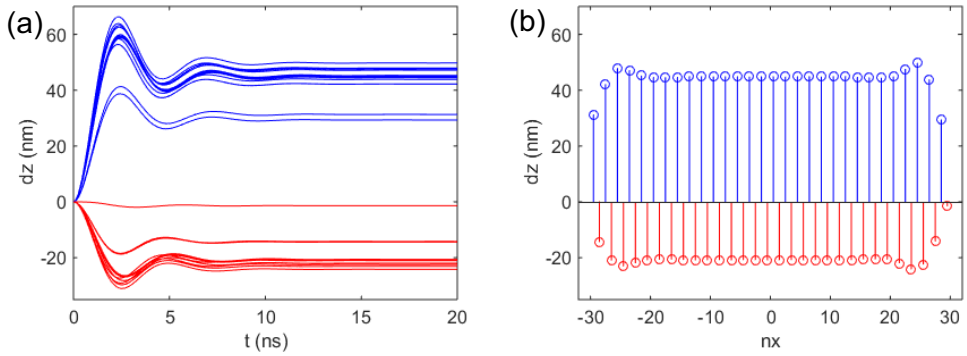

Figure A.1: (a) The dynamics and (b) the final stable state of a finite array of meta-atoms. The blue and red curves correspond to meta-atoms "1" and "2". The incident polarization is chosen as $\psi = 45^\circ$ and $\varphi = 0$ (45° linear polarization); orientation angle $\theta = 15^\circ$.

From Eqs. (A.15) to (A.17), we get the expression for the internal force in terms of the current and charge of interacting meta-atoms:

$$\begin{aligned}\mathbf{F}^{int} &= \frac{1}{2}Re\Bigg\{\int_V\int_{V'}\frac{e^{ik_0|\mathbf{r}-\mathbf{r}'|}}{4\pi\epsilon_0|\mathbf{r}-\mathbf{r}'|}\Bigg\{\left(\frac{1}{|\mathbf{r}-\mathbf{r}'|}-ik_0\right)\rho^*(\mathbf{r})\rho(\mathbf{r}')\mathbf{e_R}+\frac{i\omega}{c^2}\rho^*(\mathbf{r})\mathbf{J}(\mathbf{r}')\\ &\quad -\frac{1}{c^2}\left(\frac{1}{|\mathbf{r}-\mathbf{r}'|}-ik_0\right)\Big[\mathbf{e_R}\Big(\mathbf{J}^*(\mathbf{r})\cdot\mathbf{J}(\mathbf{r}')\Big)-\mathbf{J}(\mathbf{r}')\Big(\mathbf{e_R}\cdot\mathbf{J}^*(\mathbf{r})\Big)\Big]\Bigg\}d^3\mathbf{r}'d^3\mathbf{r}\Bigg\},\end{aligned} \tag{A.18}$$

where $\mathbf{e_R} = (\mathbf{r}-\mathbf{r}')/|\mathbf{r}-\mathbf{r}'|$. V and V' are the volume of interacting meta-atoms. The above method is quite general and can be applied to finite systems. In the design presented in the paper, the cut-wires are in the $x-y$ plane, and thus there is no z component of current, and the expression of $\mathbf{F}_z^{\text{opt}}$ can be simplified as

$$\begin{aligned}F_z^{\text{int}} &= \frac{1}{2}\text{Re}\left(\int_V\rho^*\mathbf{E}^{\text{s}}+\mathbf{J}^*\times\mathbf{B}^{\text{s}}d\mathbf{r}^3\right)\cdot\mathbf{z}\\ &= \frac{1}{2}\text{Re}\Bigg\{\int_V\int_{V'}\left(\frac{1}{|\mathbf{r}-\mathbf{r}'|}-ik\right)\frac{\exp(ik|\mathbf{r}-\mathbf{r}'|)}{4\pi\epsilon_0|\mathbf{r}-\mathbf{r}'|}\Big[\rho(\mathbf{r})\rho^*(\mathbf{r}')-\mathbf{J}(\mathbf{r})\cdot\mathbf{J}^*(\mathbf{r}')\Big]\mathbf{e_R}d\mathbf{r}'^3d\mathbf{r}^3\Bigg\}\cdot\mathbf{z},\end{aligned} \tag{A.19}$$

as indicated by the Equation 6.3 in the main text.

A.3 Nonlinear Dynamics

By introducing flexible mechanical feedback, the displacement of meta-atoms, denoted by the center of mass position $\mathbf{r}_{(i,m)}^{(c)}$ can be controlled. The nonlinear dynamics

and the stable state of the system can be found by solving the coupled equations

$$-\mathrm{i}\omega \sum_{j=1}^{2} \sum_{n=1}^{N} Z_{(i,m),(j,n)} Q_{(j,n)} = \mathcal{E}_{(i,m)}, \tag{A.20}$$

$$\mathcal{M}\ddot{\mathbf{r}}^{(\mathrm{c})}_{(i,m)} + \Gamma\dot{\mathbf{r}}^{(\mathrm{c})}_{(i,m)} = F^{\mathrm{opt}}[\mathbf{r}^{(\mathrm{c})}_{(i,m)}] + F^{\mathrm{mech}}[\mathbf{r}^{(\mathrm{c})}_{(i,m)}]. \tag{A.21}$$

Here $\mathcal{M}$ is the mass of the meta-atom, Γ is the mechanical damping due to the viscosity of the environment. Note that $Z_{(i,m),(j,n)}$, $\mathcal{E}_{(i,m)}$ and the response $Q_{(i,m)}$ are functions of $\mathbf{r}^{(\mathrm{c})}_{(i,m)}$. As an example, Figure A.1 shows the dynamics and final stable state of a finite array of meta-atoms, the same as the one studied in Figure 3 of the main text. The mass of the meta-atom is estimated as $5.4\times10^{-14}\mu$g based on the geometry of a silicon meta-atom proposed in Figure. 6.9 of the main text. The damping is chosen such that the mechanical oscillation is highly damped.

∗The Appendix is from Dr. Mingkai Liu.

References

1. A. V. Krishnamoorthy and D. A. Miller, "Scaling optoelectronic-vlsi circuits into the 21st century: a technology roadmap," *IEEE Journal of Selected Topics in Quantum Electronics*, vol. 2, no. 1, pp. 55–76, 1996. (cited on page 1)

2. D. A. Miller, "Optical interconnects to silicon," *IEEE Journal of Selected Topics in Quantum Electronics*, vol. 6, no. 6, pp. 1312–1317, 2000. (cited on page 1)

3. S. Assefa, S. Shank, W. Green, M. Khater, E. Kiewra, C. Reinholm, S. Kamlapurkar, A. Rylyakov, C. Schow, F. Horst, *et al.*, "A 90 nm cmos integrated nano-photonics technology for 25 gbps wdm optical communications applications," in *IEEE International Electron Devices Meeting (IEDM)*, vol. 33, pp. 8–33, 2012. (cited on page 2)

4. B. Shen, P. Wang, R. Polson, and R. Menon, "An integrated-nanophotonics polarization beamsplitter with 2.4$\times$ 2.4 μm2 footprint," *Nature Photonics*, vol. 9, no. 6, pp. 378–382, 2015. (cited on pages 2 and 3)

5. A. Y. Piggott, J. Lu, K. G. Lagoudakis, J. Petykiewicz, T. M. Babinec, and J. Vučković, "Inverse design and demonstration of a compact and broadband on-chip wavelength demultiplexer," *Nature Photonics*, vol. 9, no. 6, pp. 374–377, 2015. (cited on pages 2 and 3)

6. R. Guo, M. Decker, F. Setzpfandt, I. Staude, D. N. Neshev, and Y. S. Kivshar, "Plasmonic fano nanoantennas for on-chip separation of wavelength-encoded optical signals," *Nano letters*, vol. 15, no. 5, pp. 3324–3328, 2015. (cited on pages 2, 48, and 66)

7. M. Agio and A. Alù, *Optical antennas*. Cambridge University Press, 2013. (cited on page 3)

8. T. Taminiau, F. Stefani, F. Segerink, and N. Van Hulst, "Optical antennas direct single-molecule emission," *Nature Photonics*, vol. 2, no. 4, pp. 234–237, 2008. (cited on pages 5 and 6)

9. W. Zhou, M. Dridi, J. Y. Suh, C. H. Kim, D. T. Co, M. R. Wasielewski, G. C. Schatz, T. W. Odom, *et al.*, "Lasing action in strongly coupled plasmonic nanocavity arrays," *Nature nanotechnology*, vol. 8, no. 7, pp. 506–511, 2013. (cited on pages 5 and 6)

10. L. Tang, S. E. Kocabas, S. Latif, A. K. Okyay, D.-S. Ly-Gagnon, K. C. Saraswat, and D. A. Miller, "Nanometre-scale germanium photodetector enhanced by a

near-infrared dipole antenna," *Nature Photonics*, vol. 2, no. 4, pp. 226–229, 2008. (cited on pages 5 and 6)

11. A. G. Curto, G. Volpe, T. H. Taminiau, M. P. Kreuzer, R. Quidant, and N. F. van Hulst, "Unidirectional emission of a quantum dot coupled to a nanoantenna," *Science*, vol. 329, no. 5994, pp. 930–933, 2010. (cited on pages 5, 6, 25, and 65)

12. Y. De Wilde, F. Formanek, R. Carminati, B. Gralak, P.-A. Lemoine, K. Joulain, J.-P. Mulet, Y. Chen, and J.-J. Greffet, "Thermal radiation scanning tunnelling microscopy," *Nature*, vol. 444, no. 7120, pp. 740–743, 2006. (cited on pages 5 and 6)

13. N. Liu, M. L. Tang, M. Hentschel, H. Giessen, and A. P. Alivisatos, "Nanoantenna-enhanced gas sensing in a single tailored nanofocus," *Nature materials*, vol. 10, no. 8, pp. 631–636, 2011. (cited on pages 5 and 6)

14. M. W. Knight, H. Sobhani, P. Nordlander, and N. J. Halas, "Photodetection with active optical antennas," *Science*, vol. 332, no. 6030, pp. 702–704, 2011. (cited on pages 5, 6, 35, and 48)

15. J. C. Maxwell, "A dynamical theory of the electromagnetic field," *Philosophical transactions of the Royal Society of London*, vol. 155, pp. 459–512, 1865. (cited on page 4)

16. J. C. Maxwell, "A treatise on electricity and magnetism," 1873. (cited on page 4)

17. C. A. Balanis, *Antenna theory: analysis and design*. John Wiley & Sons, 2016. (cited on pages 6, 10, 28, and 29)

18. L. Novotny, "From near-field optics to optical antennas," *Phys. Today*, vol. 64, no. 7, pp. 47–52, 2011. (cited on page 6)

19. L. Novotny, "The history of near-field optics," (cited on page 6)

20. P. Bharadwaj, B. Deutsch, and L. Novotny, "Optical antennas," *Advances in Optics and Photonics*, vol. 1, no. 3, pp. 438–483, 2009. (cited on page 6)

21. P. Verma, T. Ichimura, T.-a. Yano, Y. Saito, and S. Kawata, "Nano-imaging through tip-enhanced raman spectroscopy: Stepping beyond the classical limits," *Laser & Photonics Reviews*, vol. 4, no. 4, pp. 548–561, 2010. (cited on page 6)

22. A. Ono, J.-i. Kato, and S. Kawata, "Subwavelength optical imaging through a metallic nanorod array," *Physical review letters*, vol. 95, no. 26, p. 267407, 2005. (cited on page 6)

23. S. Kawata, A. Ono, and P. Verma, "Subwavelength colour imaging with a metallic nanolens," *Nature Photonics*, vol. 2, no. 7, pp. 438–442, 2008. (cited on page 6)

24. R. F. Oulton, V. J. Sorger, T. Zentgraf, R.-M. Ma, C. Gladden, L. Dai, G. Bartal, and X. Zhang, "Plasmon lasers at deep subwavelength scale," *Nature*, vol. 461, no. 7264, pp. 629–632, 2009. (cited on page 6)

25. H. Aouani, S. Itzhakov, D. Gachet, E. Devaux, T. W. Ebbesen, H. Rigneault, D. Oron, and J. Wenger, "Colloidal quantum dots as probes of excitation field enhancement in photonic antennas," *ACS nano*, vol. 4, no. 8, pp. 4571–4578, 2010. (cited on page 6)

26. M. Ren, M. Chen, W. Wu, L. Zhang, J. Liu, B. Pi, X. Zhang, Q. Li, S. Fan, and J. Xu, "Linearly polarized light emission from quantum dots with plasmonic nanoantenna arrays," *Nano letters*, vol. 15, no. 5, pp. 2951–2957, 2015. (cited on page 6)

27. J. Lin, J. B. Mueller, Q. Wang, G. Yuan, N. Antoniou, X.-C. Yuan, and F. Capasso, "Polarization-controlled tunable directional coupling of surface plasmon polaritons," *Science*, vol. 340, no. 6130, pp. 331–334, 2013. (cited on pages 6, 25, 27, and 35)

28. J. S. White, G. Veronis, Z. Yu, E. S. Barnard, A. Chandran, S. Fan, and M. L. Brongersma, "Extraordinary optical absorption through subwavelength slits," *Optics letters*, vol. 34, no. 5, pp. 686–688, 2009. (cited on page 6)

29. L. Cao, J. S. White, J.-S. Park, J. A. Schuller, B. M. Clemens, and M. L. Brongersma, "Engineering light absorption in semiconductor nanowire devices," *Nature materials*, vol. 8, no. 8, pp. 643–647, 2009. (cited on page 6)

30. L. Cao, P. Fan, A. P. Vasudev, J. S. White, Z. Yu, W. Cai, J. A. Schuller, S. Fan, and M. L. Brongersma, "Semiconductor nanowire optical antenna solar absorbers," *Nano letters*, vol. 10, no. 2, pp. 439–445, 2010. (cited on page 6)

31. A. B. Evlyukhin, S. I. Bozhevolnyi, A. Pors, M. G. Nielsen, I. P. Radko, M. Willatzen, and O. Albrektsen, "Detuned electrical dipoles for plasmonic sensing," *Nano letters*, vol. 10, no. 11, pp. 4571–4577, 2010. (cited on page 6)

32. A. E. Cetin, D. Etezadi, B. C. Galarreta, M. P. Busson, Y. Eksioglu, and H. Altug, "Plasmonic nanohole arrays on a robust hybrid substrate for highly sensitive label-free biosensing," *Acs Photonics*, vol. 2, no. 8, pp. 1167–1174, 2015. (cited on pages 6 and 75)

33. H. A. Atwater and A. Polman, "Plasmonics for improved photovoltaic devices," *Nature materials*, vol. 9, no. 3, pp. 205–213, 2010. (cited on page 6)

34. L. Cao, J.-S. Park, P. Fan, B. Clemens, and M. L. Brongersma, "Resonant germanium nanoantenna photodetectors," *Nano letters*, vol. 10, no. 4, pp. 1229–1233, 2010. (cited on page 6)

35. J. A. Schuller, E. S. Barnard, W. Cai, Y. C. Jun, J. S. White, and M. L. Brongersma, "Plasmonics for extreme light concentration and manipulation," *Nature materials*, vol. 9, no. 3, pp. 193–204, 2010. (cited on pages 6 and 35)

36. L. Novotny and N. Van Hulst, "Antennas for light," *Nature photonics*, vol. 5, no. 2, pp. 83–90, 2011. (cited on pages 6 and 36)

37. V. Giannini, A. I. Fernández-Domínguez, S. C. Heck, and S. A. Maier, "Plasmonic nanoantennas: fundamentals and their use in controlling the radiative properties of nanoemitters," *Chemical reviews*, vol. 111, no. 6, pp. 3888–3912, 2011. (cited on page 6)

38. P. Biagioni, J.-S. Huang, and B. Hecht, "Nanoantennas for visible and infrared radiation," *Reports on Progress in Physics*, vol. 75, no. 2, p. 024402, 2012. (cited on pages 6 and 65)

39. M. Decker, I. Staude, I. I. Shishkin, K. B. Samusev, P. Parkinson, V. K. Sreenivasan, A. Minovich, A. E. Miroshnichenko, A. Zvyagin, C. Jagadish, *et al.*, "Dual-channel spontaneous emission of quantum dots in magnetic metamaterials," *Nature communications*, vol. 4, 2013. (cited on pages 6, 19, and 66)

40. A. Artar, A. A. Yanik, and H. Altug, "Directional double fano resonances in plasmonic hetero-oligomers," *Nano letters*, vol. 11, no. 9, pp. 3694–3700, 2011. (cited on pages 6, 27, and 36)

41. I. S. Maksymov, I. Staude, A. E. Miroshnichenko, and Y. S. Kivshar, "Optical yagi-uda nanoantennas," *Nanophotonics*, vol. 1, no. 1, pp. 65–81, 2012. (cited on page 6)

42. S. A. Lavasani and T. Pakizeh, "Color-switched directional ultracompact optical nanoantennas," *JOSA B*, vol. 29, no. 6, pp. 1361–1366, 2012. (cited on pages 6, 27, and 36)

43. M. V. Rybin, P. V. Kapitanova, D. S. Filonov, A. P. Slobozhanyuk, P. A. Belov, Y. S. Kivshar, and M. F. Limonov, "Fano resonances in antennas: General control over radiation patterns," *Physical Review B*, vol. 88, no. 20, p. 205106, 2013. (cited on pages 6, 27, and 36)

44. Z. Xi, Y. Lu, W. Yu, P. Yao, P. Wang, and H. Ming, "Tailoring the directivity of both excitation and emission of dipole simultaneously with two-colored plasmonic antenna," *Optics express*, vol. 21, no. 24, pp. 29365–29373, 2013. (cited on page 6)

45. I. M. Hancu, A. G. Curto, M. Castro-Lopez, M. Kuttge, and N. F. van Hulst, "Multipolar interference for directed light emission," *Nano letters*, vol. 14, no. 1, pp. 166–171, 2013. (cited on pages 6, 65, and 71)

46. J. S. Liu, R. A. Pala, F. Afshinmanesh, W. Cai, and M. L. Brongersma, "A submicron plasmonic dichroic splitter," *Nature communications*, vol. 2, p. 525, 2011. (cited on pages 6, 25, 27, and 35)

47. Y. Liu, S. Palomba, Y. Park, T. Zentgraf, X. Yin, and X. Zhang, "Compact magnetic antennas for directional excitation of surface plasmons," *Nano letters*, vol. 12, no. 9, pp. 4853–4858, 2012. (cited on pages 6, 25, 27, and 35)

48. F. Bernal Arango, A. Kwadrin, and A. F. Koenderink, "Plasmonic antennas hybridized with dielectric waveguides," *ACS nano*, vol. 6, no. 11, pp. 10156–10167, 2012. (cited on pages 6, 25, and 48)

49. T. Sidiropoulos, S. Maier, and R. Oulton, "Efficient low dispersion compact plasmonic-photonic coupler," *Optics express*, vol. 20, no. 11, pp. 12359–12365, 2012. (cited on pages 6 and 25)

50. J. Zuloaga and P. Nordlander, "On the energy shift between near-field and far-field peak intensities in localized plasmon systems," *Nano letters*, vol. 11, no. 3, pp. 1280–1283, 2011. (cited on page 8)

51. M. A. Kats, N. Yu, P. Genevet, Z. Gaburro, and F. Capasso, "Effect of radiation damping on the spectral response of plasmonic components," *Optics express*, vol. 19, no. 22, pp. 21748–21753, 2011. (cited on page 8)

52. C. F. Bohren and D. R. Huffman, *Absorption and scattering of light by small particles*. John Wiley & Sons, 2008. (cited on page 9)

53. H. G. Booker *et al.*, "Slot aerials and their relation to complementary wire aerials (babinet's principle)," *J. IEE*, vol. 93, no. pt III, pp. 620–626, 1946. (cited on page 10)

54. J. D. Jackson, *Classical electrodynamics*. Wiley, 1999. (cited on page 10)

55. V. Asadchy, I. Faniayeu, Y. Ra'di, S. Khakhomov, I. Semchenko, and S. Tretyakov, "Broadband reflectionless metasheets: frequency-selective transmission and perfect absorption," *Physical Review X*, vol. 5, no. 3, p. 031005, 2015. (cited on page 11)

56. Y. Ra'di, C. Simovski, and S. Tretyakov, "Thin perfect absorbers for electromagnetic waves: theory, design, and realizations," *Physical Review Applied*, vol. 3, no. 3, p. 037001, 2015. (cited on page 11)

57. T. Niemi, A. O. Karilainen, and S. A. Tretyakov, "Synthesis of polarization transformers," *IEEE Transactions on Antennas and Propagation*, vol. 61, no. 6, pp. 3102–3111, 2013. (cited on pages 11 and 13)

58. S. Tretyakov, *Analytical modeling in applied electromagnetics*. Artech House, 2003. (cited on pages 11 and 13)

59. V. V. Yatsenko, S. I. Maslovski, S. A. Tretyakov, S. L. Prosvirnin, and S. Zouhdi, "Plane-wave reflection from double arrays of small magnetoelectric scatterers," *IEEE Transactions on Antennas and Propagation*, vol. 51, no. 1, pp. 2–11, 2003. (cited on page 13)

60. S. A. Maier, *Plasmonics: fundamentals and applications*. Springer Science & Business Media, 2007. (cited on page 16)

61. W. Cai and V. M. Shalaev, *Optical metamaterials*, vol. 10. Springer, 2010. (cited on pages 17, 18, and 83)

62. J. Pendry, "Introduction," *Optics Express*, vol. 11, no. 7, pp. 639–639, 2003. (cited on page 17)

63. G. Thompson, "Unusual waveguide characteristics associated with the apparent negative permeability obtainable in ferrites," 1955. (cited on page 17)

64. U. Leonhardt, "Optical metamaterials: Invisibility cup," *Nature photonics*, vol. 1, no. 4, pp. 207–208, 2007. (cited on pages 17 and 18)

65. D. Barber and I. Freestone, "An investigation of the origin of the colour of the lycurgus cup by analytical transmission electron microscopy," *Archaeometry*, vol. 32, no. 1, pp. 33–45, 1990. (cited on pages 17 and 18)

66. V. G. Veselago, "The electrodynamics of substances with simultaneously negative values of ϵ and μ," *Soviet physics uspekhi*, vol. 10, no. 4, p. 509, 1968. (cited on pages 17 and 18)

67. J. B. Pendry, A. J. Holden, D. Robbins, and W. Stewart, "Magnetism from conductors and enhanced nonlinear phenomena," *IEEE transactions on microwave theory and techniques*, vol. 47, no. 11, pp. 2075–2084, 1999. (cited on pages 17 and 18)

68. D. R. Smith, W. J. Padilla, D. Vier, S. C. Nemat-Nasser, and S. Schultz, "Composite medium with simultaneously negative permeability and permittivity," *Physical review letters*, vol. 84, no. 18, p. 4184, 2000. (cited on pages 17 and 18)

69. J. B. Pendry, "Negative refraction makes a perfect lens," *Physical review letters*, vol. 85, no. 18, p. 3966, 2000. (cited on pages 17 and 18)

70. N. Fang, H. Lee, C. Sun, and X. Zhang, "Sub–diffraction-limited optical imaging with a silver superlens," *Science*, vol. 308, no. 5721, pp. 534–537, 2005. (cited on pages 17, 18, and 19)

71. F. E. Wagner, S. Haslbeck, L. Stievano, S. Calogero, Q. Pankhurst, and K.-P. Martinek, "Before striking gold in gold-ruby glass," *Nature*, vol. 407, no. 6805, pp. 691–692, 2000. (cited on page 17)

72. J. Pendry, A. Holden, W. Stewart, and I. Youngs, "Extremely low frequency plasmons in metallic mesostructures," *Physical review letters*, vol. 76, no. 25, p. 4773, 1996. (cited on page 17)

73. V. M. Shalaev, W. Cai, U. K. Chettiar, H.-K. Yuan, A. K. Sarychev, V. P. Drachev, and A. V. Kildishev, "Negative index of refraction in optical metamaterials," *Optics letters*, vol. 30, no. 24, pp. 3356–3358, 2005. (cited on pages 17 and 19)

74. S. Zhang, W. Fan, N. Panoiu, K. Malloy, R. Osgood, and S. Brueck, "Experimental demonstration of near-infrared negative-index metamaterials," *Physical review letters*, vol. 95, no. 13, p. 137404, 2005. (cited on page 17)

75. G. Dolling, C. Enkrich, M. Wegener, C. M. Soukoulis, and S. Linden, "Low-loss negative-index metamaterial at telecommunication wavelengths," *Optics letters*, vol. 31, no. 12, pp. 1800–1802, 2006. (cited on page 17)

76. G. Dolling, M. Wegener, C. M. Soukoulis, and S. Linden, "Negative-index metamaterial at 780 nm wavelength," *Optics letters*, vol. 32, no. 1, pp. 53–55, 2007. (cited on page 17)

77. S. Xiao, U. K. Chettiar, A. V. Kildishev, V. P. Drachev, and V. M. Shalaev, "Yellow-light negative-index metamaterials," *Optics letters*, vol. 34, no. 22, pp. 3478–3480, 2009. (cited on page 17)

78. U. K. Chettiar, A. V. Kildishev, H.-K. Yuan, W. Cai, S. Xiao, V. P. Drachev, and V. M. Shalaev, "Dual-band negative index metamaterial: double negative at 813 nm and single negative at 772 nm," *Optics Letters*, vol. 32, no. 12, pp. 1671–1673, 2007. (cited on page 19)

79. S. P. Burgos, R. de Waele, A. Polman, and H. A. Atwater, "A single-layer wide-angle negative-index metamaterial at visible frequencies," *Nature Materials*, vol. 9, no. 5, pp. 407–412, 2010. (cited on page 19)

80. S. Linden, C. Enkrich, M. Wegener, J. Zhou, T. Koschny, and C. M. Soukoulis, "Magnetic response of metamaterials at 100 terahertz," *Science*, vol. 306, no. 5700, pp. 1351–1353, 2004. (cited on page 19)

81. S. Zhang, W. Fan, B. Minhas, A. Frauenglass, K. Malloy, and S. Brueck, "Mid-infrared resonant magnetic nanostructures exhibiting a negative permeability," *Physical review letters*, vol. 94, no. 3, p. 037402, 2005. (cited on page 19)

82. W. Cai, U. K. Chettiar, H.-K. Yuan, V. C. de Silva, A. V. Kildishev, V. P. Drachev, and V. M. Shalaev, "Metamagnetics with rainbow colors," *Optics Express*, vol. 15, no. 6, pp. 3333–3341, 2007. (cited on page 19)

83. E. Plum, V. Fedotov, A. Schwanecke, N. Zheludev, and Y. Chen, "Giant optical gyrotropy due to electromagnetic coupling," *Applied Physics Letters*, vol. 90, no. 22, p. 223113, 2007. (cited on page 19)

84. M. Decker, M. Klein, M. Wegener, and S. Linden, "Circular dichroism of planar chiral magnetic metamaterials," *Optics letters*, vol. 32, no. 7, pp. 856–858, 2007. (cited on page 19)

85. E. Plum, V. Fedotov, and N. Zheludev, "Optical activity in extrinsically chiral metamaterial," *Applied Physics Letters*, vol. 93, no. 19, p. 191911, 2008. (cited on page 19)

86. E. Plum, V. Fedotov, and N. Zheludev, "Extrinsic electromagnetic chirality in metamaterials," *Journal of Optics A: Pure and Applied Optics*, vol. 11, no. 7, p. 074009, 2009. (cited on page 19)

87. V. Fedotov, P. Mladyonov, S. Prosvirnin, A. Rogacheva, Y. Chen, and N. Zheludev, "Asymmetric propagation of electromagnetic waves through a planar chiral structure," *Physical review letters*, vol. 97, no. 16, p. 167401, 2006. (cited on page 19)

88. M. W. Klein, C. Enkrich, M. Wegener, and S. Linden, "Second-harmonic generation from magnetic metamaterials," *Science*, vol. 313, no. 5786, pp. 502–504, 2006. (cited on page 19)

89. A. Popov and V. M. Shalaev, "Negative-index metamaterials: second-harmonic generation, manley–rowe relations and parametric amplification," *Applied Physics B*, vol. 84, no. 1-2, pp. 131–137, 2006. (cited on page 19)

90. I. V. Shadrivov, A. B. Kozyrev, D. W. van der Weide, and Y. S. Kivshar, "Tunable transmission and harmonic generation in nonlinear metamaterials," *Applied Physics Letters*, vol. 93, no. 16, p. 161903, 2008. (cited on page 19)

91. K. O'Brien, H. Suchowski, J. Rho, A. Salandrino, B. Kante, X. Yin, and X. Zhang, "Predicting nonlinear properties of metamaterials from the linear response," *Nature materials*, vol. 14, no. 4, pp. 379–383, 2015. (cited on page 19)

92. W. Cai, D. A. Genov, and V. M. Shalaev, "Superlens based on metal-dielectric composites," *Physical review B*, vol. 72, no. 19, p. 193101, 2005. (cited on page 19)

93. Z. Jacob, L. V. Alekseyev, and E. Narimanov, "Optical hyperlens: far-field imaging beyond the diffraction limit," *Optics express*, vol. 14, no. 18, pp. 8247–8256, 2006. (cited on page 19)

94. T. Taubner, D. Korobkin, Y. Urzhumov, G. Shvets, and R. Hillenbrand, "Near-field microscopy through a sic superlens," *Science*, vol. 313, no. 5793, pp. 1595–1595, 2006. (cited on page 19)

95. Z. Liu, H. Lee, Y. Xiong, C. Sun, and X. Zhang, "Far-field optical hyperlens magnifying sub-diffraction-limited objects," *science*, vol. 315, no. 5819, pp. 1686–1686, 2007. (cited on page 19)

96. Z. Liu, S. Durant, H. Lee, Y. Pikus, N. Fang, Y. Xiong, C. Sun, and X. Zhang, "Far-field optical superlens," *Nano Letters*, vol. 7, no. 2, pp. 403–408, 2007. (cited on page 19)

97. I. I. Smolyaninov, Y.-J. Hung, and C. C. Davis, "Magnifying superlens in the visible frequency range," *Science*, vol. 315, no. 5819, pp. 1699–1701, 2007. (cited on page 19)

98. M. Khorasaninejad, W. T. Chen, R. C. Devlin, J. Oh, A. Y. Zhu, and F. Capasso, "Metalenses at visible wavelengths: Diffraction-limited focusing and subwavelength resolution imaging," *Science*, vol. 352, no. 6290, pp. 1190–1194, 2016. (cited on pages 19, 20, and 102)

99. J. B. Pendry, D. Schurig, and D. R. Smith, "Controlling electromagnetic fields," *science*, vol. 312, no. 5781, pp. 1780–1782, 2006. (cited on pages 19 and 83)

100. D. Schurig, J. Mock, B. Justice, S. A. Cummer, J. B. Pendry, A. Starr, and D. Smith, "Metamaterial electromagnetic cloak at microwave frequencies," *Science*, vol. 314, no. 5801, pp. 977–980, 2006. (cited on page 19)

101. W. Cai, U. K. Chettiar, A. V. Kildishev, and V. M. Shalaev, "Optical cloaking with metamaterials," *Nature photonics*, vol. 1, no. 4, pp. 224–227, 2007. (cited on page 19)

102. J. Valentine, J. Li, T. Zentgraf, G. Bartal, and X. Zhang, "An optical cloak made of dielectrics," *Nature materials*, vol. 8, no. 7, pp. 568–571, 2009. (cited on page 19)

103. T. Ergin, N. Stenger, P. Brenner, J. B. Pendry, and M. Wegener, "Three-dimensional invisibility cloak at optical wavelengths," *Science*, vol. 328, no. 5976, pp. 337–339, 2010. (cited on page 19)

104. N. Yu, P. Genevet, M. A. Kats, F. Aieta, J.-P. Tetienne, F. Capasso, and Z. Gaburro, "Light propagation with phase discontinuities: generalized laws of reflection and refraction," *science*, vol. 334, no. 6054, pp. 333–337, 2011. (cited on pages 19 and 20)

105. N. Yu, F. Aieta, P. Genevet, M. A. Kats, Z. Gaburro, and F. Capasso, "A broadband, background-free quarter-wave plate based on plasmonic metasurfaces," *Nano letters*, vol. 12, no. 12, pp. 6328–6333, 2012. (cited on pages 19 and 20)

106. S. Sun, Q. He, S. Xiao, Q. Xu, X. Li, and L. Zhou, "Gradient-index meta-surfaces as a bridge linking propagating waves and surface waves," *Nature materials*, vol. 11, no. 5, pp. 426–431, 2012. (cited on pages 19 and 20)

107. B. Walther, C. Helgert, C. Rockstuhl, F. Setzpfandt, F. Eilenberger, E.-B. Kley, F. Lederer, A. Tünnermann, and T. Pertsch, "Spatial and spectral light shaping with metamaterials," *Advanced Materials*, vol. 24, no. 47, pp. 6300–6304, 2012. (cited on pages 19 and 20)

108. L. Huang, X. Chen, H. Mühlenbernd, G. Li, B. Bai, Q. Tan, G. Jin, T. Zentgraf, and S. Zhang, "Dispersionless phase discontinuities for controlling light propagation," *Nano letters*, vol. 12, no. 11, pp. 5750–5755, 2012. (cited on pages 19 and 20)

109. X. Yin, Z. Ye, J. Rho, Y. Wang, and X. Zhang, "Photonic spin hall effect at metasurfaces," *Science*, vol. 339, no. 6126, pp. 1405–1407, 2013. (cited on pages 19 and 20)

110. H. Hua, "Sunglass-like displays become a reality with freeform optical technology," *SPIE Newsroom*, 2012. (cited on page 20)

111. C. M. Soukoulis and M. Wegener, "Past achievements and future challenges in the development of three-dimensional photonic metamaterials," *Nature Photonics*, vol. 5, no. 9, pp. 523–530, 2011. (cited on page 19)

112. A. V. Kildishev, A. Boltasseva, and V. M. Shalaev, "Planar photonics with metasurfaces," *Science*, vol. 339, no. 6125, p. 1232009, 2013. (cited on page 19)

113. N. Yu and F. Capasso, "Flat optics with designer metasurfaces," *Nature materials*, vol. 13, no. 2, pp. 139–150, 2014. (cited on pages 19 and 83)

114. http://www.gadgethelpline.com/smart-contact-lenses-whos-got-their-eyes-on-the-prize/
https://www3.oculus.com/en-us/rift/
https://hypebeast.com/2016/4/sony-patents-smart-contact-lens camera (cited on page 19)

115. K. Tanaka, E. Plum, J. Ou, T. Uchino, and N. Zheludev, "Multifold enhancement of quantum dot luminescence in plasmonic metamaterials," *Physical review letters*, vol. 105, no. 22, p. 227403, 2010. (cited on pages 19 and 21)

116. S. Najmaei, A. Mlayah, A. Arbouet, C. Girard, J. Léotin, and J. Lou, "Plasmonic pumping of excitonic photoluminescence in hybrid mos_2–au nanostructures," *ACS nano*, vol. 8, no. 12, pp. 12682–12689, 2014. (cited on pages 21 and 22)

117. K. V. Sreekanth, Y. Alapan, M. ElKabbash, E. Ilker, M. Hinczewski, U. A. Gurkan, A. De Luca, and G. Strangi, "Extreme sensitivity biosensing platform based on hyperbolic metamaterials," *Nature materials*, 2016. (cited on pages 21 and 22)

118. J. Zhang, K. F. MacDonald, and N. I. Zheludev, "Nonlinear dielectric optomechanical metamaterials," *Light: Science & Applications*, vol. 2, no. 8, p. e96, 2013. (cited on pages 21, 22, and 84)

119. K. E. Chong, I. Staude, A. James, J. Dominguez, S. Liu, S. Campione, G. S. Subramania, T. S. Luk, M. Decker, D. N. Neshev, *et al.*, "Polarization-independent silicon metadevices for efficient optical wavefront control," *Nano letters*, vol. 15, no. 8, pp. 5369–5374, 2015. (cited on pages 21, 22, and 48)

120. K. E. Chong, L. Wang, I. Staude, A. R. James, J. Dominguez, S. Liu, G. S. Subramania, M. Decker, D. N. Neshev, I. Brener, *et al.*, "Efficient polarization-insensitive complex wavefront control using huygens' metasurfaces based on dielectric resonant meta-atoms," *ACS Photonics*, vol. 3, no. 4, pp. 514–519, 2016. (cited on pages 21, 22, and 48)

121. D. Dregely, R. Taubert, J. Dorfmüller, R. Vogelgesang, K. Kern, and H. Giessen, "3d optical yagi-uda nanoantenna array," *Nature communications*, vol. 2, p. 267, 2011. (cited on pages 25 and 36)

122. W. Zhu, D. Wang, and K. B. Crozier, "Direct observation of beamed raman scattering," *Nano letters*, vol. 12, no. 12, pp. 6235–6243, 2012. (cited on page 25)

123. W. Liu, A. E. Miroshnichenko, D. N. Neshev, and Y. S. Kivshar, "Broadband unidirectional scattering by magneto-electric core–shell nanoparticles," *ACS nano*, vol. 6, no. 6, pp. 5489–5497, 2012. (cited on pages 25 and 36)

124. D. Vercruysse, Y. Sonnefraud, N. Verellen, F. B. Fuchs, G. Di Martino, L. Lagae, V. V. Moshchalkov, S. A. Maier, and P. Van Dorpe, "Unidirectional side scattering of light by a single-element nanoantenna," *Nano letters*, vol. 13, no. 8, pp. 3843–3849, 2013. (cited on pages 25 and 36)

125. I. Staude, I. S. Maksymov, M. Decker, A. E. Miroshnichenko, D. N. Neshev, C. Jagadish, and Y. S. Kivshar, "Broadband scattering by tapered nanoantennas," *physica status solidi (RRL)-Rapid Research Letters*, vol. 6, no. 12, pp. 466–468, 2012. (cited on pages 25 and 36)

126. B. Luk'yanchuk, N. I. Zheludev, S. A. Maier, N. J. Halas, P. Nordlander, H. Giessen, and C. T. Chong, "The fano resonance in plasmonic nanostructures and metamaterials," *Nature materials*, vol. 9, no. 9, pp. 707–715, 2010. (cited on pages 26 and 36)

127. A. E. Miroshnichenko, S. Flach, and Y. S. Kivshar, "Fano resonances in nanoscale structures," *Reviews of Modern Physics*, vol. 82, no. 3, p. 2257, 2010. (cited on page 26)

128. U. Fano, "Effects of configuration interaction on intensities and phase shifts," *Physical Review*, vol. 124, no. 6, p. 1866, 1961. (cited on page 26)

129. T. Shegai, S. Chen, V. D. Miljković, G. Zengin, P. Johansson, and M. Käll, "A bimetallic nanoantenna for directional colour routing," *Nature communications*, vol. 2, p. 481, 2011. (cited on page 27)

130. N. Feth, S. Linden, M. Klein, M. Decker, F. Niesler, Y. Zeng, W. Hoyer, J. Liu, S. Koch, J. Moloney, *et al.*, "Second-harmonic generation from complementary split-ring resonators," *Optics letters*, vol. 33, no. 17, pp. 1975–1977, 2008. (cited on page 29)

131. D. K. Gramotnev and S. I. Bozhevolnyi, "Plasmonics beyond the diffraction limit," *Nature photonics*, vol. 4, no. 2, pp. 83–91, 2010. (cited on pages 35 and 48)

132. R. Zia, J. A. Schuller, A. Chandran, and M. L. Brongersma, "Plasmonics: the next chip-scale technology," *Materials today*, vol. 9, no. 7, pp. 20–27, 2006. (cited on pages 35 and 48)

133. G. Konstantatos and E. H. Sargent, "Nanostructured materials for photon detection," *Nature nanotechnology*, vol. 5, no. 6, pp. 391–400, 2010. (cited on pages 35 and 48)

134. I. Goykhman, B. Desiatov, J. Khurgin, J. Shappir, and U. Levy, "Locally oxidized silicon surface-plasmon schottky detector for telecom regime," *Nano letters*, vol. 11, no. 6, pp. 2219–2224, 2011. (cited on pages 35 and 48)

135. A. Sobhani, M. W. Knight, Y. Wang, B. Zheng, N. S. King, L. V. Brown, Z. Fang, P. Nordlander, and N. J. Halas, "Narrowband photodetection in the near-infrared with a plasmon-induced hot electron device," *Nature communications*, vol. 4, p. 1643, 2013. (cited on pages 35 and 48)

136. H. Chalabi, D. Schoen, and M. L. Brongersma, "Hot-electron photodetection with a plasmonic nanostripe antenna," *Nano letters*, vol. 14, no. 3, pp. 1374–1380, 2014. (cited on pages 35 and 48)

137. W. Cai, J. S. White, and M. L. Brongersma, "Compact, high-speed and power-efficient electrooptic plasmonic modulators," *Nano letters*, vol. 9, no. 12, pp. 4403–4411, 2009. (cited on pages 35 and 48)

138. A. Melikyan, L. Alloatti, A. Muslija, D. Hillerkuss, P. Schindler, J. Li, R. Palmer, D. Korn, S. Muehlbrandt, D. Van Thourhout, *et al.*, "High-speed plasmonic phase modulators," *Nature Photonics*, vol. 8, no. 3, pp. 229–233, 2014. (cited on pages 35 and 48)

139. S. I. Bozhevolnyi, V. S. Volkov, E. Devaux, J.-Y. Laluet, and T. W. Ebbesen, "Channel plasmon subwavelength waveguide components including interferometers and ring resonators," *Nature*, vol. 440, no. 7083, pp. 508–511, 2006. (cited on page 35)

140. F. López-Tejeira, S. G. Rodrigo, L. Martín-Moreno, F. J. García-Vidal, E. Devaux, T. W. Ebbesen, J. R. Krenn, I. Radko, S. I. Bozhevolnyi, M. U. González, *et al.*, "Efficient unidirectional nanoslit couplers for surface plasmons," *Nature Physics*, vol. 3, no. 5, pp. 324–328, 2007. (cited on page 35)

141. A. Baron, E. Devaux, J.-C. Rodier, J.-P. Hugonin, E. Rousseau, C. Genet, T. W. Ebbesen, and P. Lalanne, "Compact antenna for efficient and unidirectional launching and decoupling of surface plasmons," *Nano letters*, vol. 11, no. 10, pp. 4207–4212, 2011. (cited on page 35)

142. F. J. Rodríguez-Fortuño, G. Marino, P. Ginzburg, D. O'Connor, A. Martínez, G. A. Wurtz, and A. V. Zayats, "Near-field interference for the unidirectional excitation of electromagnetic guided modes," *Science*, vol. 340, no. 6130, pp. 328–330, 2013. (cited on pages 35 and 48)

143. J. Petersen, J. Volz, and A. Rauschenbeutel, "Chiral nanophotonic waveguide interface based on spin-orbit interaction of light," *Science*, vol. 346, no. 6205, pp. 67–71, 2014. (cited on pages 35 and 48)

144. T. P. Sidiropoulos, M. P. Nielsen, T. R. Roschuk, A. V. Zayats, S. A. Maier, and R. F. Oulton, "Compact optical antenna coupler for silicon photonics characterized by third-harmonic generation," *ACS Photonics*, vol. 1, no. 10, pp. 912–916, 2014. (cited on pages 35 and 48)

145. A. Y. Piggott, J. Lu, T. M. Babinec, K. G. Lagoudakis, J. Petykiewicz, and J. Vučković, "Inverse design and implementation of a wavelength demultiplexing grating coupler," *Scientific reports*, vol. 4, 2014. (cited on page 35)

146. R. Guo, M. Decker, I. Staude, D. N. Neshev, and Y. S. Kivshar, "Bidirectional waveguide coupling with plasmonic fano nanoantennas," *Applied Physics Letters*, vol. 105, no. 5, p. 053114, 2014. (cited on pages 36, 48, 52, and 66)

147. A. I. Kuznetsov, A. E. Miroshnichenko, Y. H. Fu, J. Zhang, and B. Luk'Yanchuk, "Magnetic light," *arXiv preprint arXiv:1205.1610*, 2012. (cited on page 47)

148. I. Staude, A. E. Miroshnichenko, M. Decker, N. T. Fofang, S. Liu, E. Gonzales, J. Dominguez, T. S. Luk, D. N. Neshev, I. Brener, *et al.*, "Tailoring directional scattering through magnetic and electric resonances in subwavelength silicon nanodisks," *ACS nano*, vol. 7, no. 9, pp. 7824–7832, 2013. (cited on pages 47, 66, and 69)

149. M. Decker, I. Staude, M. Falkner, J. Dominguez, D. N. Neshev, I. Brener, T. Pertsch, and Y. S. Kivshar, "High-efficiency dielectric huygens' surfaces," *Advanced Optical Materials*, vol. 3, no. 6, pp. 813–820, 2015. (cited on pages 48, 66, 69, and 72)

150. M. I. Shalaev, J. Sun, A. Tsukernik, A. Pandey, K. Nikolskiy, and N. M. Litchinitser, "High-efficiency all-dielectric metasurfaces for ultracompact beam manipulation in transmission mode," *Nano letters*, vol. 15, no. 9, pp. 6261–6266, 2015. (cited on page 48)

151. P. Berini and I. De Leon, "Surface plasmon-polariton amplifiers and lasers," *Nature Photonics*, vol. 6, no. 1, pp. 16–24, 2012. (cited on page 48)

152. I. P. Kaminow and T. Li, "Optical fiber telecommunications iv-a, volume a: Components," 2002. (cited on page 54)

153. S. Kharitonov, R. Kiselev, A. Kumar, I. F. de Jáuregui Ruiz, X. Shi, K. Leósson, T. Pertsch, S. Nolte, S. Bozhevolnyi, and A. Chipouline, "Data transmission in long-range dielectric-loaded surface plasmon polariton waveguides," *Optics express*, vol. 22, no. 22, pp. 26742–26751, 2014. (cited on pages 55, 58, 61, and 63)

154. D. Marcuse, "Derivation of analytical expressions for the bit-error probability in lightwave systems with optical amplifiers," *Journal of Lightwave Technology*, vol. 8, no. 12, pp. 1816–1823, 1990. (cited on page 58)

155. J. Wang, D. Bonneau, M. Villa, J. W. Silverstone, R. Santagati, S. Miki, T. Yamashita, M. Fujiwara, M. Sasaki, H. Terai, *et al.*, "Chip-to-chip quantum photonic interconnect by path-polarization interconversion," *Optica*, vol. 3, no. 4, pp. 407–413, 2016. (cited on page 62)

156. S. S. Kruk, M. Decker, I. Staude, S. Schlecht, M. Greppmair, D. N. Neshev, and Y. S. Kivshar, "Spin-polarized photon emission by resonant multipolar nanoantennas," *ACS Photonics*, vol. 1, no. 11, pp. 1218–1223, 2014. (cited on pages 65 and 66)

157. T. H. Taminiau, F. D. Stefani, and N. F. van Hulst, "Enhanced directional excitation and emission of single emitters by a nano-optical yagi-uda antenna," *Optics express*, vol. 16, no. 14, pp. 10858–10866, 2008. (cited on page 66)

158. A. E. Krasnok, A. E. Miroshnichenko, P. A. Belov, and Y. S. Kivshar, "All-dielectric optical nanoantennas," *Optics Express*, vol. 20, no. 18, pp. 20599–20604, 2012. (cited on page 66)

159. S. Person, M. Jain, Z. Lapin, J. J. Saenz, G. Wicks, and L. Novotny, "Demonstration of zero optical backscattering from single nanoparticles," *Nano letters*, vol. 13, no. 4, pp. 1806–1809, 2013. (cited on page 66)

160. A. E. Krasnok, C. R. Simovski, P. A. Belov, and Y. S. Kivshar, "Superdirective dielectric nanoantennas," *Nanoscale*, vol. 6, no. 13, pp. 7354–7361, 2014. (cited on page 66)

161. A. Devilez, B. Stout, and N. Bonod, "Compact metallo-dielectric optical antenna for ultra directional and enhanced radiative emission," *ACS nano*, vol. 4, no. 6, pp. 3390–3396, 2010. (cited on page 66)

162. B. Rolly, B. Stout, and N. Bonod, "Boosting the directivity of optical antennas with magnetic and electric dipolar resonant particles," *Optics express*, vol. 20, no. 18, pp. 20376–20386, 2012. (cited on page 66)

163. X. Zeng, W. Yu, P. Yao, Z. Xi, Y. Lu, and P. Wang, "Metallo-dielectric hybrid antenna for high purcell factor and radiation efficiency," *Optics express*, vol. 22, no. 12, pp. 14517–14523, 2014. (cited on page 66)

164. E. Rusak, I. Staude, M. Decker, J. Sautter, A. E. Miroshnichenko, D. A. Powell, D. N. Neshev, and Y. S. Kivshar, "Hybrid nanoantennas for directional emission enhancement," *Applied Physics Letters*, vol. 105, no. 22, p. 221109, 2014. (cited on page 66)

165. S. Shopova, R. Rajmangal, S. Holler, and S. Arnold, "Plasmonic enhancement of a whispering-gallery-mode biosensor for single nanoparticle detection," *Applied Physics Letters*, vol. 98, no. 24, p. 243104, 2011. (cited on page 66)

166. R. Noskov, A. Krasnok, and Y. S. Kivshar, "Nonlinear metal–dielectric nanoantennas for light switching and routing," *New Journal of Physics*, vol. 14, no. 9, p. 093005, 2012. (cited on page 66)

167. T. G. Habteyes, I. Staude, K. E. Chong, J. Dominguez, M. Decker, A. Miroshnichenko, Y. Kivshar, and I. Brener, "Near-field mapping of optical modes on all-dielectric silicon nanodisks," *ACS Photonics*, vol. 1, no. 9, pp. 794–798, 2014. (cited on page 67)

168. P. B. Johnson and R.-W. Christy, "Optical constants of the noble metals," *Physical review B*, vol. 6, no. 12, p. 4370, 1972. (cited on page 69)

169. S. Mühlig, C. Menzel, C. Rockstuhl, and F. Lederer, "Multipole analysis of meta-atoms," *Metamaterials*, vol. 5, no. 2, pp. 64–73, 2011. (cited on page 70)

170. R. Alaee, R. Filter, D. Lehr, F. Lederer, and C. Rockstuhl, "A generalized kerker condition for highly directive nanoantennas," *Optics letters*, vol. 40, no. 11, pp. 2645–2648, 2015. (cited on page 72)

171. Z. Yu and S. Fan, "Extraordinarily high spectral sensitivity in refractive index sensors using multiple optical modes," *Optics express*, vol. 19, no. 11, pp. 10029–10040, 2011. (cited on page 76)

172. N. Engheta and R. W. Ziolkowski, *Metamaterials: physics and engineering explorations*. John Wiley & Sons, 2006. (cited on page 83)

173. H. Chen, C. Chan, and P. Sheng, "Transformation optics and metamaterials," *Nature materials*, vol. 9, no. 5, pp. 387–396, 2010. (cited on page 83)

174. A. Poddubny, I. Iorsh, P. Belov, and Y. Kivshar, "Hyperbolic metamaterials," *Nature Photonics*, vol. 7, no. 12, pp. 948–957, 2013. (cited on page 83)

175. J. Pendry, "A chiral route to negative refraction," *Science*, vol. 306, no. 5700, pp. 1353–1355, 2004. (cited on page 83)

176. S. Tretyakov, A. Sihvola, and L. Jylhä, "Backward-wave regime and negative refraction in chiral composites," *Photonics and Nanostructures-Fundamentals and Applications*, vol. 3, no. 2, pp. 107–115, 2005. (cited on page 83)

177. S. Zhang, Y.-S. Park, J. Li, X. Lu, W. Zhang, and X. Zhang, "Negative refractive index in chiral metamaterials," *Physical review letters*, vol. 102, no. 2, p. 023901, 2009. (cited on page 83)

178. J. K. Gansel, M. Thiel, M. S. Rill, M. Decker, K. Bade, V. Saile, G. von Freymann, S. Linden, and M. Wegener, "Gold helix photonic metamaterial as broadband circular polarizer," *Science*, vol. 325, no. 5947, pp. 1513–1515, 2009. (cited on page 83)

179. V. K. Valev, J. J. Baumberg, C. Sibilia, and T. Verbiest, "Chirality and chiroptical effects in plasmonic nanostructures: fundamentals, recent progress, and outlook," *Advanced Materials*, vol. 25, no. 18, pp. 2517–2534, 2013. (cited on page 83)

180. E. Plum, X.-X. Liu, V. Fedotov, Y. Chen, D. Tsai, and N. Zheludev, "Metamaterials: optical activity without chirality," *Physical review letters*, vol. 102, no. 11, p. 113902, 2009. (cited on page 83)

181. S. V. Zhukovsky, A. V. Novitsky, and V. M. Galynsky, "Elliptical dichroism: operating principle of planar chiral metamaterials," *Optics letters*, vol. 34, no. 13, pp. 1988–1990, 2009. (cited on page 83)

182. E. Plum, V. Fedotov, and N. Zheludev, "Asymmetric transmission: a generic property of two-dimensional periodic patterns," *J. Opt.*, vol. 13, no. 2, p. 024006, 2011. (cited on page 83)

183. A. D. Boardman, V. V. Grimalsky, Y. S. Kivshar, S. V. Koshevaya, M. Lapine, N. M. Litchinitser, V. N. Malnev, M. Noginov, Y. G. Rapoport, and V. M. Shalaev, "Active and tunable metamaterials," *Laser & Photonics Reviews*, vol. 5, no. 2, pp. 287–307, 2011. (cited on page 83)

184. N. I. Zheludev and Y. S. Kivshar, "From metamaterials to metadevices," *Nature materials*, vol. 11, no. 11, pp. 917–924, 2012. (cited on page 83)

185. M. Lapine, I. V. Shadrivov, and Y. S. Kivshar, "Colloquium: nonlinear metamaterials," *Reviews of Modern Physics*, vol. 86, no. 3, p. 1093, 2014. (cited on page 83)

186. I. V. Shadrivov, M. Lapine, Y. S. Kivshar, *et al.*, *Nonlinear, tunable and active metamaterials*. Springer, 2015. (cited on page 83)

187. S. Zhang, J. Zhou, Y.-S. Park, J. Rho, R. Singh, S. Nam, A. K. Azad, H.-T. Chen, X. Yin, A. J. Taylor, *et al.*, "Photoinduced handedness switching in terahertz chiral metamolecules," *Nature communications*, vol. 3, p. 942, 2012. (cited on page 83)

188. J. Zhou, D. R. Chowdhury, R. Zhao, A. K. Azad, H.-T. Chen, C. M. Soukoulis, A. J. Taylor, and J. F. O'Hara, "Terahertz chiral metamaterials with giant and

dynamically tunable optical activity," *Physical Review B*, vol. 86, no. 3, p. 035448, 2012. (cited on page 83)

189. M. Lapine, I. V. Shadrivov, D. A. Powell, and Y. S. Kivshar, "Magnetoelastic metamaterials," *Nature materials*, vol. 11, no. 1, pp. 30–33, 2012. (cited on pages 84 and 91)

190. M. Liu, Y. Sun, D. A. Powell, I. V. Shadrivov, M. Lapine, R. C. McPhedran, and Y. S. Kivshar, "Nonlinear response via intrinsic rotation in metamaterials," *Physical Review B*, vol. 87, no. 23, p. 235126, 2013. (cited on pages 84 and 91)

191. A. P. Slobozhanyuk, M. Lapine, D. A. Powell, I. V. Shadrivov, Y. S. Kivshar, R. C. McPhedran, and P. A. Belov, "Flexible helices for nonlinear metamaterials," *Advanced Materials*, vol. 25, no. 25, pp. 3409–3412, 2013. (cited on page 84)

192. M. Liu, D. Powell, I. Shadrivov, M. Lapine, and Y. S. Kivshar, "Self-oscillations in nonlinear torsional metamaterials," *New Journal of Physics*, vol. 15, no. 7, p. 073036, 2013. (cited on pages 84 and 91)

193. M. Liu, D. A. Powell, I. V. Shadrivov, M. Lapine, and Y. S. Kivshar, "Spontaneous chiral symmetry breaking in metamaterials," *Nature communications*, vol. 5, 2014. (cited on pages 84, 91, and 93)

194. T. J. Kippenberg and K. J. Vahala, "Cavity opto-mechanics," *Optics Express*, vol. 15, no. 25, pp. 17172–17205, 2007. (cited on page 84)

195. T. J. Kippenberg and K. J. Vahala, "Cavity optomechanics: back-action at the mesoscale," *science*, vol. 321, no. 5893, pp. 1172–1176, 2008. (cited on page 84)

196. M. Aspelmeyer, T. J. Kippenberg, and F. Marquardt, "Cavity optomechanics," *Reviews of Modern Physics*, vol. 86, no. 4, p. 1391, 2014. (cited on page 84)

197. Y. Sun, T. P. White, and A. A. Sukhorukov, "Slow-light enhanced optical forces between longitudinally shifted photonic-crystal nanowire waveguides," *Optics letters*, vol. 37, no. 5, pp. 785–787, 2012. (cited on page 84)

198. S. Albaladejo, M. I. Marqués, M. Laroche, and J. J. Sáenz, "Scattering forces from the curl of the spin angular momentum of a light field," *Physical review letters*, vol. 102, no. 11, p. 113602, 2009. (cited on page 86)

199. D. A. Powell, M. Lapine, M. V. Gorkunov, I. V. Shadrivov, and Y. S. Kivshar, "Metamaterial tuning by manipulation of near-field interaction," *Physical Review B*, vol. 82, no. 15, p. 155128, 2010. (cited on page 86)

200. D. A. Powell, K. Hannam, I. V. Shadrivov, and Y. S. Kivshar, "Near-field interaction of twisted split-ring resonators," *Physical Review B*, vol. 83, no. 23, p. 235420, 2011. (cited on pages 86 and 103)

201. M. Liu, D. A. Powell, I. V. Shadrivov, and Y. S. Kivshar, "Optical activity and coupling in twisted dimer meta-atoms," *Applied Physics Letters*, vol. 100, no. 11, p. 111114, 2012. (cited on pages 86 and 103)

202. D. A. Powell, "Resonant dynamics of arbitrarily shaped meta-atoms," *Physical Review B*, vol. 90, no. 7, p. 075108, 2014. (cited on pages 86 and 103)

203. H. Liu, J. Ng, S. Wang, Z. Lin, Z. Hang, C. Chan, and S. Zhu, "Strong light-induced negative optical pressure arising from kinetic energy of conduction electrons in plasmon-type cavities," *Physical review letters*, vol. 106, no. 8, p. 087401, 2011. (cited on page 89)

204. J. Chen, J. Ng, Z. Lin, and C. Chan, "Optical pulling force," *Nature photonics*, vol. 5, no. 9, pp. 531–534, 2011. (cited on page 89)

205. A. Dogariu, S. Sukhov, and J. Sáenz, "Optically induced'negative forces'," *Nature Photonics*, vol. 7, no. 1, pp. 24–27, 2013. (cited on page 89)

206. J.-Y. Ou, E. Plum, L. Jiang, and N. I. Zheludev, "Reconfigurable photonic metamaterials," *Nano letters*, vol. 11, no. 5, pp. 2142–2144, 2011. (cited on page 93)

207. J.-Y. Ou, E. Plum, J. Zhang, and N. I. Zheludev, "An electromechanically reconfigurable plasmonic metamaterial operating in the near-infrared," *Nature nanotechnology*, vol. 8, no. 4, pp. 252–255, 2013. (cited on page 93)

208. J. Valente, J.-Y. Ou, E. Plum, I. J. Youngs, and N. I. Zheludev, "A magneto-electro-optical effect in a plasmonic nanowire material," *Nature communications*, vol. 6, 2015. (cited on page 93)

209. I. V. Shadrivov, "Pure nonlinear optical activity in metamaterials," *Applied Physics Letters*, vol. 101, no. 4, p. 041911, 2012. (cited on page 95)